Structural Dynamics of Tensegrity Prisms and Masts Under Changing Cable Tension

by

Michelle R. Alber

(Under the Direction of R. Benjamin Davis)

Abstract

Tensegrity masts are a network of compressive and tensile elements, composed of multiple interconnected tensegrity units. Unlike other structures, tensegrities are not limited by fixed structural properties. The ability to vary cable tension in a tensegrity enables modification of the structural dynamic properties. This work studies how the natural frequencies of a tensegrity mast change with changing cable tension. A three-stage tensegrity mast is modeled and tested. The first several natural frequencies of the structure are tracked across a range of configurations. The results show the effect of tensioning different sets of cables on the natural frequencies of the mast. Applications for a tensegrity-based structure with tunable natural frequencies are discussed.

Index words: Tensegrity Prism, Tensegrity Mast, Form-Finding, Structural Dynamics, Modal Testing, Tensegrity Construction, Natural Frequency

Structural Dynamics of Tensegrity Prisms and Masts Under Changing Cable Tension

by

Michelle R. Alber

B.S., Georgia College & State University, 2014

A Dissertation Submitted to the Graduate Faculty
of The University of Georgia in Partial Fulfillment
of the
Requirements for the Degree

Masters of Science

Athens, Georgia

2017

©2017

Michelle R. Alber

All Rights Reserved

Structural Dynamics of Tensegrity Prisms and Masts Under Changing Cable Tension

by

Michelle R. Alber

Approved:

Major Professor: R. Benjamin Davis

Committee: Donald Leo
Eric Freeman

Electronic Version Approved:

Suzanne Barbour
Dean of the Graduate School
The University of Georgia
August 2017

Structural Dynamics of Tensegrity Prisms and Masts Under Changing Cable Tension

Michelle R. Alber

July 24, 2017

Acknowledgements

I would like to thank the UGA College of Engineering for this incredible experience. A special thank you goes to Clodagh Miller for encouraging me to pursue UGA for graduate school and coaching me through the admissions process.

I am thankful for the NASA Aeronautics Fellowship for funding my Master's degree and for providing financial support for my project. I also appreciate the mentorship of Vytas SunSpiral and the opportunity to collaborate at the NASA Ames Research Center.

I would like to thank my colleagues and peers for supporting me, especially those who have been a part of the Dynamic Devices & Solutions Lab. Thank you to Haning Xiu and Stephen Higgins for assisting me with my research and selflessly spending long hours to help me. Haning helped greatly with the mathematical modeling, while Stephen contributed to a good portion of the test article design.

Thank you, Dean Leo and Dr. Freeman, for serving on my committee and for all of your help and patience.

My deepest appreciation goes to my fabulous mentor, Dr. Davis. Thank you for providing me this opportunity and for your endless encouragement, support, and guidance. Without your continuous mentorship and direction, I would not be where I am today. Words cannot explain my level of gratitude.

This was truly a wonderful and enlightening experience that I will always treasure and I will miss you all dearly.

Contents

List of Figures

List of Tables

Nomenclature

The nomenclature follows the following scheme: All variables will be in italics. All operator names are capitalized. All vectors are column vectors. All matrices will be denoted by a bold capital letter $\mathbf{E}$, all vectors with a bold lowercase letter $\mathbf{v}$. The k^{th} column vector of a matrix $\mathbf{E}$ is denoted by the subscript proceeding the lowercase bold letter $\mathbf{e}_k$. The entries in a vector will be in italics v_k with a subscript number describing the k^{th} entry location.

Roman symbols

$\mathbf{a}$ Cross-sectional area vector, $\in \mathbb{R}^b$

$\mathbf{A}$	Equilibrium matrix, $\in \mathbb{R}^{3n \times b}$
b	Number of members
$\mathbf{C}$	Connectivity matrix, $\in \mathbb{R}^{b \times n}$
d	Member diameter
d	Number of dimensions
$\mathbf{D}$	Force density matrix, $\in \mathbb{R}^{b \times b}$
e	Young's modulus
$\mathbf{e}$	Member Young's modulus vector, $\in \mathbb{R}^{b}$
$\mathbf{f}$	Nodal external force vector, $\in \mathbb{R}^{n}$
$\mathbf{F}_{\mathrm{e}}$	Matrix of nodal external force vectors, $\in \mathbb{R}^{3 \times n}$
$\mathbf{F}_{\mathrm{m}}$	Matrix of member force vectors, $\in \mathbb{R}^{3 \times b}$
$\mathbf{F}_{\mathrm{n}}$	Matrix of resultant nodal force vectors, $\in \mathbb{R}^{3 \times b}$
$\mathbf{I}_{(k \times k)}$	Identity matrix, $\in \mathbb{R}^{k \times k}$
$\mathbf{J}$	Jacobian matrix, $\in \mathbb{R}^{3n \times 3n}$
$\mathbf{K}_{\mathrm{E}}$	Linear elastic stiffness matrix, $\in \mathbb{R}^{3n \times 3n}$
$\mathbf{K}_{\mathrm{G}}$	Geometric stiffness matrix, $\in \mathbb{R}^{3n \times 3n}$
$\mathbf{K}_{\mathrm{n}}$	Secant stiffness matrix, $\in \mathbb{R}^{3n \times 3n}$
$\mathbf{K}_{\mathrm{T}}$	Tangent stiffness matrix, $\in \mathbb{R}^{3n \times 3n}$
ℓ	Member length
$\boldsymbol{\ell}$	Member length vector, $\in \mathbb{R}^{b}$
$\boldsymbol{\ell}_0$	Unstressed member length vector, $\in \mathbb{R}^{b}$
m	Mass of member
m	Number of internal mechanisms
$\mathbf{M}$	Lumped nodal mass matrix, $\in \mathbb{R}^{3n \times 3n}$
n	Number of nodes
$\mathbf{n}$	Displacement vector, $\in \mathbb{R}^{3n}$
N	Dimension of null space

r	Number of rigid body modes
s	Number of self-stress states
t	Total number of iterations
$\mathbf{t}$	Member internal force vector, $\in \mathbb{R}^b$
tol	Tolerance value
$\mathbf{q}$	Force density vector, $\in \mathbb{R}^b$
$\mathbf{u}$	Left singular vector of $\mathbf{A}$, $\in \mathbb{R}^n$
$\mathbf{U}$	Left singular vector matrix of $\mathbf{A}$, $\in \mathbb{R}^{n \times n}$
$\mathbf{W}$	Right singular vector of $\mathbf{A}$, $\in \mathbb{R}^b$
$\mathbf{W}$	Right singular vector matrix of $\mathbf{A}$, $\in \mathbb{R}^{b \times b}$
$\mathbf{[x\ y\ z]}$	Nodal coordinate matrix, $\in \mathbb{R}^{n \times 3}$
$\mathbf{0}$	Vector of all zeros
$\mathbf{1}$	Vector of all ones

Greek symbols

γ	Index value
$\boldsymbol{\kappa}$	Member stiffness vector, $\in \mathbb{R}^b$
λ	Eigenvalue of $\mathbf{D}$
ω	Eigenvalue of $\mathbf{K}_\mathrm{n}$
$\mathbf{\Omega}$	Diagonal matrix of $\mathbf{K}_\mathrm{n}$'s eigenvalues, $\in \mathbb{R}^{3n \times 3n}$
$\boldsymbol{\phi}$	Eigenvector of $\mathbf{D}$, $\in \mathbb{R}^b$
$\mathbf{\Phi}$	Eigenvector matrix of $\mathbf{D}$, $\in \mathbb{R}^{b \times b}$
$\boldsymbol{\psi}$	Eigenvector of $\mathbf{K}_\mathrm{n}$, $\in \mathbb{R}^{3n}$
$\mathbf{\Psi}$	Eigenvector matrix of $\mathbf{K}_\mathrm{n}$, $\in \mathbb{R}^{3n \times 3n}$
μ	Singular value of $\mathbf{A}$
$\mathbf{\Sigma}$	Matrix of projected length vectors, $\in \mathbb{R}^{b \times 3}$

Superscripts

0	Value at 0^{th} iteration
i	Value at i^{th} iteration
t	Target value

Subscripts

0	Initial value
m	Value in modal space
v	Value in physical space
$\overline{\bigcirc}$	Modified variable

Acronyms

CFM	Clamped-Free Mast
CFP	Clamped-Free Prism
DAQ	Data Acquisition Analyzer
DOF	Degree of Freedom
EMA	Experimental Modal Analysis
EOM	Equation of Motion
EVD	Eigenvalue Decomposition
FDM	Force Density Method
FEM	Finite Element Method
FFP	Free-Free Prism
FFT	Fast Fourier Transform
FRF	Frequency Response Function
GA	Genetic Algorithm

LDV	Laser Doppler Vibrometer
MILP	Mixed Integer Linear Programming
NI	National Instruments
NRM	Newton-Raphson Method
SVD	Singular Value Decomposition
UAV	Unmanned Aerial Vehicle

Chapter 1

Introduction

1.1 Motivation

The fixed stiffness and structural properties of traditional aircraft wings can be a major constraint on performance. As the need for aircraft to fly efficiently across a wide range of conditions increase, there is a growing need for wings to be able to change their structural properties in flight. Having authority of a wing's structural properties would result in wings that are more receptive to control and offers an attractive way to integrate structural design with control system design. Aircraft wings that are capable of morphing their shape and/or changing their stiffness properties possess the potential for aeroelastic instability suppression and, as a result, would enable flight over a wide range of flight conditions.

Aeroelastic considerations, as well as understanding structural behavior, are of importance for safety as well as improved performance and maneuverability. Aeroelastic instabilities such as flutter and divergence, can cause operating limitations [3] or even structural failure due to the structure coupling with the aerodynamic loading. Design constraints are posed on aircraft to avoid repeating many well known aeroelastic failures [4]. For instance, NASA's Helios was an Unmanned Aerial Vehicle (UAV) that failed due to an aeroelastic phenomenon known as divergence [5].

In light of these issues, this research investigation is motivated by the need to develop a new class of aircraft wings that are more robust in the face of aeroelastic considerations. It is also hypothesized that the control and instability issues can be largely mitigated by leveraging structures with adaptable properties. Previous research considers Shape Memory

Alloys (SMAs) [6], flexible control surfaces, and a morphing trailing edge as potential ways of making aircraft wings more controllable and adaptable [7]. This work considers a class of structures known as tensegrities as another potential solution. Their strong, light-weight, flexible, tunable, and scalable features make tensegrities promising particularly for aerospace applications.

Tensegrities have adaptable structural properties and can morph shape by changing their cable tension. The ability to change configurations is another major advantage of a tensegrity-based framework, which would give a wing adaptable structural features and may offer an effective way to suppress undesirable vibrational response and/or aeroelastic instabilities. This also makes them potential candidates for morphing aircraft wings. Unlike traditional wings which have fixed structural properties, tensegrity wings offer controllable static and dynamic structural properties. They have also been shown to have the potential for 25-50% weight savings [8].

Tensegrities are a structural framework characterized by a combination of rigid struts in compression, linked together through cables in tension, and held together in a self-stabilizing equilibrium state [9]. In this way, the tensile members stabilize the configuration of the tensegrity structure without any external forces. When the internal and external forces of the system are balanced, a tensegrity structure exhibits mechanical stability, enabling the structure to withstand substantial loading and stress, while, at the same time, maintaining an exceptionally high strength-to-weight ratio. The term tensegrity was coined by Buckminster Fuller by combining the words "tension" and "integrity" [10].

The first documented tensegrity structure was built by artist Kenneth Snelson [10], famous for the "Snelson's X" tensegrity. Even though the structure has been known for over 50 years, little effort has been made to adapt it to engineering applications [9]. Previously, the most common considerations of tensegrity structures have been toys [9] and art [11]. However, now it is known that tensegrity-like structures exist in nature, such as in the human body, where the bones hold the compressive load and the tendons provide the tension for

stabilization [12].

Tensegrities are attractive structures because they handle loading by distributing forces axially through each member [9]. Consequently, members do not have to be designed to handle shear and bending forces [13]. Moreover, cables are strong in tension, lightweight, foldable, and can have a variable tension [14]. This means that the structural properties can be controlled by altering the tension in the structure's tensile elements. Actuators can be placed on cables to create an active structure [14]. Tensegrity structures can be changed substantially without requiring extra energy to hold them in a configuration [15]. They require less energy to manipulate [10] and are able to achieve multiple equilibrium positions. This could ultimately lessen the stress on a wing's structural components, and can ease the integration of an aircraft wing's control system. Additionally, the shape of a tensegrity structure can be changed with small changes of unstressed lengths of the members, which facilitates high precision control [14].

Figure 1.1: Tensegrity wing structure demonstration hardware made by Skelton [1]

An example static model of a tensegrity wing structure that was built by Skelton [1] is shown in Fig. 1.1. The tensegrity system incorporates a spar, ribs, and an airfoil profile similar to those which compose the framework of a traditional wing system. However, in this investigation, test articles will be built with the idea that the entire internal framework of a traditional wing could be replaced with the struts and actuated tensile cables of a tensegrity mast. The objective to this research is to investigate how the natural frequency changes

with varying cable tension in tensegrity prisms and masts.

1.2 Applications

Tensegrity structures have been considered in a wide variety of applications, from modeling cell behavior [16–18], including capturing the mechanical behavior of the cytoskeleton [19,20] and even viruses [20], to mimicking diaphragm motion [21]. They have also been considered in the context of robotics [8,22–24], space platforms [25], deployable systems [26–30] such as a deployable antenna [31]. Tensegrities have the potential to be compacted into very small volumes, which makes them attractive for deployment applications [14]. They can also be automatically deployed where cables can be tensioned to raise the structure from a collapsed state to a stable tensegrity position [9]. In the same way, the potential energy of stressed elastic cables can be used to deploy the structure into a stable configuration [9].

Tensegrity booms have also been considered. Booms are long, slender, lightweight, and deployable systems frequently used in space missions to accurately position payloads [32]. Typically, booms are structurally efficient, can be packed into a small volume and deployed, and the most mass efficient long booms have truss-like structural architectures, which make tensegrities ideal for this application [32].

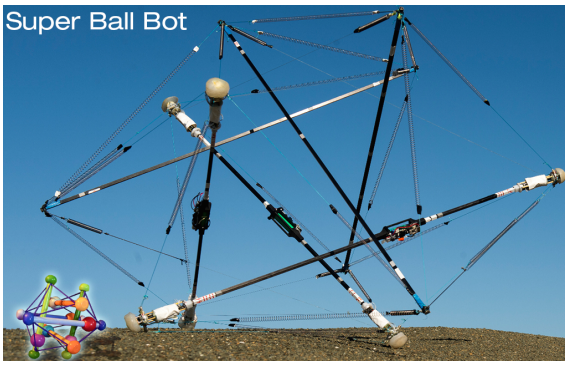

Figure 1.2: NASA's "SUPERball Bot"

NASA's Intelligent Systems Division are in the process of developing a collapsible, terres-

trial robot that has the potential to contribute toward space exploration goals. Rimoli [33] looks at the impact tolerance of tensegrities as planetary landers and remarks that an efficient structural design for a planetary lander should be able to evenly deform and store elastic strain energy during impact, which makes tensegrities attractive for the application. NASA's Super Ball Bot, shown in Fig. 1.2, is a six-strut tensegrity robot landing and mobility test platform. It is based on the expandable octahedron, a spherical tensegrity [24], with the purpose of enabling more reliable planetary missions. The advantages of using tensegrity systems for planetary surface explorers are that they are sturdier and can withstand substantial impact. Once on the planet, the cables can be adjusted to roll the bot in any direction, while data collecting devices or payloads are housed within its core. The robot is cable-driven, with 24 cables independently actuated by linear actuators [24]. Caluwaerts and Carbajal [13] shows the schematic of a robotic tensile actuator.

Other non-aerospace applications include civil structures, such as tensegrity pedestrian bridges [34–36].

1.3 Tensegrity types

Pin-jointed structures are generally classified as trusses or pre-stressed structures [37]. This can, in turn, be broken into two categories: tensile structures, such as cable nets, or cable-strut structures [37], such as tensegrity structures and tensegrity domes [29]. Tensegrity structures only exist under certain geometries [9]. Tensegrities may have as few as six members, such as Snelson's X, or as many as 90 members [38], though there is no limitation. Tensegrities can have continuously running cables, where the cables do not connect at the nodes. These are known as clustered tensgrities [39–41]. They are generally organized into categories, such as class, redundant [39]/non-redundant, symmetric, active/passive, and number of self-stress states. Redundant structures have reinforcing cables added to the structure.

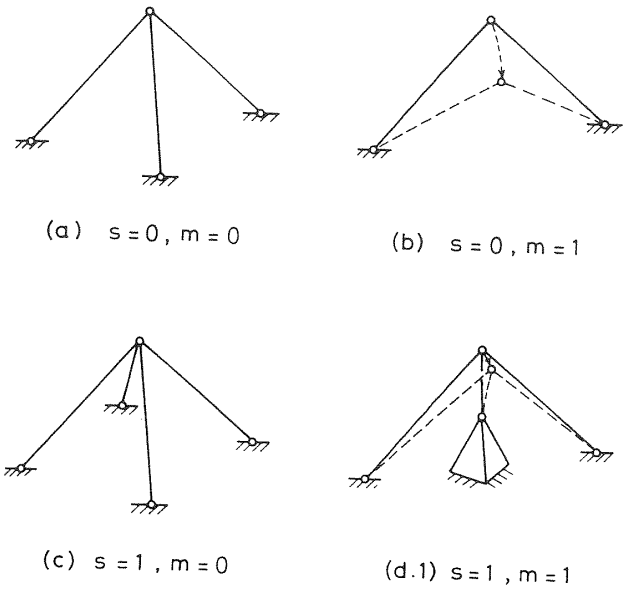

Figure 1.3: Static and kinematic determinacy and indeterminacy illustrations from Ref. [2]

Static and kinematic determinacy are central to an understanding of the mechanics of pin-jointed frameworks like tensegrity structures. Fig. 1.3, from Ref. [2], is used to visualize the meaning of self-stress states and internal mechanisms. In Fig. 1.3 (a), the tension in every strut can be determined by means of equations of equilibrium. Thus, this frame is statically determinate, since the number of nodal equations is equal to the number of unknown tensions, i.e., the solution is unique. Additionally, the frame is also kinematically determinate in the sense that the position of the joint is uniquely determined by the lengths of the struts.

Removing a strut results in a mechanism and the node can move as shown in Fig. 1.3 (b). The location of the joint cannot be uniquely determined by the length of the struts, so it is kinematically indeterminate. The assembly also has a mode of inextensional deformation. Meaning, it can distort without changing the length of any member.

Alternatively, an extra bar can be added to Fig. 1.3 (a) instead, as shown in Fig. 1.3 (c). Now the frame is still kinematically determinate but becomes statically indeterminate as there are now more unknowns than equations, and the solution for the tensions is not unique. The indeterminacy can be described as having a single state of self-stress. If the bar

redundant bar in Fig. 1.3 (c) is instead in a state of tension, the conditions of equilibrium would require other members to be stressed as well. This can be visualized by imagining that the new member is slightly shorter than the distance between the two joints it is connecting. Tension is then necessary to provide the small elastic elongation required to make it fit.

If a third bar is added to Fig. 1.3 (b), as in Fig. 1.3 (d.1), the frame becomes statically and kinematically indeterminante, moving with only small displacements of the inextensional mechanism. This is the case for tensegrity structures.

The most common tensegrities have symmetric properties, such as prismatic tensegrities [9, 25, 42–45], cylindrical tensegrities [42, 46, 47], tensegrity polygons [28], and spherical systems [28]. Zhang, et al. [48] investigate tensegrity structures with dihedral symmetry.

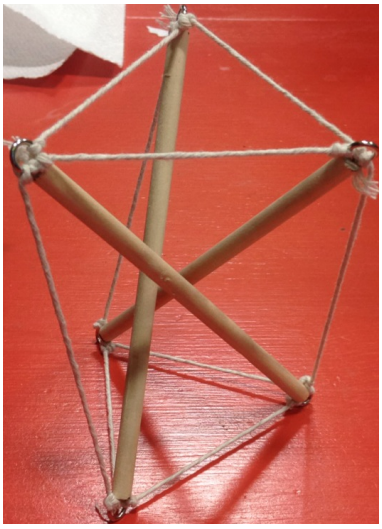

Figure 1.4: Tensegrity prism

Classic tensegrities are given names such as: the two-dimensional Snelson's X or "X-tensegrities" [37, 49, 50] (also referred to as tensegrity kites [25]), three-strut or prism tensegrity [9, 32, 49–52] (or sometimes referred to as "triplex" [42, 53]), shown in Fig. 1.4, four-strut tensegrity [54, 55] (sometimes referred to as "quadruplex" [42, 53]), hexagon [54, 55] as well as the three-dimensional six-strut tensegrity [51], octahedral cell [51], expandable octahedron [33, 42, 51, 54–57], and truncated icosahedron [42, 54, 56] and tetrahedral tenseg-

rity [42, 47, 54–59].

A class k tensegrity system has k strut(s) connected at one node [60]. A tensegrity system is considered to be class 1 if struts are free floating. Tensegrity prisms are class 1 tensegrities, while masts constructed of tensegrity prism units are class 2 tensegrities [32].

Tensegrity mast structures [26,32,61–64] are made up of multiple tensegrity units and, in turn, can be made into large-scale systems [65]. They have been considered in various contexts, including optimization [14,37,66,67], applied loading [61], as well as actuation [68,69]. Tensegrity masts can be both class 1 and class 2 [70]. For example, saddle-vertical-diagonal tensegrities [14, 27, 32, 71, 72] have one state of self-stress and one mechanism for any number of modules [14]. Planar tensegrities, such as the two-dimensional, three-module Snelson's X [14, 37, 73, 74], are class 2 tensegrities. There is a host of work relating to planar tensegrity structures [75–83]. Many theoretical studies are also applied to tensegrity beams [29,37,39–41,63,68,69,74,75,83–89]. A great deal of consideration is given to tensegrity towers [66,72,90], which have been frequently studied as booms [14,32]. In other works, tensegrity arches [16,90] are given some attention.

Modular structures [14, 32, 38, 50, 91], include a tensegrity grid structures [73, 91–97] or double-layer tensegrity grids [98]. They are constructed with modules or "cells" such as the octagonal cell and "four-strut" systems [87], also known four-plex module [74], quadruplex module [37,50], and Micheletti and Marcus tensegrity modules, both of which form stuctures with one state of self-stress [32]. Large scale tensegrity grids are advantageous because the failure of one of its components might not lead to an overall collapse [75]. Modules can also be connected together to obtain a larger tensegrity structure as in a beam [37, 86, 87], tower [99], and ring [59, 99], and space tensegrity structure [76]. Interestingly, a tensegrity tower, consisting of three struts per stage, sandwiched between rigid triangular plates and held in place by saddle, vertical, and diagonal cables, has the same equilibrium configuration but with a smaller number of unknown cable forces as the original structure, where the rigid plates are replaced by sets of three cables [71]. Refs. [39, 91, 95] construct a quadruplex

module to form a tensegrity beam, while Refs. [37, 73, 86] looks at a quadruplex module to form a double-layer quadruplex tensegrity grid, and a five-quadruplex module. It is worth noting that the behavior of modular tensegrity systems is known to be particularly similar to that of single cells [20].

Other types include irregular tensegrity structures [85, 100], such as membranes [49], fabric frameworks [101], or two-dimensional tensegrity airfoils [103]. The Geiger dome is a small-scale tensegrity made up of 32 nodes and 73 members [102]. Many methods noted in this work are also frequently applied to pin-jointed structures that are not necessarily pure tensegrities, such as cable domes [28, 104–106] or spoked-wheel roof structure [107].

Note that the definition of a tensegrity can become controversial when certain structures are included in its definition [59]. Structures, such as the one in Fig. 1.1, which do not follow the definition of a tensegrity, are referred to here as hybrid structures. Refs. [8, 29, 108] look at plate based tensegrity structures, which are a hybrid tensegrity, while Ref. [109] look at a plate constructed of prism units. Faulk and Tilbert [108] study plate tensegrity modules that are linked together to form a long plane plate tensegrity systems. Hybrid structures typically involve a more complicated process for modeling.

1.4 Current work

This work explores tensegrity systems as the framework for a tunable aircraft wing structure and analyzes the structural properties of a tensegrity mast with a representative wing-like geometry. This investigation is a first step towards addressing how choosing different cables to actuate changes the properties of tensegrity structures to prevent unwanted vibrational and aeroelastic behavior. This work demonstrates how control of the tension in the tensile elements of a tensegrity structure can enable robust control of the natural frequencies and modes. This work shows that the first two modes of a tensegrity structure can be separated by changing the length of the cables.

Most available studies for aerospace applications are concentrated on tensegrities in

space. Very few works explore tensegrity wing structures, with even fewer considering tensegrities for aeronautic applications. Research for the application of a tensegrity-based wing [41,64,68,69,110,111] so far is limited to shape-changing airfoils [103], tensegrity-based fins [112,113], swimmers [114], and a tensegrity spar [64].

Refs. [13, 52] explicitly state they are primarily concerned with the form-finding and analysis of class 1 tensegrity structures [49]. Previously, considerable research has been performed on the control, statics, and dynamics of class 1 tensegrities, with few studying class 2 tensegrities [77]. Additionally, though there is a plentiful amount of literature regarding tensegrity prisms, few build and experimentally test physical test articles. Refs. [14, 50] also consider a tensgrity prism mast; however, they are constructed of two and four modules rather than three.

This work applies the algorithms of Refs. [42, 54] to find an initial configuration with minimal inputs and then the algorithm discussed by Ref. [115] was used to model the new equilibrium configuration given a change of the lengths of certain cables. A modal analysis was conducted at each length-change increment. The process of determining the stable configuration for a set of tensegrity element lengths is a relatively unexplored form-finding problem. Several authors have developed various form-finding methods, but very few of them allow the member lengths to be directly controlled; nor do they provide a clear understand of how the lengths of the members affect the overall shape and dynamic properties of the tensegrity system [25]. This work formulates a new method for converting length changes into nodal coordinate changes. Tensegrity shape-change is successfully modeled with direct control of member lengths.

Experimental results are used to validate the theoretical model. Experimentally modal test a tensegrity mast for a range of cable lengths. Natural frequencies are identified for the test articles for a range of cable lengths. Four different actuation strategies are explored and their effects on the natural frequencies of the system are compared. In addition, this is the first work to explore how different boundary conditions influence the natural frequency

behavior of tensegrities and to compare the dynamic behavior of prisms with masts.

The thesis is organized as follows. First, linear algebra concepts are reviewed for better clarification of the algorithmic procedures. Next, the mathematical model is presented, where a form-finding and length-changing algorithm are explained. Then, the design and construction of the test articles is explained and the experimental procedure is outlined. Finally, the results are shown, analyzed, discussed, and compared with other similar works.

Contributions:

1. A large number of tensegrity types are presented by accumulating previous literature
2. A thorough literature review is performed and the pros and cons of previous form-finding methods applied to tensegrity structures are presented
3. Form-finding algorithm for tensegrity structures is presented clearly and the results from several numerical examples are shown
4. A method is shown for converting length changes into nodal position changes
5. First work to modal test tensegrity prisms and masts for various cable actuation strategies
6. First work to consider how the natural frequencies of tensegrity prisms and masts are impacted by length change
7. Results show the natural frequencies of tensegrity structures change the most for a vertical actuation strategy
8. Results show length change has more of an effect on higher modes of tensegrities

Chapter 2

Literature Review

The advantages of tensegrity systems come at the cost of design complexity [25]. Length can be calculated as the vector magnitude of the nodal coordinates, which involves a square-root term. Thus, the modeling of tensegrity structures can be cumbersome due to the nonlinearities [8].

2.1 Theoretical work

Most literature regarding tensegrity structures is purely theoretical and has not been validated experimentally. The majority of theoretical work completed on tensegrities so far perform mathematical modeling and theoretical analysis for simple tensegrity geometries. Regarding mathematics literature, Connelly and others have proved conditions for stability and rigidity properties of tensegrities (referred to in mathematical formulations as tensegrity frameworks) [10]. Tensegrities are commonly modeled with frictionless pin-joints, neglecting the self-weight of the members [42]. In some cases, tensile members are modeled as springs with a zero rest length [10, 15]. In general, tensegrity structures are primarily statically modeled, where form-finding is usually performed first to find their equilibrium shapes. This initial shape can then be changed to form new configurations. Quasi-static behavior is generally analyzed from here with the consideration of relatively low frequency dynamic loads [33].

Form-finding is known as the solution process which simultaneously determines the self-stressed equilibrium and corresponding geometry [74]. A form-finding problem has no closed-

form solution, and is instead examined for sufficient conditions. While there exists a tremendous amount of tensegrity form-finding literature, most of the proposed models can only be applied to specific types of tensegrities, such as symmetrical, only prismatic [25], equivalent tensile/compressive forces in all members, etc. Ali, et al. [39] present a modified dynamic relaxation (mDR) algorithm, with their approach explicitly applicable to clustered tensegrity structures, with continuous cables sliding over frictionless pulleys. Additionally, most works formulate their solution methods for specific types of tensegrities or are very computationally expensive or mathematically complex algorithms. Despite much development in form-finding analysis, most previous methods are efficient only for tensegrity structures of relatively small scale [44]. Most of the available methods have dealt with the form-finding of tensegrities for only the case of a single self-stress state [51, 58]. As Xu, et al. [116] points out, the MILP method (amongst many others) are formulated for and applied to Class 1 tensegrity structures only [29], in which one strut is connected to each node. There are little to no studies applying such method(s) to general class k structures.

Assuming the connectivity is known, the analysis and design of a tensegrity structure normally depends on two main variables: the position of the nodal coordinates and the prestress level of its members [74]. It is possible for both of these quantities to be unknown, the case which will be discussed later in this work. Ref. [117] takes a new approach where the connectivity matrix is the unknown variable. Again, this approach is limited because it can only be applied to two-dimensional tensegrities.

Form-finding methods

Form-finding methods for tensegrity systems can be classified into three categories: geometric, analytical, and numerical [59, 74]. Numerical methods are generally more practical for large, asymmetrical tensegrities, while analytical methods are merely appropriate for tensegrities with a high order of symmetry [19,74]. Deriving form-finding formulations for irregular tensegrity structures analytically is a difficult task [19].

The following form-finding methods do not include analytical methods, which are configuration specific. Pietila and Cohen [8] point out that solving, even a single cell with multiple DOFs, analytically can quickly become a difficult task. Thus, analytical methods are not practical for an engineer who does not have extensive amount of experience with solving the dynamics of complicated structures. These methods use specific equations to generate certain types of tensegrities, which have characteristic equilibrium configurations such as cylindrical [46] or prismatic tensegrities. Prismatic tensegrities can be calculated analytically by means of given criteria such as a special twist/rotation angle between the top and bottom polygons, strut-to-cable length ratios, or tension coefficients [71, 118]. Specifically, the geometry of prismatic tensegrities is given by the number of struts, lower and upper radii, height, and rotation angle. Similarly, if each of the six struts of an expandable octahedron tensegrity is divided into three pairs, the distance between each strut pair is equal to half the length of the strut [71]. However, building a structure around such criteria is not ideal in practice.

Traditional solvers, such as gradient-based solvers, are limited because the equilibrium tensegrity space is non-smooth, with the exception being Micheletti and Cadoni [28] who study tensegrity ballons due to the system's smooth behavior. They further remark that for more diverse situations, other form-finding and static analysis would be more effective.

The following presented methods can typically be used to solve a wide variety of problems; however, here they are compared as applied to tensegrity structures based on existing literature.

An iterative method is a mathematical procedure that starts with an initial guess at a solution and the i^{th} approximation is derived from the previous ones. In this way, the guess is continuously updated with approximate solutions that improve at each iteration until converging at the actual solution. Most existing iterative techniques for solving large linear systems of equations use a projection process in one way or another. Projection techniques are a way to extract an approximation to the solution of a linear system from a

subspace of $\mathbb{R}^n$. A subspace is a set of vectors that is closed under addition and multiplication by a scalar. A linear system is a set of linear equations that are considered collectively and solved simultaneously, rather than individually. The following presented methods are iterative procedures that are specifically applied to tensegrity structures.

There are many ways to go about an iterative procedure. For problems that require finding the root of an equation, one may use the Newton-Raphson Method (NRM). The NRM is an iterative method which uses an initial guess to generate successive approximations to a solution, where a correction term is introduced to the iterative equations [124].

Various considerations can be added onto any of these methods, including the consideration of momentum [10, 125], joint friction, gravitational effects, nonlinear stiffness, nonconservative forces, and path-planning [10, 78]. Additionally, procedures can be added to add external loading [97], account for buckling [28, 33, 145] or to constrain anything from nodes to geometrical constraints like shape [126], rotational symmetry [72], elevation [72], or a maximum allowed volume or mass. Additional geometric constraints cause the linearized problem to become nonlinear again, and are generally solved using gradient-based methods [121]. Optimizers can also be put in place to find desired configurations such as the topology that maximizes stiffness [96, 97], stiffness-to-mass ratio given loading, minimal mass configurations, preserved total cable length, minimization of deviation of member forces from target values [96, 97], or other desirable qualities. Optimization can be accomplished by using programming methods such as MILP [88] or algorithms such as gradient-descent or genetic/evolutionary.

Force density method

The Force Density Method (FDM) is one of the fundamental methods for finding new configurations of a tensegrity structure [126]. Any state of equilibrium can be obtained by the solution of one system of linear equations, constructed using member force-length ratios, called force densities, as degrees-of-freedom (DOFs) [128]. The FDM is an advantageous

Method	Description	Pros	Cons	Main EQs
Dynamic Relaxation Method (DRM) [11, 24, 38, 71, 98, 119–122] Modified Dynamic Relaxation Method (mDR) [39, 40]	•simulates dynamic behavior •node displacement traced over time until sum of residual forces in nodes converges to near "0" value •residual forces converted to velocities •uses fictitious damping with externally applied load •tracks kinetic energy of system over time	•lower computational cost •does not require stiffness matrix •attractive for structures with nonlinear geometric and material behavior •control over predefined stresses	•not as effective with many nodes •convergence dependent on choice of damping •"kinetic damping" $\left(K \neq \frac{f}{dx}\right)$ •no material specification	$\mathbf{f}_{\text{ext}}(t) = \left\{\mathbf{M}\ddot{\mathbf{p}} + \mathbf{C}\dot{\mathbf{p}}\right\} + \mathbf{f}_{\text{int}}(p)$ ${}^{i}\mathbf{r} = {}^{i}\mathbf{M}{}^{i}\dot{\mathbf{v}}(t) + {}^{i}\mathbf{C}{}^{i}\mathbf{v}(t)$ ${}^{i+1}\mathbf{u} = {}^{i}\mathbf{u} + \Delta\mathbf{t}{}^{i}\mathbf{v}$ $\text{KE}(t) = \sum_{i=1}^{n} \frac{1}{2} m_i \mathbf{v}_i(t) \cdot \mathbf{v}_i(t)$
Minimal cycle basis [56]	•combined form of equilibrium and geometrical compatability equations for tensegrity structures •considers connectivity as directed graph •generates compatability equations via cycle basis	•can be solved analytically or numerically •reduced computational effort	•found form requires symmetry •unfeasible solutions may arise for small lengths or force densities	$\mathbf{Aq} = \mathbf{0}$ $\mathbf{HD} = \mathbf{0}$
Newton-Raphson Method (NRM) [20, 28, 47, 59, 75]	•solves form-finding problem for tensegrities with linear elastic properties • shortens cables for large-displacement elastic analysis	•can find roots of function •potential for quadratic convergence	•fails at limit points •must compute derivative of function	${}^{i}\mathbf{x} = {}^{i}\mathbf{x} - \left[\frac{\partial \mathbf{f}}{\partial \mathbf{x}}\right]_{\mathbf{x}={}^{i}\mathbf{x}} \left({}^{i}\mathbf{f} - \mathbf{f}_0\right)$
Stiffness Matrix Form-Finding (SMFF) [44] Stiffness Matrix Method (SMM) [119, 123] Transient Stiffness Method (TSM)	•considers relation between total elastic strain energy and structural stiffness matrix •minimizes total potential energy •changes K positive definite after excluding rigid-body motions	•suitable for large-scale irregular tensegrities with large number of nodes •can specify external and internal loading	•starts from arbitrary position •must input number of nodes and members, structural topology, natural lengths, and axial stiffnesses of members	$U = \begin{cases} 0 & \ell \leq \ell_0 \\ \frac{1}{2}k(\ell - \ell_0)^2 & \text{o/w} \end{cases}$ $\mathbf{K} = \mathbf{S} + \mathbf{A} \cdot \text{diag}\left(\ldots, k\frac{\ell_0}{\ell}, \ldots\right) \cdot \mathbf{A}^{\text{T}}$
Monte Carlo Form-Finding (MCFF) [85]	•molecular simulations •tensegrity modeled as molecule •nodes and members modeled as atoms joined by atomic bonds, respectively •each step generates trial configuration by random sampling •accept-or-reject scheme depending on which has minimal energy	•good for large-scale tensegrities •does not require prior knowledge of nodal coodinates	•cannot specify nodal coordinates •takes hours to run on computer	$E = \begin{cases} 0 & \ell \leq \ell_0 \\ \frac{1}{2}k(\ell - \ell_0)^2 & \text{o/w} \end{cases}$

Table 2.1: Iterative/numerical form-finding methods for tensegrities

Method	Description	Pros	Cons	Main EQs
Force Density Method (FDM) [11,37,50,53,54, 71, 121, 126] Extended Force Density Method (EFDM) [127]. Non-Linear Force Density Method (NLFDM)	•based on a mathematical description of static equilibrium •tool for finding initial base geometry and initial pre-stressing set •mathematical transformation from nonlinear equilibrium equations into linear equations at nodes •each member has force density	•explores new non-degenerate and asymmetric formations •provides number of states of self-stress and internal mechanisms •provides stability analysis •results apply to any kind of material •finds super-stable tensegrities	•no direct control over member lengths or tension •works better for structures with one state of self-stress •difficult to constrain nodes •cables assumed to be massless •no material specification •force density results may differ (not unique) •hard to converge with negative eigenvalues	$\mathbf{D}\begin{bmatrix}\mathbf{x} & \mathbf{y} & \mathbf{z}\end{bmatrix} = \begin{bmatrix}\mathbf{0} & \mathbf{0} & \mathbf{0}\end{bmatrix}$ $\mathbf{Aq} = \mathbf{0}$
Force-Displacement Relationship [115]	•based on small displacement theory, assuming linear dependence of deflections upon applied forces •solves force-displacement equation by using EVD to convert between physical and modal space •uses NRM to iterate between nodal coordinates in modal space	•simple mathematical formulations •efficient computations •control over material properties •can be applied to any tensegrity class •allows for nodal (length) control	•not commonly used (limited information available) •certain structural changes may have convergence issues	$\mathbf{K}\Delta\mathbf{p}=\Delta\mathbf{f}$

Table 2.2: Iterative/numerical form-finding methods for tensegrities (used in this work)

form-finding method because it prescribes one single quantity, the force density, for each member and obtains as a unique result the appropriate state of equilibrium [128]. The force densities can be thought of as stresses [71]. It allows for many very different shapes to be computed and displayed in a short time [128]. Another advantage to the FDM is that it provides a linear solution to the shape-finding problem. In this way, the final shape obtained by the FDM is independent of the initial coordinates of the structures, and the controlling element variable is that of force density [129].

The analysis process of the FDM is relatively simple compared with other nonlinear methods such as the NRM or DRM [129]. However, this convenience has its drawbacks in that the outcome of the final stress distribution is difficult to control [129]. Another disadvantage is that once a form has been found, a new method must be put in place to analyze its response under loading [129]. The main limitation to this method is the inability to constrain nodes or to add external forcing. This is due to the nature of the form-finding problem, since the

procedure depends on the null spaces of the matrices. When nodes are constrained, this is essentially the same as adding external forcing. The known coordinates can be multiplied and subtracted to the other side of the equations, resulting in an equilibrium problem which is no longer formulated as a matrix times a vector equals zero. As will be seen in this work, the limitations of the FDM required the use of a second algorithm.

The FDM was originally proposed to solve the equilibrium equations for any type of cable net and has been extensively studied for tendon structures [49, 106, 129–132]. The set of linear equilibrium equations solving a cable net becomes indefinite when a negative force density is assign to compression members [131]. There are many ways to extend the cable net formulation of the FDM to tensegrity structures. The variational principle has been used to extend the FDM to structures with tension membranes and compression members [131]. Koohestani and Guest [56] formulate a form-finding for tensegiry structures based on the force density formulation. The difference between their formulation and the force density formulation is analogous to the difference between the force and displacement methods for structural analysis. In the displacement method, the equilibrium equations are written based on the stiffness matrix and the nodal displacements, which automatically satisfy compatibility conditions. In the standard force method, both the equilibrium and the compatibility conditions are written individually, based on elements' independent forces, and should be satisfied simultaneously [56]. An optimization method can be used to find the global minimum, leading to a set of force densities that guarantee the constrain conditions for the force density matrix [76].

General form-finding methods

The following methods presented here are broader categories of the previously presented form-finding methods. They are discussed specifically for tensegrity form-finding.

From a modeling perspective, symmetry is desired because it is useful for eliminating some unknowns. Symmetry properties are very commonly used for tensgrity form-finding [43, 133,

Method	Description	Pros	Cons	Examples
Variational Principle (Virtual Work) [49, 131]	•performs form-finding analysis by solving stationary problem of selected functionals •assumes only change in cable length during virtual displacement	•extends FDM	•can't specify lengths of cables, only struts •structure must be symmetric	SMFF TSM
Energy Minimization Methods [71, 96]	•based on Connelly's Rigidity Theory •when nodes are displaced, energy builds up as a function of the square of the extension •minimizes total potential strain energy	•finds irregular tensegrities •found structures are stable	•struts can go through each other •only considers symmetric configurations •constraint may not be differentiable at boundary of feasible region •difficulties applying nonlinear programming •does not consider self-weight nor external loading •topology must be known prior	MCFF
Static [9, 59, 71]	•searches geometric variations of a given topology •equilibrates imposed member forces	•knowledge of initial topology is not required	•not as effective with many nodes	FDM
Kinematic [9, 59, 71]	•lengths of cables/struts are kept constant while strut/cable lengths are increased/decreased until maximum/minimum is reached •residual forces converted to velocities •does not explicitly require cables be in pre-tension	•best if configuration details of structure are known •predefine lengths of cables and iteratively elongate struts until equilibrium is found •finds cable-to-strut length ratio	•not as effective with many nodes	L/QPM DRM
Genetic/ Evolutionary Algorithms (GA) [14, 52, 55, 58, 100, 117, 126, 136] Differential Evolution (DE) modified Differential Evolution (mDE) [74]	•global search technique based on survival of the fittest •finds global minimum •based on mechanics of natural selection and genetics •set of fitness criteria or fitness function/penalty system •connectivity matrix and force density vector encoded into two different chromosomes	•generates (small) irregular tensegrities without intuition or simple geometric shapes	•best if configuration details of structure are known •has trouble finding appropriate solutions and converging candidate solutions •not viable for large irregular tensegrities	EFDM
Gradient-Descent Algorithms [55]	•iterative optimization algorithm •finds minimum of function by stepping towards negative gradient	•simple •suitable for large models	•often trapped at local optimal solutions •stiffness matrix cannot be singular	NRM
Interactive methods [107, 137]	•allows users to interactively explore continuous space of valid structures	•more freedom selecting geometric constraints	•less control over model	Rhinoceros

Table 2.3: General methods applied to tensegrity form-finding

134]. Self-stress can be calculated using a symmetry-based method [135]. The majority of form-finding methods using the force density require symmetry properties so that the number of variables and, in turn, equilibrium equations can be reduced [20, 55].

Other form-finding methods include, geometric intersection method [25], where each set of member lengths defines a geometric surface, and the Parametric Variational Principle (PVP) method [89], developed for geometric nonlinear analysis of tensegrity structures based on the co-rotational approach. Lee and Lee [58] remove cables until the minimum number of cables are connected to give stability.

There are several ways the FDM has been combined with other analysis tools. Lee and Lee [140] combined the FDM with a GA, where the discontinuity condition of struts was used to select strut candidate groups from arbitrary members. Tran and Lee [86] considered the geometric and material nonlinearities of tensegrity behavior solving with a modified NRM.

Method	Description	Pros	Cons
Mixed Integer Linear/Quadratic Programming (MIL/QP) or Linear/Quadratic Programming Method (L/QPM) (linprog,quadprog) [78, 96, 99, 116, 138]	•numerical algorithm •used to solve structural optimization problems •extended to general class k tensegrity structures •maximizes number of struts over self-equilibrium condition of axial forces and discontinuity condition of struts •solves minimization problem of number of cables to remove redundant equilibriums	•always successfully finds best new q •used to solve structural optimization problems •does not require symmetry	•cannot specify lengths of cables, only struts •equations have to be manipulated to be in certain format •not guaranteed to produce stable tensegrity structures
Finite Element Method (FEM) [20, 33, 59, 75, 139]	•modifies single cable lengths such that total cable length is preserved and potential energy is minimized •computes equilibrium configurations for given cable lengths by computing gradient relating change of cable lengths to change of bar lengths •uses nonlinear Euler-Bernoulli beam element	•converges with very few iterations •successful for larger structures	•requires inputs of topology, undeformed bar lengths, total cable length, cable pre-stress, and bar stiffness •requires symmetry for imposing constraints
Reduced Coordinates [71]	•struts are constraints acting on cable structure •set of independent, generalized coordinates define position and orientation of struts •equilibrium equations are obtained by relating forces in cables and bars by virtual work	•useful for certain class of tensegrity towers	•requires symbolic manipulation software •not widely-used method
The Nelder-Mead simplex method [46, 124]	•solves global equilibrium problems •unconstrained optimization method for complex objective functions •solves nonlinear problem by examining objective function	•gradient-free	•based on grouping and symmetry

Table 2.4: General methods applied to tensegrity form-finding (continued)

Do, et al. [55] combine a new modified differential evolution (mDE) with the FDM, which is proposed as an efficient numerical algorithm for form-finding tensegrity structures. Similar to the FDM, the force densities of the tensegrity structures were determined by minimizing the objective function related to the eigenvalues. Similarly, Koohestani [134] approaches the form-finding problem of tensegrities as a minimization problem and formulates a special objective function often used in GAs, known as a fitness function based on the smallest eigenvalues of the force density matrix. Lu, et al. [57] use a coordinate-based FDM to form-finding for irregular tensegrity structures via matrix iteration, where the given coordinates are treated as a constraint condition. Ashwear and Eriksson [75] combined the FDM with the NRM by changing the unstressed length, using the NRM to iteratively solve for the new equilibrium, and then evaluating the natural frequencies. A very similar procedure is performed in this work.

The results in Ref. [55] show agreement with others in literature, with significantly lower computational time. Additionally, Ashwear and Eriksson [75] reduce the computational time for the FEM by using several beam elements for each compression member and a single beam for tensile members.

Shape/length-change

Tensegrities can function as shape-morphing structures [70,103]. Micheletti and Williams [90] use a method known as a Marching Procedure to transform a tensegrity tower into an arch. They propose an algorithm to numerically solve a set of differential equations and use the second-order stress test, a convenient condition that is stronger than the minimal-energy condition. The main goal of the research presented in Ref. [78] is to obtain preliminary insight into the possibilities of changing the shape of a tensegrity depending on the capability of changing a member's length. The work discusses several aspects of modeling tensegrity systems, addressing structural limitations in shape control, how the shape change requirements are formulated for actuator selection and control design purposes, and computational

Marching Procedure [90]	•discovers range of feasible geometries for topology of stable configuration •utilizes stability tests and rank deficiency manifold •lengths are control parameters •moves lengths along continuous path	•performs continuous length changes •can be implemented in Matlab •can reach configurations far from initial one •can be extended to large structures with multiple states of self-stress	•must start in stable position •many steps •cannot specify material properties •buckling and other instabilities must be considered separately •must avoid configurations with a high compression to tension ratio
Virtual Tensegrity Method [125]	•energy/momentum method •uses tensegrity models to synthesize and analyze the shape dynamics of multi-agent systems •each particle modeled as tensegrity node, members are attractive or repulsive forces for cables and struts, respectively	•enables shape change	•many steps/complex math •cannot impose constraints on length of members
Rank-Deficiency Manifold [15]	•based on characterization of rank-deficiency manifold •subset of cable lengths form local coordinate system on manifold •compatibility equations and orthogonality conditions form system of ordinary differential equations (ODEs) which give deformation rates of members as a function of nodal velocities	•cable lengths are control parameters	•ODEs must be solved using Runge-Kutta
Geometrical Variation Approach [15]	•iterative approach based on linearized form of underdetermined system of equilibrium equations •finds close variation to initial equilibrium geometry	•finds wide variety of irregular tensegrities •viable for design of tensegrities with special geometries or force distributions	•must start with structure already in equilibrium •only takes into consideration change in geometry •does not check stability

Table 2.5: Shape/length changing methods for tensegrities

results.

Nabet and Leonard [10] present a methodology that provides distributed control laws for tensegrity shape-change based on edge-length constraints; however, this is formulated specifically for arbitrary planar shapes. Based on an active tensegrity concept, Pietila and Cohen [8] develop a method for camber-morphing control of an airfoil, which enables maneuvering without conventional control surfaces [8]. Henrickson, et al. [103] look at morphing a tensegrity-based airfoil. The scope of theoretical literature regarding tensegrity control is especially dominated by Skelton's work [109].

Dalilsafaei, et al. [14] study various active tensegrity booms to understand how the num-

ber of actuators achieves bending stiffness enhancement, while Safaei, et al. [32] elaborate on this work and extend the comparison to even more types of booms, including a prism mast. In both of these works, the bending stiffness of various tensegrity booms are compared with each other as well as against truss boom systems. The stiffness properties are compared for different boom configurations for various geometry and loading cases [14]. It is found that tensegrity booms are most flexible when subject to bending loads [14]. Safaei, et al. [32] further expand Dalilsafaei, et al. [14] by quantifying how much more flexible a slender tensegrity boom is compared to a state-of-the-art truss boom and explain why some tensegrity topologies are more flexible than others.

Dalilsafaei, et al. [14] showed that, even when actuators are placed in different positions for both structures, the Snelson mast was still easier to control than the prism mast, a discovery which is attributed to the number of self-stress states. Additionally, the struts of the prism mast face buckling, while those in the class 1 Snelson mast do not [14]. While control difficulty is a disadvantage of tensegrity structures with more than one state of self-stress, for the design of a 60 m tall tensegrity tower, a class 2 tensegrity topology was selected over a class 1 as the latter would not provide sufficient stiffness [32]. Dalilsafaei, et al. [14] show that without actuators the tensegrity prism mast is stiffer than the Snelson; however, after actuation, the Snelson tensegrity mast shows higher stiffness.

Structural dynamics

Only a few studies are devoted to dynamic response and behavior of a tensegrity [75]. Lee and Lee [37] investigate identification of pre-stress levels via a GA to maximize the natural frequencies of tensegrity structures with an equilibrium constraint. The proposed method does not take into account boundary conditions or external loading. Safaei, et al. [141] present a method applicable for designing tensegrity structures when the natural frequencies are a major criteria. Faroughi and Tur [142] present an algorithm that will obtain optimum design parameter values of tensegrity structures which satisfy desired vibration properties.

Pilade Foti, et al. [84] use a GA to identify the pre-sress levels by maximizing natural frequency and imposing an equilibrium constraint. Caluwaerts and Carbajal [13] explore the tuning of the natural frequencies of redundant tensegrity structures with zero net mechanical work. Ashwear, et al. [50] aim to find the optimum internal force distribution, such that the lowest sensitive natural frequency of the structure is as high as possible and well separated from the next higher one [50].

A few vibrational analyses have been conducted on tensegrity systems [142, 143]. It is clear from the literature that the natural frequencies of tensegrity structures are affected by design parameters such as member cross-sectional area [75]. There is a host of theoretical work related to the effect of tension on the natural frequencies of tensegrities. Lee and Lee [37] show the relationship between the natural frequency and the level of pre-stress for a two-module Snelson's X. This plot shows that the natural frequency is constant with a slight increase just before cable yield. Faroughi and Tur [142] show the first three mode shapes of a three-module Snelson's X tensegrity structure and show how the first three natural frequencies vary with the level of pre-tension in the structure. Ashwear and Eriksson [75] investigate the relationship between the lowest natural frequencies and the level of pre-stress for the X-frame tensegrity and tensegrity beam and show coinciding frequencies. Safaei, et al. [141] show how the first three natural frequencies increase with increasing pre-stress level for symmetric patterns. Ashwear, et al. [50] investigate the sensitivity of the first natural frequency to the level of pre-stress in tensegrity structures and find that they can be high or low depending on the design. Thus, it is not always possible to use the first natural frequency as an indicator of the pre-stress level [50]. Ashwear, et al. [50] also note that there are certain frequencies which are particularly sensitive to pre-stress level. Ashwear, et al. [75] see the natural frequencies as nonlinear functions of introduced pre-stress.

Attig, et al. [102] determine a damping ratio of 5% for tensegrity prisms and find that the first mode is torsion and the second is bending. Contradictorily, Bossens, et al. [146] display the mode shapes for the first four natural frequencies of their FEM, which show

bending motion for the first family of modes and torsion for the next. Faroughi and Lee [73] look at the natural frequencies and mode shapes of a double layer tensegrity grid under external loading, with and without damping and slackening. Oppenheim and Williams [143] investigate the nonlinear vibrations of a tensegrity structure that is excited particularly in the direction of infinitesimal flex and the implications of the role of damping for the design of tensegrity structures is discussed for space applications.

Safaei, et al. [32] find that the Snelson and prism masts have the higher first natural frequencies, compared to the Marcus and Micheletti tensegrity masts. Considering only linear dynamics around a given equilibrium state without no external loading, the natural frequency results of Safaei, et al. [32] show that the tensegrity masts are at least one to three orders of magnitude more flexible than a regular truss. The study in Ref. [32] aims to provide a broader picture of the linear dynamic characteristics of tensegrity booms of different topology complexity, number of states of self-stress, and number of infinitesimal mechanisms. Safaei, et al. [32] use the fundamental natural frequency to compare performance of various tensegrity boom structures; the boom with the highest first fundamental frequency has the best deployed structural performance.

Ashwear, et al. [75] look at the first several natural frequencies of tensegrity systems with struts near buckling, focusing particularly on structures where the compressive member behavior dominates the response. Three specific planar tensegrities are studied, all of which are two-dimensional structures. A frequency approaching zero most likely indicates that at least one strut is approaching buckling. They improve current models for resonance frequency simulation of tensegrities by introducing bending behavior and by one-way couping axial force with stiffness, focusing on a tool for anticipating the collapse of tensegrity structures. Ashwear, et al. show the first four mode shapes at buckling, as well as the evolution of the six lowest natural frequencies with increasing cable pre-stress (from 0 kN to about 52 kN) as the struts approach buckling. These natural frequencies coalesce at around 45 kN, which is attributed to symmetric behavior. If the lengths are further decreased, the six

lowest natural frequencies no longer coincide, but approach zero. Additionally, many of the natural frequencies in Ref. [75] are seen to be overlapping, referred to as modal "families" in this work; particularly, modes one through four and modes five and six overlap. The two-dimensional tensegrity "X" beam was tuned from 1×2.8 m^2 to 1×3 m^2 [75].

There has been a small amount of effort contributing to vibration control [109, 144]. Averseng, et al. [92] present a mixed dynamic control law for the displacements and vibrations of a tensegrity plane grid.

2.2 Experimental work

Several static tensegrity test articles have been constructed; however, nearly all of them are class 1 (easier joint construction), and the ones that are higher than class 1 are constructed such that the member lengths cannot be easily adjusted. Michielsen, et al. [145] consider the undamped modes of a base excited tensegrity prism test article under varying top masses. They found that top mass plays a role in the tensegrity dynamics. Refs. [93, 94] model and fabricate a tensegrity grid. There are various materials used for constructing tensegrities such as carbon fiber struts and steel cables [38]. Lu, et al. [57] construct a tensegrity joint and use a turnbuckle. However, this is used simply for prototype construction and not for adjusting tension.

Few experimental studies for tensegrity structures have been observed to be of practical significance and mainly small, simple and symmetrical tensegrity models are tested [122]. Ali and Smith [122] note that neither modal identification nor experimental testing under dynamic loads for tensegrities of multiple self-stress levels could be found in literature.

Ali and Smith [122] investigate the vibration control of a full-scale, active, tensegrity grid structure. Natural vibration modes of the tensegrity structure are identified experimentally and compared with those determined through a finite element model. Dynamic behavior is experimentally investigated through testing under dynamic excitation [122]. Laboratory testing is carried out for multiple self-stress levels and for different excitation frequencies.

The dynamic behavior of the structure is also numerically simulated. Vibration control is then carried out by modifying the pre-stress level of the structure through contractions and elongations of active struts in order to shift the natural frequencies away from excitation. The tensegrity pre-stress level was controlled through one millimeter increments of elongations and contractions of active struts. Ref. [109] also conducts a similar experiment to study the vibration control of tensegrities. Chang, et al. [109] present an experimental study of strategies for damping control.

Ali and Smith [122] conduct a dynamic analysis of a five-module tensegrity structure and shows that the linearized dynamic model offers a good approximation for its nonlinear behavior. The testing involved exciting the tesegrity structure and measuring the vibration response. A single point dynamic loading was applied using an electro-mechanic shaker and vertical displacement measurements were taken at the top surface nodes of the structure. Prakash uses accelerometers to collect time-domain analysis data; however, only the theoretical analysis is found to be reliable [94]. Bossens, et al. [146] use accelerometers to measure the response of a tensegrity structure excited by a mechanical shaker. Angellier, et al. [93] use strain gages to experimentally check the validity of using indirect measurement techniques to measure the loading in each member. They found that beam modeling poorly represented the real tensegrity behavior, especially for weak loads [93].

There have been several experimental investigations looking at how the pre-stress level of tensegrity masts affects the vibrational response. Rhode-Barbarigos [147] experimentally tests an active deployable tensegrity "hollow-rope" foot bridge and concludes that the fundamental frequency is not directly influenced by the pre-stress level but rather by the absence of infinitesimal mechanisms in the tensegrity system. Bossens, et al. [146] show how the first four natural frequencies vary with the level of pre-tension in the structure and note that the first natural frequency is a "soft" mode, meaning it starts at zero and increases. Ali and Smith [148] look at the evolution of the first natural frequency with respect to pre-stress level of a full scale active tensegrity structure and use vibration control to shift natural fre-

quencies away from excitation. Vibration tests were performed by Ali and Smith [122] for different pre-stress levels to identify the relationships between the tensegrity pre-stress level and its dynamic behavior. They found that decreasing the active strut lengths has the effect of reducing the natural frequency of the first resonance mode. Angellier, et al. [93] look at the evolution of the natural frequency according to the pre-stress level for four different boundary conditions and find that the first frequency mode is proportional to the square root of the tension of the element linked to the pre-stress level and the remaining modes are quasi linear and weak.

While these studies effectively establish a relationship, none of them explore how varying the length of the cables of a tensegrity influences the natural frequencies of the structure. None of these works look at length changes, only tension changes. Changing lengths means that the static equilibrium shape changes.

Tensegrity structures contain more tensile members than compressive, and thus the structure predominantly experiences a tension force [9]. Likewise, the tensile members will produce a larger contribution to the overall structure's bending stiffness [14]. This suggests that the vibration response of a tensegrity structure is primarily dictated by the amount of tension in the tensile members. Safaei, et al. [32] show that the first natural frequency can be raised by increasing the cross-sectional areas of cable members. Similarly, this work investigates how much the separation of the first two natural frequencies changes based on changing cable tension.

The response of a tensegrity to loading and excitation is strongly dependent on pre-stress. Most works state that the natural frequencies of a tensegrity structure increase with increasing pre-stress; however, without quantifying to what extent this is true. Ashwear and Eriksson [75] show that the lowest natural frequencies of a tensegrity system can not only increase but decrease as well with increasing pre-stress. A tensegrity may, at first, have cable dominated behavior in which pre-stressing will raise the lowest natural frequencies; however, up to a limit, any further increase in pre-stress will lead to a strut dominated response, where

the frequencies now decrease. Thus, it is worth investigating where this behavior changes during the tensioning process. This decrease could also be caused by certain geometries and materials in which pre-stressing may decrease the stiffness. Ref. [75] notes that, in addition to the lowest resonance frequencies, higher frequencies should be considered as they provide further information about the system. Thus, a spectrum of natural frequencies should be used as indicators for tuning the tenesgrity structure towards a target design [75].

Chapter 3

Linear Algebra Concepts

This chapter provides a brief overview of the mathematical concepts used for the linear algebra of pin-jointed structures.

3.1 Null space and rank deficiency

The null space is useful for solving a system of homogeneous equations. The vectors within the null space of a matrix, say example matrix $\mathbf{E}$, are all of the vectors that, when multiplied with $\mathbf{E}$, yield $\mathbf{0}$. So, example vector $\mathbf{h}$ is in the null space of $\mathbf{E}$ if

$$\mathbf{E}\mathbf{h} = \mathbf{0} \ . \tag{3.1}$$

When $\mathbf{E}$ is rank deficient, there is at least one free variable because at least one of the rows is linearly dependent [149]. A null space is present for a matrix when the matrix is rank deficient. The rank of example matrix $\mathbf{E}$ is the number of rows in $\mathbf{E}$ that are linearly independent [149]. A distinction should be made here between the null space, the one or more column vectors, and the dimension of the null space N, i.e., the number of column vectors in the null space.

Rank deficiency indicates that there exists a zero eigen- or singular value. This means that, for tensegrity structures, there is more than one equilibrium point, i.e., a line of equilibrium points pointing in the direction of the eigenvector associated with the zero eigenvalue.

Every homogeneous system has at least one solution. Notice that if we assume $\mathbf{E}$ in

Eq. (3.1) is nonsingular (i.e., has an inverse, $\det(\mathbf{E}) \neq 0$) and multiply both sides by $\mathbf{E}^{-1}$, then $\mathbf{h} = \mathbf{0}$ is the unique solution. However, this solution does not provide any information about the system and is referred to as the trivial solution. To achieve a non-trivial solution, it should be enforced that $\mathbf{h} \neq \mathbf{0}$. For this to be true mathematically, $\mathbf{E}$ must be singular, i.e.,

$$\det(\mathbf{E}) = 0 \ . \tag{3.2}$$

If $\mathbf{E}$ is singular, the linear system of equations has infinitely many solutions. This is because inverting any matrix involves dividing by the matrix determinant; however, dividing by zero is undefined.

3.2 Matrix decompositions

Matrix decomposition can solve a homogeneous system. It is a way to discover the vector $\mathbf{h}$ (and perhaps other vectors) that are in the null space of $\mathbf{E}$. Many problems present themselves in terms of an eigenvalue problem:

$$\mathbf{E}\mathbf{h} = \lambda\mathbf{h} \ , \tag{3.3}$$

where λ is an eigenvalue of $\mathbf{E}$, and $\mathbf{h} \in \mathbb{R}^k$ is an eigenvector of $\mathbf{E} \in \mathbb{R}^{k\times k}$. This equation means that under the action of a linear operator $\mathbf{E}$, the vector $\mathbf{h}$ is converted to a collinear vector $\lambda\mathbf{h}$. In other words, the goal is to find $\mathbf{h}$ such that $\lambda\mathbf{h}$ and $\mathbf{E}\mathbf{h}$ point in the same direction. If $\lambda = 0$, then $\mathbf{E}\mathbf{h} = 0$, meaning the eigenvector $\mathbf{h}$ corresponding to the eigenvalue 0 is a vector in the null space of $\mathbf{E}$, and $\mathbf{h}$ is arbitrary. Note that when λ is zero, Eq. (3.3) becomes Eq. (3.1). Hence, the solution vectors $\mathbf{h}$ to the homogeneous system correspond to a zero eigenvalue.

If $\mathbf{h}$ is nonzero, this problem will only have a solution if

$$\det\left(\mathbf{E} - \boldsymbol{\lambda}\mathbf{I}\right) = 0 \ . \tag{3.4}$$

In general, the eigenvectors are not unique, and any linear combination of the eigenvectors will also satisfy the original matrix equation. They are not unique because the matrices considered here are singular, i.e., there is a "free" variable. The number of equations must be equal to the number of unknowns if the solution is to be unique [2]. Expanding Eq. (3.4) gives the characteristic equation:

$$a\lambda^N + a_1\lambda^{N-1} + \cdots + a_j\lambda^{N-j} + \cdots + a_{N-1}\lambda + a_N = 0 \ , \tag{3.5}$$

which can be used to solve for the eigenvalues λ. Once the eigenvalues have been found, the eigenvectors $\mathbf{h}$ can be solved from

$$\left(\mathbf{E} - \lambda\mathbf{I}\right)\mathbf{h} = 0 \ . \tag{3.6}$$

$\mathbf{E}$ can be decomposed using the EVD, such as

$$\mathbf{E} = \mathbf{h}^{\mathrm{T}}\mathrm{diag}(\boldsymbol{\lambda})\mathbf{h} \ , \tag{3.7}$$

Similarly, the Singular Value Decomposition (SVD) of $\mathbf{E}$ is

$$\mathbf{E} = \mathbf{U}^{\mathrm{T}}\mathrm{diag}(\boldsymbol{\mu})\mathbf{W} \ , \tag{3.8}$$

Numerical solutions to a homogeneous system can be found with the SVD. Koohestani and Guest [56] use the SVD to determine the solution to minimizing the 2-norm of the residual forces. Based on this decomposition, the best approximation is found using the column vectors $\mathbf{w}$ of $\mathbf{W}$ associated with the smallest singular values $\boldsymbol{\mu}$ [56]. Generally, the EVD is preferred because the matrices it produces indicate a lot of properties about the system. However, it cannot be applied to rectangular matrices. Instead, the SVD is used in a similar

manner, to obtain an orthonormal basis [56].

The SVD is connected to the EVD in that each column vector in $\mathbf{U}$ is also an eigenvector of $\mathbf{E}\mathbf{E}^{\mathrm{T}}$ and each column vector of $\mathbf{V}$ is an eigenvector of $\mathbf{E}^{\mathrm{T}}\mathbf{E}$ (essentially two versions of $\mathbf{A}^2$). It can be shown with increasing power of $\mathbf{E}$ that the eigenvalues raise to the same powers. For further reading on the details and derivations of these decompositions, the reader is referred to Ref. [149]. More information regarding matrix decomposition theory and the applications of linear algebra for tensegrities can be found in Refs. [62, 148].

3.3 Linear dependence and degeneracy

The dimension of the null space can also be seen as the number of linearly dependent rows in a matrix. Thus, matrices are made up of two kinds of row/column vectors: linearly dependent and linearly independent. If two vectors are dependent, then one is a scalar multiple of the other. This means only one vector could be used to represent both vectors, therefore, one may be omitted. Alternatively, principal components may be used to replace a set of collinear variables with one or more orthogonal components.

Mathematically, degeneracy can be best illustrated by inspecting Eq. (3.1). If $\mathbf{E}$ is a system such that all the entries in each row sum to zero, $\mathbf{h} = \mathbf{1}$ (or any vector with the same value for every entry) will solve Eq. (3.1). To achieve a valid form-found structure, it must be non-degenerate. Geometrically, this means the structure is truly three-dimensional and will not collapse into a lower dimension. For this to be true, there are certain necessary rank deficiency conditions that must be satisfied [54].

3.4 Change of a matrix basis

A basis is the fewest number of vectors that can be multiplied by a coefficient to reproduce another vector. The standard basis for a vector $\mathbf{v}$, say

$$\mathbf{v} = \begin{Bmatrix} 3 \\ 3 \\ 1 \end{Bmatrix},$$

would be

$$\begin{Bmatrix} 1 \\ 0 \\ 0 \end{Bmatrix}, \begin{Bmatrix} 0 \\ 1 \\ 0 \end{Bmatrix}, \begin{Bmatrix} 0 \\ 0 \\ 1 \end{Bmatrix},$$

because

$$\begin{Bmatrix} 3 \\ 3 \\ 1 \end{Bmatrix} = c_1 \begin{Bmatrix} 1 \\ 0 \\ 0 \end{Bmatrix} + c_2 \begin{Bmatrix} 0 \\ 1 \\ 0 \end{Bmatrix} + c_3 \begin{Bmatrix} 0 \\ 0 \\ 1 \end{Bmatrix},$$

where $c_1 = 3$, $c_2 = 3$, and $c_3 = 1$. In matrix notation:

$$\overbrace{\begin{Bmatrix} \mathrm{v}_1 \\ \mathrm{v}_2 \\ \mathrm{v}_3 \end{Bmatrix}}^{\mathbf{v}} = \overbrace{\begin{bmatrix} 1 & 0 & 0 \\ 0 & 1 & 0 \\ 0 & 0 & 1 \end{bmatrix}}^{\mathbf{B}_1} \overbrace{\begin{Bmatrix} c_1 \\ c_2 \\ c_3 \end{Bmatrix}}^{\mathbf{c}}.$$

Similarly, $\mathbf{v}$ can also be written in a new basis

$$\begin{Bmatrix} 1 \\ 1 \\ 0 \end{Bmatrix}, \begin{Bmatrix} 0 \\ 0 \\ 1 \end{Bmatrix},$$

as

$$3 \begin{Bmatrix} 1 \\ 1 \\ 0 \end{Bmatrix} + \begin{Bmatrix} 0 \\ 0 \\ 1 \end{Bmatrix}.$$

So, in vector notation:

$$\begin{Bmatrix} 3 \\ 3 \\ 1 \end{Bmatrix} = c_1 \begin{Bmatrix} 1 \\ 1 \\ 0 \end{Bmatrix} + c_2 \begin{Bmatrix} 0 \\ 0 \\ 1 \end{Bmatrix},$$

where $c_1 = 3$ and $c_2 = 1$. In matrix notation:

$$\overbrace{\begin{Bmatrix} v_1 \\ v_2 \\ v_3 \end{Bmatrix}}^{\mathbf{v}} = \overbrace{\begin{Bmatrix} 1 & 0 \\ 1 & 0 \\ 0 & 1 \end{Bmatrix}}^{\mathbf{B}_2} \overbrace{\begin{Bmatrix} c_1 \\ c_2 \end{Bmatrix}}^{\mathbf{c}}.$$

So, we want to find $\mathbf{c}$ that will satisfy $\mathbf{v} = \mathbf{Bc}$, i.e., $\mathbf{c} = \mathbf{B}^{-1}\mathbf{v}$. If B_1 is the standard basis, then changing from B_1 to B_2 is geometrically equivalent to starting with a definition of the x, y, and z axis, and then defining a new set of axes. For example, a "fast" basis change for a Fourier transform is an FFT. The EVD and SVD are essentially ways to write a system in a new basis.

It is possible to choose any basis, but a basis cannot contain the $\mathbf{0}$ vector. For $\mathbf{B}$ to be a good basis, it must be easily invertible. It is known that a matrix is easily invertible if the basis vectors are orthogonal. Furthermore, a matrix with orthonormal columns is attractive because its inverse is the same as the transpose, an operation which is advantageous for computing speed. If $\mathbf{v}_1$, $\mathbf{v}_2$, and $\mathbf{v}_3$ are orthogonal vectors this means they are mutually perpendicular, i.e. $\mathbf{v}_1 \cdot \mathbf{v}_2 = 0$, $\mathbf{v}_2 \cdot \mathbf{v}_3 = 0$, and $\mathbf{v}_1 \cdot \mathbf{v}_3 = 0$. In other words, these vectors form an orthogonal basis with respect to the standard dot product on $\mathbb{R}^3$. The eigenvectors from the EVD form an orthogonal basis of $\mathbb{R}^3$ and the singular vectors from the SVD form an orthogonal basis of $\mathbb{R}^3$, as well.

Chapter 4

Form-Finding Algorithm

The choice of form-finding method depends on the availability of initial information and the complexity of the structure [126]. Techniques with minimum parameters are highly sought after [126].

An objective function can be minimized directly by obtaining an optimal null space vector or the nearest valid solution via projection [13]. Therefore, a gradient descent algorithm is not required here because the null space vectors are made available for use.

The presented form-finding algorithm is based on the Force Density Method (FDM) [71]. However, for the case of tensegrities, compressive members are added. In general, the equilibrium equations of cable-strut structures are highly coupled nonlinear equations. For example, displacing one node will change the tension in each cable which causes all the other nodes to displace. Thus, the force density (also known as the tension coefficient) is a quantity that is commonly used to linearize the equilibrium equations [53, 54]. It represents a member's internal axial force per unit length. For tensegrities, the FDM assumes the struts are rigid bodies and the cables are massless.

According to Harichandran and Sreevalli [126], the FDM is the most appropriate method out of all form-finding methods to discover new formations of tensegrity structures with the fewest input parameters. This method is found to be suitable for regular tensegrity structures and is generally applied to cable domes [126]. However, the possibility of this method for structures involving a large number of members and/or complex constraints needs further investigation [126].

4.1 Equilibrium equations

To differentiate between nodes and members in text, an 'N' will precede nodal numbers and an 'B' will precede member numbers. Fig. 4.1 shows node N1 connected by member B1 to node N2 and to N3 by member B2. This illustration is used to derive the equilibrium equations which relate the internal force of each element to the balance of the forces at the nodes.

Derivation

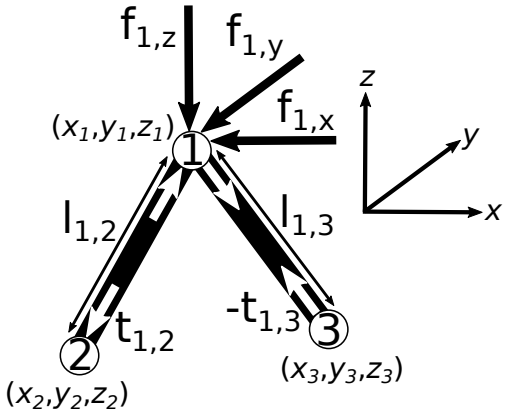

Figure 4.1: FBD of nodes 1, 2, and 3

The Free Body Diagram (FBD) in Fig. 4.1, indicating the direction of the internal force vectors in three-dimensional space, is used for the following derivation. It shows the x, y, and z coordinates for three nodes, internal force t, and length ℓ for two members, with external forces f. The coordinate system is shown to indicate the sign convention of the external forcing. Assuming no nodes are constrained, the corresponding set of equations of static equilibrium is given by summing the forces contributed by the members at each node. The equations for N1 are, for example

$$
\begin{aligned}
(x_1 \text{ - } x_2)\,\tfrac{t_{1,2}}{l_{1,2}} + (x_1 \text{ - } x_3)\,\tfrac{t_{1,3}}{l_{1,3}} + \cdots + (x_1 \text{ - } x_p)\,\tfrac{t_{1,p}}{l_{1,p}} &= f_{1,x}\ , \\
(y_1 \text{ - } y_2)\,\tfrac{t_{1,2}}{l_{1,2}} + (y_1 \text{ - } y_3)\,\tfrac{t_{1,3}}{l_{1,3}} + \cdots + (y_1 \text{ - } y_p)\,\tfrac{t_{1,p}}{l_{1,p}} &= f_{1,y}\ , \\
(z_1 \text{ - } z_2)\,\tfrac{t_{1,2}}{l_{1,2}} + (z_1 \text{ - } z_3)\,\tfrac{t_{1,3}}{l_{1,3}} + \cdots + (z_1 \text{ - } z_p)\,\tfrac{t_{1,p}}{l_{1,p}} &= f_{1,z}\ ,
\end{aligned}
\tag{4.1}
$$

where f is an external force vector with components f_x, f_y, and f_z. The subscript p is the number of members connected to node N1. Any b member, defined by the connection of two nodes, has an internal force t_b and a length l_b. In the FDM, Eq. (4.1) is linearized by defining a new variable q for the force density, which is a ratio of the member's tension to its length, i.e., $q_b = \frac{t_b}{l_b}$. Hence, now length is only dependent on the nodal coordinates, and q correspondingly scales according to this length. In other words, each member of the structure carries a force that is measured by its magnitude q. Substituting and distributing q through the systems in Eq. (4.1), they can be rearranged as

$$
\begin{aligned}
\left(q_{1,2} + \cdots + q_{1,(p\text{ - }1)} + q_{1,p}\right)\ \mathrm{x}_1 \text{ - } q_{1,2}\ \mathrm{x}_2 \text{ - } \ \ldots\ \text{ - } q_{1,(p\text{ - }1)}\ \mathrm{x}_{(p\text{ - }1)} \text{ - } q_{1,p}\ \mathrm{x}_p &= f_{1,x}\ , \\
\left(q_{1,2} + \cdots + q_{1,(p\text{ - }1)} + q_{1,p}\right)\ \mathrm{y}_1 \text{ - } q_{1,2}\ \mathrm{y}_2 \text{ - } \ \ldots\ \text{ - } q_{1,(p\text{ - }1)}\ \mathrm{y}_{(p\text{ - }1)} \text{ - } q_{1,p}\ \mathrm{y}_p &= f_{1,y}\ , \\
\left(q_{1,2} + \cdots + q_{1,(p\text{ - }1)} + q_{1,p}\right)\ \mathrm{z}_1 \text{ - } q_{1,2}\ \mathrm{z}_2 \text{ - } \ \ldots\ \text{ - } q_{1,(p\text{ - }1)}\ \mathrm{z}_{(p\text{ - }1)} \text{ - } q_{1,p}\ \mathrm{z}_p &= f_{1,z}\ .
\end{aligned}
\tag{4.2}
$$

Converting to vector/matrix form

The member force density coefficients vector $\mathbf{q} \in \mathbb{R}^b$ is defined as

$$
\mathbf{q} = \frac{\mathbf{t}}{\boldsymbol{\ell}},
\tag{4.3}
$$

where $\mathbf{t} \in \mathbb{R}^b$ is the member internal force vector, whose entries are $+t$ for tensile members and -t for compression members, and $\boldsymbol{\ell} \in \mathbb{R}^b$ is the member length vector.

A node is defined at each pin-joint of the tensegrity structure, i.e., the points at the ends of the struts. The nodal coordinate vectors $\mathbf{x} \in \mathbb{R}^n$, $\mathbf{y} \in \mathbb{R}^n$, and $\mathbf{z} \in \mathbb{R}^n$ are defined as

$$\mathbf{x} = \begin{Bmatrix} x_1 & \dots & x_n \end{Bmatrix}^{\mathrm{T}}, \tag{4.4a}$$

$$\mathbf{y} = \begin{Bmatrix} y_1 & \dots & y_n \end{Bmatrix}^{\mathrm{T}}, \tag{4.4b}$$

$$\mathbf{z} = \begin{Bmatrix} z_1 & \dots & z_n \end{Bmatrix}^{\mathrm{T}}, \tag{4.4c}$$

where (x_n, y_n, z_n) are the nodal coordinates of the n^{th} node. These are used to form the nodal coordinate matrix $[\mathbf{x}\ \mathbf{y}\ \mathbf{z}] \in \mathbb{R}^{n\times 3}$. Note here that all of the following formulations will be in terms of three-dimensional space but the same process can be applied to two dimensions, in which case, $d = 2$, where d is the number of dimensions, and $\mathbf{z} = \mathbf{0}$.

Notice in Fig. 6.2 that each node is assigned a number 1 through 6 and each member is assigned a number 1 through 12. This numbering scheme is convenient because many of the following presented vectors and matrices have b and/or n entries for each member and/or node, respectively corresponding to the labels in Fig. 6.2. For instance, the connectivity matrix $\mathbf{C} \in \mathbb{R}^{b\times n}$ has a column for each of the n nodes and a row for each of the b members, where b is the number of cable members plus the number of strut members. A given row vector of $\mathbf{C}$ will contain entries which dictate which nodes the member is connected to. Suppose member b connects nodes j and k ($j < k$), then the j^{th} and k^{th} elements of the b^{th} row of $\mathbf{C}$ are set to 1 and -1, respectively, as follows [55, 150]:

$$\mathbf{C}_{b,\gamma} = \begin{cases} 1 & \text{for} \quad \gamma = j\ , \\ \text{-1} & \text{for} \quad \gamma = k\ , \\ 0 & \text{otherwise}\ , \end{cases} \tag{4.5}$$

where b is the index for every row in $\mathbf{C}$ according to the member. Similarly, γ is the index for each column in $\mathbf{C}$. Note here that $\mathbf{C}$ is unitless. For examples of other ways to assemble

$\mathbf{C}$, refer to [62, 92]. Refer to Appendix A for the connectivity matrix used for the tensegrity prism presented in Fig. 6.2.

In the force density method, $\mathbf{C}$ has a special importance. Notice from the definition of $\mathbf{C}$ in Eq. (4.5), and $\mathbf{x}$ in Eq. (4.4a), that

$$\mathbf{Cx} = \begin{Bmatrix} x_2 \text{ - } x_1 \\ \vdots \\ x_n \text{ - } x_1 \end{Bmatrix} , \tag{4.6}$$

where B1 is connected to N1 and N2, and Bb is connected to Nn and N1. Eq. (4.6) is used to compact all of the coordinate differences from Eq. (4.1) into one vector. This is a system of coordinate differences referred to as the "projected lengths" of each member in the x-direction. Each member has three projected lengths, one in each of the x, y, and z directions. This is analogous to the $\hat{i}$, $\hat{j}$, and $\hat{k}$ components of a given member's length vector.

Thus, the system of equations is converted to matrix form by compacting the "equations" part of the system into a matrix times the unknown variables listed in a vector. The system of equilibrium equations can be expressed in two forms: Eq. (4.1) where q is factored out as the unknown, or Eq. (4.2) where the unknown variables are x, y, and z [119]. First, we examine the former, in which case Eq. (4.1) is equivalent to

$$\overbrace{\begin{bmatrix} -1 & \dots & 0 & \dots & -1 & \dots & 0 \\ \vdots & \ddots & \vdots & & \vdots & & \vdots \\ 1 & \dots & -1 & \dots & 1 & \dots & 0 \\ \vdots & & \vdots & \ddots & \vdots & & \vdots \\ 0 & \dots & 0 & \dots & 0 & \dots & -1 \\ \vdots & & \vdots & & \vdots & \ddots & \vdots \\ 0 & \dots & 1 & \dots & 0 & \dots & 1 \end{bmatrix}}^{\mathbf{A}} \begin{bmatrix} x_2 \text{ - } x_1 & \dots & 0 \\ \vdots & \ddots & \vdots \\ 0 & \dots & x_n \text{ - } x_1 \end{bmatrix} \overbrace{\begin{Bmatrix} q_{1,2} \\ q_{1,3} \\ \vdots \\ q_{1,n} \end{Bmatrix}}^{\mathbf{q}} = \overbrace{\begin{Bmatrix} f_{1,x} \\ f_{1,y} \\ f_{1,z} \end{Bmatrix}}^{\mathbf{f}} , \quad (4.7)$$

also written as

$$\begin{aligned} \mathbf{C}^{\mathrm{T}} \mathrm{diag}\left(\mathbf{C}\mathbf{x}\right) \mathbf{q} &= \mathbf{0} \ , \\ \mathbf{C}^{\mathrm{T}} \mathrm{diag}\left(\mathbf{C}\mathbf{y}\right) \mathbf{q} &= \mathbf{0} \ , \\ \mathbf{C}^{\mathrm{T}} \mathrm{diag}\left(\mathbf{C}\mathbf{z}\right) \mathbf{q} &= \mathbf{0} \ . \end{aligned} \quad (4.8)$$

This includes the x, y, and z directions and sets $\mathbf{f} = \mathbf{0}$, as tensegrity structures are self-equilibrated [74]. For this set of equations, the dependent variable is $\mathbf{q}$. The other form from Eq. (4.2) can be written as

$$\overbrace{\begin{bmatrix} \sum_{\gamma}^{p} q_{\gamma,\gamma+1} & \text{-}q_{1,2} & \dots & \text{-}q_{1,n} \\ \text{-}q_{1,2} & \sum_{\gamma}^{p} q_{\gamma,\gamma+1} & \vdots & 0 \\ \vdots & \dots & \ddots & \vdots \\ \text{-}q_{1,n} & 0 & \dots & \sum_{\gamma}^{p} q_{\gamma,\gamma+1} \end{bmatrix}}^{\mathbf{D}} \overbrace{\begin{bmatrix} \mathbf{x} & \mathbf{y} & \mathbf{z} \end{bmatrix}}^{} \begin{bmatrix} x_1 & y_1 & z_1 \\ x_2 & y_2 & z_2 \\ \vdots & \vdots & \vdots \\ x_n & y_n & z_n \end{bmatrix} = \overbrace{\begin{bmatrix} \mathbf{f}_x & \mathbf{f}_y & \mathbf{f}_z \end{bmatrix}}^{} \begin{bmatrix} f_{1,x} & f_{1,y} & f_{1,z} \\ f_{2,x} & f_{2,y} & f_{2,z} \\ \vdots & \vdots & \vdots \\ f_{\mathrm{p,x}} & f_{\mathrm{p,y}} & f_{\mathrm{p,z}} \end{bmatrix}, \quad (4.9)$$

or equivalently

$$\begin{aligned}
\mathbf{C}^{\mathrm{T}}\mathrm{diag}\left(\mathbf{q}\right)\mathbf{C}\mathbf{x} &= \mathbf{0}\ , \\
\mathbf{C}^{\mathrm{T}}\mathrm{diag}\left(\mathbf{q}\right)\mathbf{C}\mathbf{y} &= \mathbf{0}\ , \\
\mathbf{C}^{\mathrm{T}}\mathrm{diag}\left(\mathbf{q}\right)\mathbf{C}\mathbf{z} &= \mathbf{0}\ ,
\end{aligned} \tag{4.10}$$

in the x, y, and z directions and where $\mathbf{f} = \mathbf{0}$. Now the dependent variables are the nodal coordinates. The matrix $\mathbf{C}^{\mathrm{T}}\mathrm{diag}\left(\mathbf{q}\right)\mathbf{C}$ is known as a Gaussian transformation [128]. Eq. (4.9) relates back to Eq. (4.2) in that $\mathbf{D}$ has the form:

$$\mathbf{D}_{(j,k)} = \begin{cases} -q_\gamma & \text{if nodes } j \text{ and } k \text{ are connected}\ , \\ \sum_{\gamma}^{p} q_\gamma & \text{for } j = k\ , \\ 0 & \text{otherwise}\ . \end{cases} \tag{4.11}$$

4.2 Iterative equations

The two sets of equilibria equations for a general class k tensegrity structure are as follows [54]:

$$\mathbf{D}[\mathbf{x}\ \mathbf{y}\ \mathbf{z}] = [\mathbf{0}\ \mathbf{0}\ \mathbf{0}]\ , \tag{4.12a}$$

$$\mathbf{A}\mathbf{q} = \mathbf{0}\ , \tag{4.12b}$$

where the force density matrix $\mathbf{D}$, also referred to as the stress matrix [74], is a function of the member force density coefficient vector $\mathbf{q}$ while the equilibrium matrix $\mathbf{A}$ is a function of the nodal coordinate matrix $[\mathbf{x}\ \mathbf{y}\ \mathbf{z}]$ and $\mathbf{0}$ is the zero vector. No external forcing is assumed here. Note that Eqs. (4.12a) and (4.12b) have infinitely many solutions, implying that the system has an infinite number of equilibrium positions.

There are several strategies for solving Eqs. (4.12a) and (4.12b). For an overview of these, the reader is referred to Refs. [11, 71, 151]. Comparing Eq. (3.1) with Eqs. (4.12a) and (4.12b), it can be seen that $[\mathbf{x}\ \mathbf{y}\ \mathbf{z}]$ is in the null space of $\mathbf{D}$ and $\mathbf{q}$ is in the null space

of **A**. Note that because there are three vectors in [**x y z**], we must find three vectors that are in the null space of **D**. During the iterative process the algorithm changes the nodal coordinates and the force densities and passes them back and forth between Eqs. (4.12a) and (4.12b) until **x**, **y**, and **z** are in the nullspace of **D** and **q** is in the nullspace of **A**, i.e., a set of nodal coordinates and force densities that satisfy the equilibrium equations.

At each iteration, the best approximation for [**x y z**] in Eq. (4.12a) is selected from the decomposition of **D** and the best approximation for **q** in Eq. (4.12b) is selected from the decomposition of **A**. Beginning with either a guess for **q** or known coordinates [**x y z**] (see Fig. 4.2 for illustration), the form-finding procedure works by iterating between Eqs. (4.12a) and (4.12b) until **D** [**x y z**] and **Aq** are zero within a given tolerance *tol*, which in this case is 10^{-8}. For engineering purposes, the exact solution is not needed, but rather a solution with enough precision for practical implementation. Thus, zero is relaxed to *tol* and t is the total number of iterations completed at convergence.

Form-finding procedure

A left superscript of i is given to variables that change during the algorithm, denoting the variable's value at the i^{th} iteration. The following procedure was implemented in MATLAB version 2016a. Example form-found results can be found in Appendix A. The following form-finding algorithm uses a numerical iterative approach, where the only necessary input values are the structure's connectivity (stored in matrix **C**), b, n, d, and sgn (**t**), i.e., the direction of the internal axial force of each member (tension or compression). For the first iteration ($i = 0$), there are two possible choices as an input to the algorithm, depending on what is initially known about the structure. If an initial set of nodal coordinates that are close to a postulated equilibrium position, but not necessarily in equilibrium, are known, then the procedure begins with ^{0}[**x y z**] (see Fig. 4.2). Otherwise, the procedure starts with an initial guess for the force density, denoted ^{0}**q**, formed via Eq. (4.13).

The first iteration of **q** is

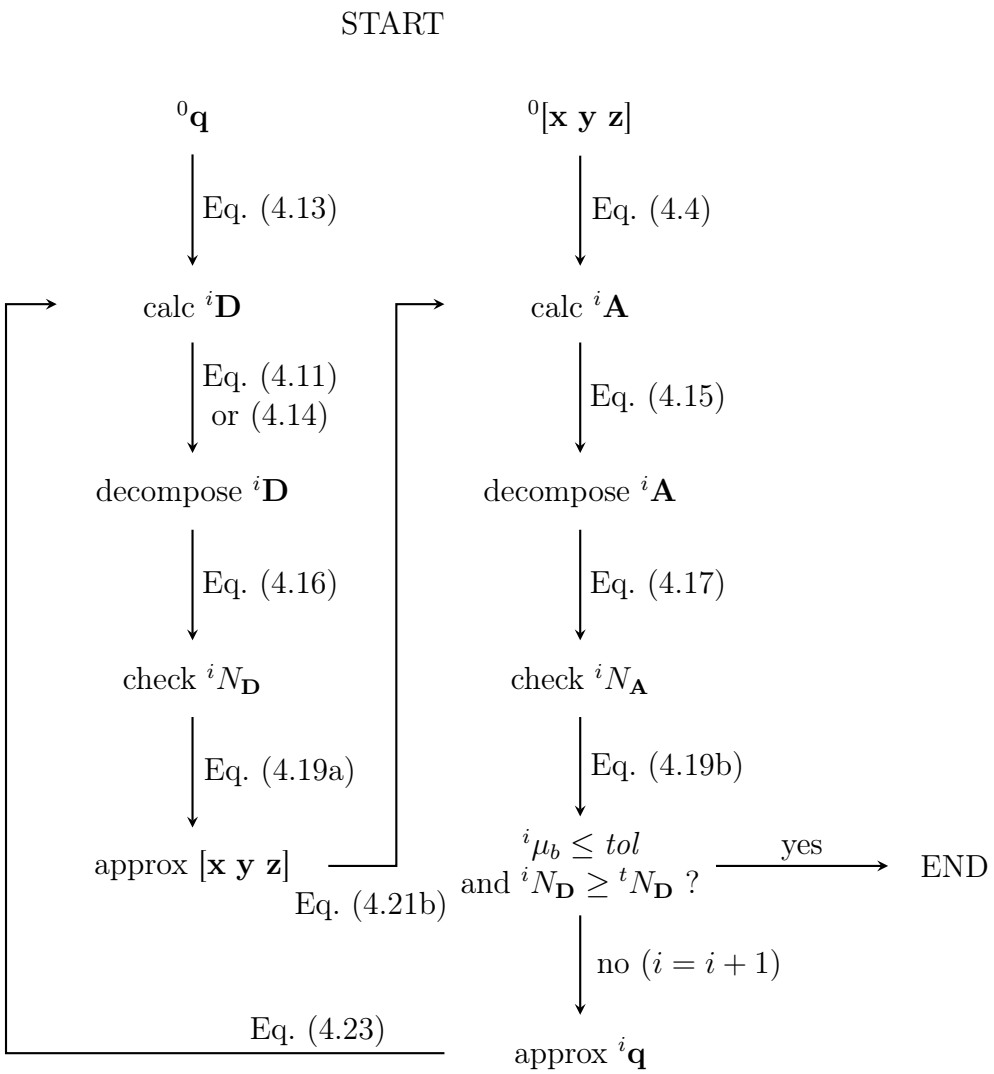

Figure 4.2: Form-finding algorithm flow diagram

$$
{}^0q = \begin{cases} 1 & \text{for tension members ,} \\ \\ \text{-1} & \text{for compression members ,} \end{cases} \tag{4.13}
$$

where ${}^0q$ is an entry in the vector ${}^0\mathbf{q}$. The sign convention here is important and the sign of each entry in ${}^i\mathbf{q}$ will stay the same, i.e., throughout the algorithm $\mathbf{q}$ does not change direction, only magnitude. This is due to the fact that cables are assumed not to support compression. This is not the only way to generate ${}^0\mathbf{q}$, as Koohestani and Guest [56] generates this vector randomly. Refer to Refs. [56, 152] for other variations of ${}^0\mathbf{q}$.

As long as the initial coordinates are unknown, the calculation of $\mathbf{D}$ will be the first step at the beginning of each iteration. The i^{th} iteration of $\mathbf{D} \in \mathbb{R}^{b\times b}$ is

$$
{}^i\mathbf{D} = \mathbf{C}^{\mathrm{T}} \operatorname{diag}({}^i\mathbf{q})\ \mathbf{C} \ . \tag{4.14}
$$

Note that $\mathbf{D}$ can also be calculated via Eq. (4.11).

If an initial set of nodal coordinates are known, the first operation performed in the algorithm will compute $\mathbf{A}$ using ${}^0[\mathbf{x}\ \mathbf{y}\ \mathbf{z}]$. The i^{th} iteration of $\mathbf{A} \in \mathbb{R}^{3n\times b}$ is built by stacking three $n \times b$ matrices on top of each other, as in

$$
{}^i\mathbf{A} = \begin{bmatrix} \mathbf{C}^{\mathrm{T}} \operatorname{diag}(\mathbf{C}\ {}^i\mathbf{x}) \\ \mathbf{C}^{\mathrm{T}} \operatorname{diag}(\mathbf{C}\ {}^i\mathbf{y}) \\ \mathbf{C}^{\mathrm{T}} \operatorname{diag}(\mathbf{C}\ {}^i\mathbf{z}) \end{bmatrix} \ . \tag{4.15}
$$

The equilibrium matrix of a structure contains a wealth of the static/kinematic properties [2, 11, 153]. The set of states of self-stress is contained within the null space of the equilibrium matrix, which is needed in the design of optimal states of pre-stress to tension all cables in a tensegrity [153]. The bases of vector spaces of force densities and internal mechanisms can be calculated from the null space of the equilibrium matrix $\mathbf{A}$ [51, 91]. Because $\mathbf{D}$ is always square, symmetric, and singular, $[\mathbf{x}\ \mathbf{y}\ \mathbf{z}]$ in Eq. (4.12a) can be found through

the EVD [42]. However, $\mathbf{q}$ in Eq. (4.12b) must be found through the SVD [42].

The EVD of ${}^{i}\mathbf{D}$ is

$$ {}^{i}\mathbf{D} = {}^{i}\mathbf{\Phi}^{\mathrm{T}} \operatorname{diag}({}^{i}\boldsymbol{\lambda})\, {}^{i}\mathbf{\Phi} \ , \tag{4.16} $$

where ${}^{i}\boldsymbol{\lambda} \in \mathbb{R}^{b}$ is a vector of the eigenvalues sorted in ascending order and ${}^{i}\mathbf{\Phi} \in \mathbb{R}^{b\times b}$ is the eigenvector matrix which has an eigenvector ${}^{i}\boldsymbol{\phi} \in \mathbb{R}^{b}$ as each column.

The SVD of ${}^{i}\mathbf{A}$ is [154]

$$ {}^{i}\mathbf{A} = {}^{i}\mathbf{U}^{\mathrm{T}} \operatorname{diag}({}^{i}\boldsymbol{\mu})\, {}^{i}\mathbf{W} \ , \tag{4.17} $$

where ${}^{i}\boldsymbol{\mu} \in \mathbb{R}^{b}$ is a vector of the singular values sorted in descending order, ${}^{i}\mathbf{U} \in \mathbb{R}^{n\times n}$ is a matrix with each left singular vector ${}^{i}\mathbf{u} \in \mathbb{R}^{n}$ as the columns, and ${}^{i}\mathbf{W} \in \mathbb{R}^{b\times b}$ is a matrix with each right singular vector ${}^{i}\mathbf{w} \in \mathbb{R}^{b}$ as the columns. It is well-known that the column vectors $\mathbf{u}$ contain the inextensional mechanisms, which are either infinitesimal mechanisms or rigid body motions [51]. Note that the matrix $\operatorname{diag}({}^{i}\boldsymbol{\mu})$ that comes out of the SVD will have b - n extra zero rows due to the fact that this matrix is rectangular. Although it is generally desired that the sign of $\mathbf{q}$ be the same in all iterations, the overall sign is not important at this stage, and is arbitrary in the SVD [56]. Also note, in the following sections, it is assumed that the eigenvalue-vector and singular value-vector pairs have already been rearranged such that the eigenvalues are sorted in ascending order and singular values sorted in descending order, respectively.

From here, to find the best approximated solution to Eq. (4.12a), ${}^{i}\mathbf{D}$ can be decomposed via Eq. (4.16). Three of the eigenvectors are selected as the nodal coordinates $[\mathbf{x}\ \mathbf{y}\ \mathbf{z}]$ used to calculate ${}^{i}\mathbf{A}$. Similarly, ${}^{i}\mathbf{A}$ is decomposed according to Eq. (4.17) and the best singular vector that approximates Eq. (4.12b) is selected as $\mathbf{q}$. From here, if the last singular value ${}^{i}\mu_{b}$ (Eq. (4.17)) is greater than *tol*, then $i = i+1$, and $\mathbf{D}$ is recalculated with ${}^{i+1}\mathbf{q}$ via Eq. (4.11)

or (4.14), and the process described above is repeated for i iterations. Fig. 4.2 shows an illustrative flow chart of the full iterative process [13, 42, 51, 54].

Condition(s) for convergence

The algorithmic iterations are concerned with the zero eigenvalues of $\mathbf{D}$ and the zero singular values of $\mathbf{A}$, for achieving convergence. Throughout the iteration process, there are tactics to "force" a matrix to become rank deficient to create a null space. To find a $\mathbf{q}$ which satisfies Eq. (4.12b), the dimension of the null space of $\mathbf{A}$ must be at least one. Similarly, to find nodal coordinates $[\mathbf{x}\ \mathbf{y}\ \mathbf{z}]$ which solve Eq. (4.12a), the null space of $\mathbf{D}$ must be at least three for three vectors (one for $\mathbf{x}$, one for $\mathbf{y}$, and one for $\mathbf{z}$) to be the solution.

There are two rank deficiencies (or null spaces) of importance for this algorithm: the current iteration dimension of the null space ${}^{i}N$ and the target dimension of the null space ${}^{t}N$. After every iteration, the algorithm checks the current null spaces of ${}^{i}\mathbf{D}$ and ${}^{i}\mathbf{A}$. If at the end of an iteration either ${}^{i}N_{\mathbf{D}} \neq {}^{t}N_{\mathbf{D}}$ or ${}^{i}N_{\mathbf{A}} \neq {}^{t}N_{\mathbf{A}}$, the algorithm continues to the next iteration ($i = i + 1$). The algorithm strategically chooses ${}^{i}[\mathbf{x}\ \mathbf{y}\ \mathbf{z}]$ from the eigenvectors and ${}^{i}\mathbf{q}$ from the right singular vectors so that ${}^{i}N$ approaches ${}^{t}N$.

The dimensions of the null spaces of $\mathbf{D}$ and $\mathbf{A}$ for the i^{th} iteration are computed as follows:

$$ {}^{i}N_{\mathbf{D}} = b \text{ - rank}\,({}^{i}\mathbf{D}) \ , \tag{4.18a} $$

$$ {}^{i}N_{\mathbf{A}} = 3n \text{ - rank}\,({}^{i}\mathbf{A}) \ , \tag{4.18b} $$

where rank $({}^{i}\mathbf{D})$ is the number rows in ${}^{i}\mathbf{D}$ that are linearly independent [149] and rank $({}^{i}\mathbf{A})$ is the number of linearly independent rows in ${}^{i}\mathbf{A}$. Eq. (4.18a) and Eq. (4.18b) come from the fact that, by definition, the rank of a matrix plus the dimension of the null space of the same matrix is equal to the number of rows in that matrix.

Notice $\mathbf{1}$ is in the null space of $\mathbf{D}$, i.e., ${}^{i}N_{\mathbf{D}}$ must be at least one. Note that this is where

the '+1' came from in Eq. (4.19a). The **1** vector is an eigenvector of **D**. However, **x**, **y**, nor **z** can be the **1** vector. Imagine $\mathbf{z} = \mathbf{1}$, so every node has the same z-coordinate. In this case, all nodes will lie along the x-y plane, which means the structure has collapsed down to two-dimensions. It will be seen that this **1** vector is intentionally discarded so that it is not a candidate for x, y, or z.

The target null spaces of **D** and **A** are

$$^{t}N_{\mathbf{D}} = d + 1 \tag{4.19a}$$

and

$$^{t}N_{\mathbf{A}} \geq 1 \ , \tag{4.19b}$$

respectively. In other words, when $^{i}N_{\mathbf{D}}$ from Eq. (4.18a) is equal to $d + 1$ and $^{i}N_{\mathbf{A}}$ from Eq. (4.18b) is at least equal to one, this means Eqs. (4.12a) and (4.12b) are satisfied, so the algorithm has converged. Another way of looking at the same set of criteria would be to iterate until **D** has $d + 1$ zero eigenvalues and **A** has at least one zero singular value. Note here that when $\mu_b \leq \ tol$, Eq. (4.19b) is automatically satisfied. Also, note that regardless of the $^{i}N_{\mathbf{A}}$ value calculated in Eq. (4.18b), **D**'s null space $N_{\mathbf{D}}$ must be large enough to terminate the algorithm.

Approximating ^{i}[x y z]

There are many methods for choosing ^{i}[**x y z**] [42, 54, 152]. The method used by Estrada, et al. [42] is the one that is used in this work.

In Eq. (4.16), the eigenvector corresponding to the zero eigenvalue is a null space vector and in Eq. (4.17), the right singular vector corresponding to the zero singular value is also a null space vector. This shows that the three $\boldsymbol{\phi}$ that correspond to the three zero λ are the nodal coordinates ^{i}[**x y z**] that solve Eq. (4.12a) and the **w** that corresponds to the zero $\boldsymbol{\mu}$ is the **q** that solves Eq. (4.12b). For this reason, the algorithm strategically chooses ^{i}[**x y**

$\mathbf{z}]$ and ${}^{i}\mathbf{q}$ at each iteration so that the corresponding eigen- and singular values iteratively approach *tol*. When it is necessary to approximate the solution for the next iteration, certain eigenvectors from ${}^{i}\mathbf{\Phi}$ (Eq. (4.16)) and certain singular vectors from ${}^{i}\mathbf{W}$ from Eq. (4.17) are used for finding the next ${}^{i}[\mathbf{x}\ \mathbf{y}\ \mathbf{z}]$ and ${}^{i}\mathbf{q}$, respectively. The selection of $\boldsymbol{\phi}$ and $\mathbf{w}$ depends on the dimension of ${}^{i}N$.

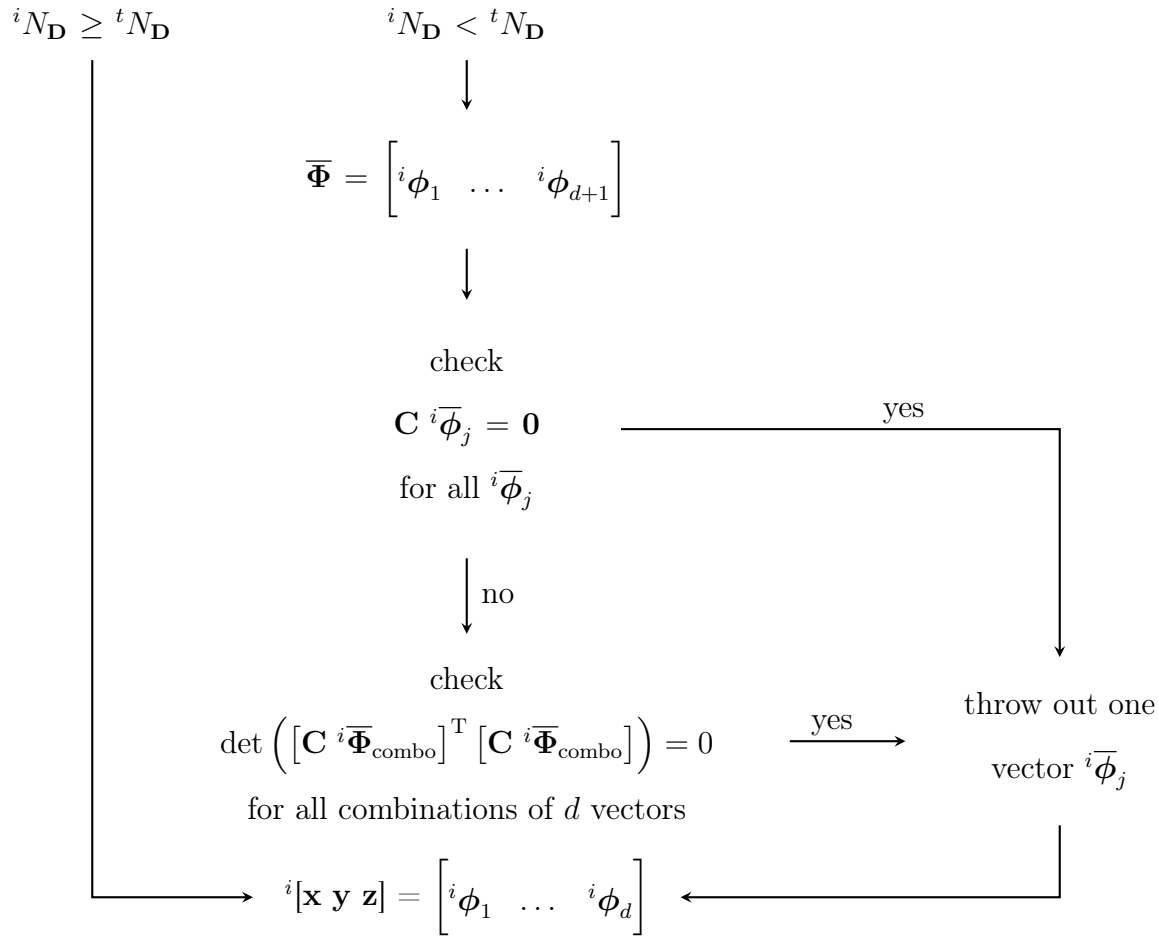

Figure 4.3: Approximating ${}^{i}[\mathbf{x}\ \mathbf{y}\ \mathbf{z}]$

Ultimately, we want ${}^{i}\mathbf{x}, {}^{i}\mathbf{y}$, and ${}^{i}\mathbf{z}$ to be linearly independent without any equaling $\mathbf{1}$ (or having entries all with the same value). So, define $\overline{\mathbf{\Phi}}$ as

$$ {}^{i}\overline{\mathbf{\Phi}} = \left[{}^{i}\boldsymbol{\phi}_1 \quad \dots \quad {}^{i}\boldsymbol{\phi}_{d+1} \right] . \tag{4.20} $$

When ${}^{i}N_D$ (Eq. (4.18a)) $\geq {}^{t}N_D$ (Eq. (4.19a)), the ${}^{i}\boldsymbol{\phi}$ (Eq. (4.16)) corresponding to the

smallest d λ are in the null space of ${}^{i}\mathbf{D}$ and these d columns $\begin{bmatrix} {}^{i}\boldsymbol{\phi}_1 & \dots & {}^{i}\boldsymbol{\phi}_d \end{bmatrix}$ are ${}^{i}[\mathbf{x}\ \mathbf{y}\ \mathbf{z}]$ because they satisfy Eq. (4.12a). Note that this means, even when the null space is larger than required, only d vectors are pulled from $\boldsymbol{\Phi}$.

When ${}^{i}N_D < {}^{t}N_D$, $d+1$ columns of ${}^{i}\overline{\boldsymbol{\Phi}}$ (Eq. (4.20)) are used to approximate ${}^{i}[\mathbf{x}\ \mathbf{y}\ \mathbf{z}]$. This is accomplished by forming ${}^{i}\overline{\boldsymbol{\Phi}}_{\text{combo}}$, a matrix of any set of d vectors from ${}^{i}\overline{\boldsymbol{\Phi}}$. The process assesses the column vectors of ${}^{i}\overline{\boldsymbol{\Phi}}$ and throws out one of them for either being the $\mathbf{1}$ vector or for linear dependency:

$$\mathbf{C}\ {}^{i}\overline{\boldsymbol{\phi}}_j \begin{cases} = \mathbf{0} & \text{if } {}^{i}\overline{\boldsymbol{\phi}}_j = \mathbf{1}\ , \\ \neq \mathbf{0} & \text{if } {}^{i}\overline{\boldsymbol{\phi}}_j \neq \mathbf{1}\ , \end{cases} \tag{4.21a}$$

and

$$\det\left(\left[\mathbf{C}\ {}^{i}\overline{\boldsymbol{\Phi}}_{\text{combo}}\right]^{\mathrm{T}}\left[\mathbf{C}\ {}^{i}\overline{\boldsymbol{\Phi}}_{\text{combo}}\right]\right) \begin{cases} = 0 & \text{if } {}^{i}\overline{\boldsymbol{\Phi}}_{\text{combo}} \text{ are linearly dependent}\ , \\ \neq 0 & \text{if } {}^{i}\overline{\boldsymbol{\Phi}}_{\text{combo}} \text{ are linearly independent}\ . \end{cases} \tag{4.21b}$$

Eq. (4.21a) is always checked first, where $\mathbf{C}$ is multiplied by each eigenvector 1 through $d+1$ to check if any result in $\mathbf{0}$. If an eigenvector is not first eliminated by Eq. (4.21a), then the linear dependency of each set of d eigenvectors can be checked by Eq. (4.21b). In this way, every combination of d vectors from ${}^{i}\overline{\boldsymbol{\Phi}}$ is checked until a linearly independent set is found. Then, the set of d eigenvectors which results in a nonzero determinant, computed by Eq. (4.21b), will be ${}^{i}[\mathbf{x}\ \mathbf{y}\ \mathbf{z}]$.

Approximating ${}^{i}\mathbf{q}$

There are several methods for approximating ${}^{i}\mathbf{q}$ [54, 74].

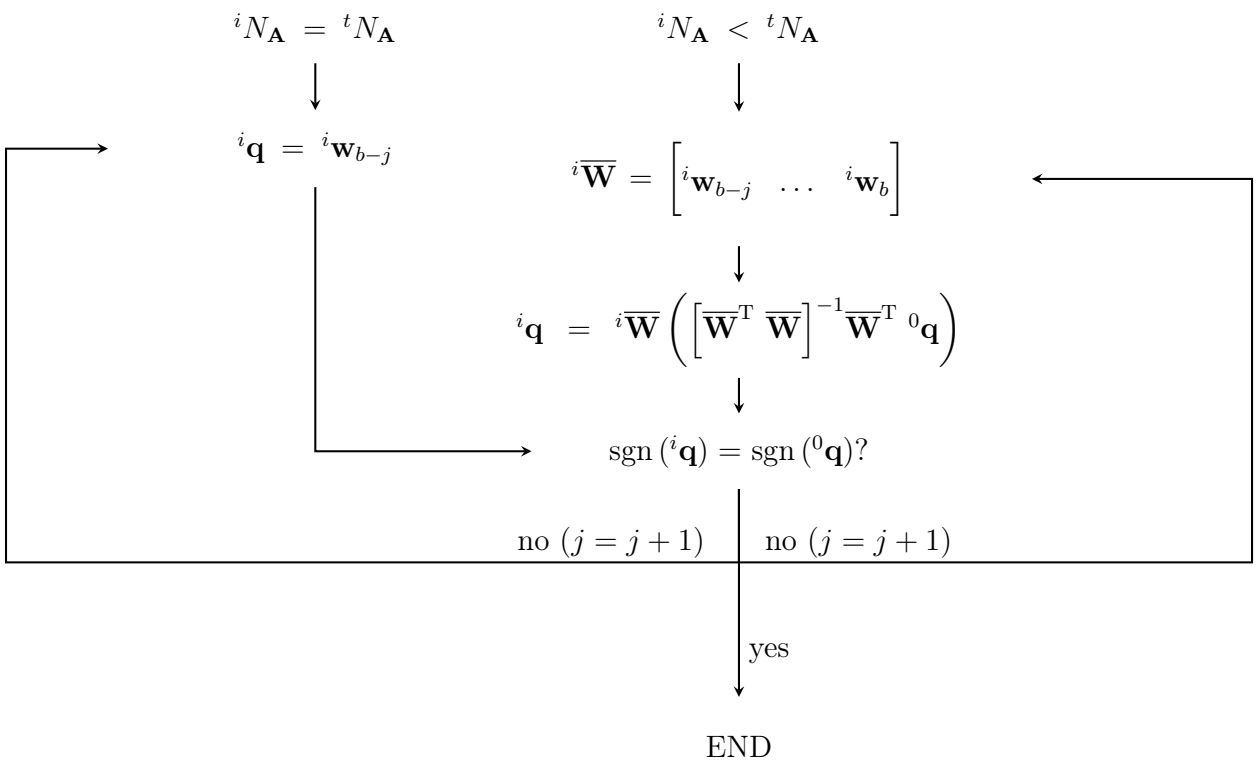

Figure 4.4: Approximating ${}^{i}\mathbf{q}$ for ${}^{i}N_{\mathbf{A}} = {}^{t}N_{\mathbf{A}}$ and ${}^{i}N_{\mathbf{A}} < {}^{t}N_{\mathbf{A}}$

Ultimately it is desired that the entries of ${}^{i}\mathbf{q}$ be negative for struts and positive for cables, i.e., when

$$\mathrm{sgn}({}^{i}\mathbf{q}) = \mathrm{sgn}\left({}^{0}\mathbf{q}\right) \ , \tag{4.22}$$

${}^{i}\mathbf{q}$ has been found. When ${}^{i}N_{A} = {}^{t}N_{A} = 1$, the ${}^{i}\mathbf{w}$ corresponding to the zero μ is in the null space of ${}^{i}\mathbf{A}$. Note here that this column may have inverted signs and this should be checked. This column definitely satisfies Eq. (4.12b); however, it must also satisfy Eq. (4.22) to be ${}^{i}\mathbf{q}$. If Eq. (4.22) is not satisfied, the second to last column of ${}^{i}\overline{\mathbf{W}}$ is checked and so on, until each sign matches its member type.

When ${}^{i}N_{A} < {}^{t}N_{A}$, one or more ${}^{i}\mathbf{w}$ vectors are used for approximating ${}^{i}\mathbf{q}$. The procedure employs the columns of $\mathbf{W}$ to find a least squares approximation to minimize the 2-norm [42]:

$$\left|\left|{}^{i}\mathbf{W}\ {}^{i}\mathbf{q}\ \text{-}\ {}^{0}\mathbf{q}\right|\right|^{2}\ . \tag{4.23}$$

The procedure starts by first defining $\overline{\mathbf{W}}$, a modified version of $\mathbf{W}$ from Eq. (4.17):

$${}^{i}\overline{\mathbf{W}} = \begin{bmatrix} {}^{i}\mathbf{w}_{b-j} & \dots & {}^{i}\mathbf{w}_{b} \end{bmatrix}\ , \tag{4.24}$$

where the dimensions of $\overline{\mathbf{W}}$ change depending on the value of j. Note when $j = 0$, $\overline{\mathbf{W}}$ is a vector. The procedure starts with ${}^{i}\overline{\mathbf{W}}$ and it is used to compute ${}^{i}\mathbf{q}$. If this $\mathbf{q}$ does not satisfy Eq. (4.22), then the next ${}^{i}\mathbf{w}$ is added to the beginning of $\overline{\mathbf{W}}$. The process is repeated, by adding singular vectors to $\overline{\mathbf{W}}$ until ${}^{i}\mathbf{q}$ is found.

To find ${}^{i}\mathbf{q}$, $\overline{\mathbf{W}}$ is used as a basis for the solution space and this process searches for the coefficients $\mathbf{c}$ that give the linear combination of ${}^{i}\mathbf{q}$, i.e.,

$$\overbrace{{}^{i}\overline{\mathbf{W}}\mathbf{c}}^{{}^{i}\mathbf{q}} = {}^{0}\mathbf{q}. \tag{4.25}$$

Multiplying Eq. (4.25) by the transpose of $\overline{\mathbf{W}}$ because $\left[\overline{\mathbf{W}}^{\mathrm{T}}\ \overline{\mathbf{W}}\right]$ is invertible and inverting this matrix to the right-hand side gives

$$\mathbf{c} = \left[\overline{\mathbf{W}}^{\mathrm{T}}\ \overline{\mathbf{W}}\right]^{-1}\overline{\mathbf{W}}^{\mathrm{T}}\ {}^{0}\mathbf{q}\ . \tag{4.26}$$

This will give the coefficients $\mathbf{c}$ that are the least squared approximation of ${}^{i}\mathbf{q}$:

$${}^{i}\mathbf{q} = \overline{\mathbf{W}}\mathbf{c}\ . \tag{4.27}$$

When ${}^{i}N_{A} > {}^{t}N_{A}$, there is more than one zero singular value. This means that there is more than one ${}^{i}\mathbf{w}$ in the null space of ${}^{i}\mathbf{A}$ that solves Eq. (4.12b), and so a combination of them will give the approximated ${}^{i}\mathbf{q}$. The calculation of $\mathbf{q}$ is relatively straightforward when $s = 1$; however, this is not the case for tensegrities with multiple self-stress states [74]. There is a special case, such as with tensegrity masts or cable domes [105], of the form-finding

algorithm in which ${}^{i}N_{\mathbf{A}}$ is larger than 1. In this case, the system is said to have multiple states of self-stress and requires extra steps when approximating ${}^{i}\mathbf{q}$ in Eq. (4.23) [2,51,155].

The situation is important to explore because tensegrity prism masts have more than one state of self-stress. Previously, the form-finding algorithm could begin with either a guess at ${}^{0}\mathbf{q}$ or with an initial set of nodal coordinates ${}^{0}[\mathbf{x}\ \mathbf{y}\ \mathbf{z}]$. However, tensegrity masts require the specification of an initial set of nodal coordinates to form-find successfully.

Multiple self-stress states has been addressed in other ways. For example, Yuan, et al. [106] use the Double Singular Value Decomposition (DSVD) Method to determine the integral pre-stress distribution of a cable dome. During the procedure, the SVD is applied twice, once on the equilibrium matrix to obtain the independent self-stress modes and a second time on a matrix of independent self-stress modes to obtain the integral pre-stress modes. A similar process is performed here, where the members are grouped based on symmetry to find what is known as the single integral self-stress state [37,51].

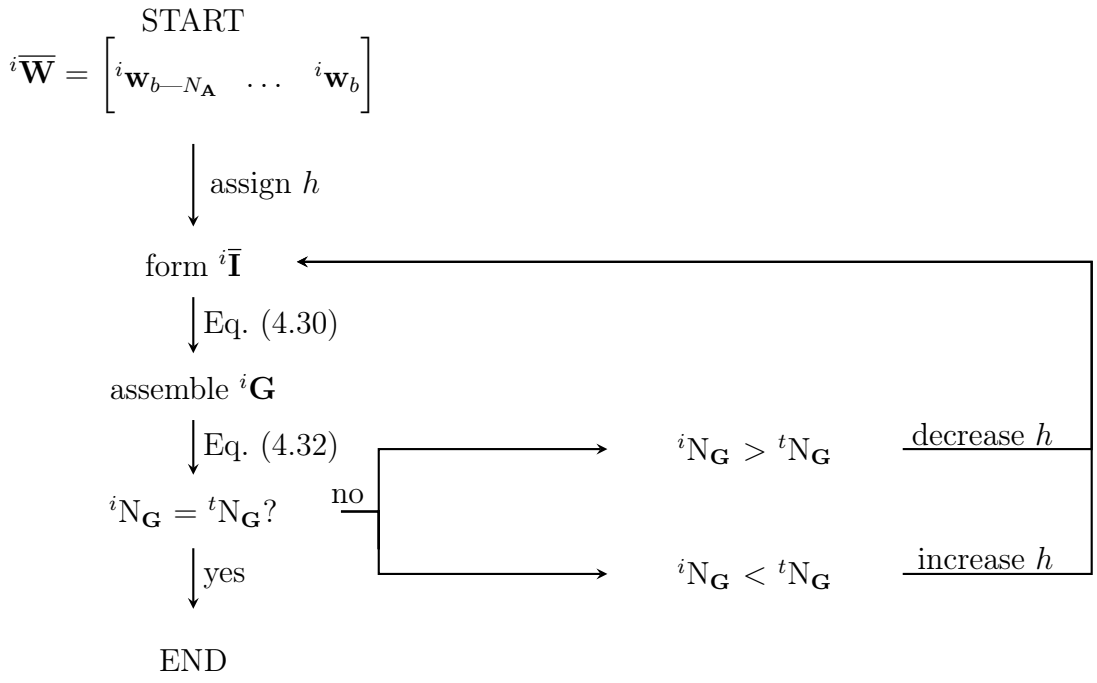

Figure 4.5: Approximating ${}^{i}\mathbf{q}$ for ${}^{i}N_{\mathbf{A}} > {}^{t}N_{\mathbf{A}}$

When ${}^{i}N_A = {}^{t}N_A$, $\mathbf{q}$ was the last column of $\mathbf{W}$ because there was only one vector in the null space of $\mathbf{A}$. Now the null space is larger than one and hence multiple null space vectors are used for determining $\mathbf{q}$.

When ${}^{i}N_{\mathbf{A}} > 1$, ${}^{i}\overline{\mathbf{W}}$ is

$$ {}^{i}\overline{\mathbf{W}} = \begin{bmatrix} {}^{i}\mathbf{w}_{b-N_{\mathbf{A}}} & \dots & {}^{i}\mathbf{w}_{b} \end{bmatrix} , \tag{4.28} $$

where ${}^{i}\overline{\mathbf{W}}$ is a matrix of $N_{\mathbf{A}}$ singular vectors that are the last $N_{\mathbf{A}}$ columns of ${}^{i}\mathbf{W}$ from Eq. (4.17). Note that $\overline{\mathbf{W}}$ will always be a matrix. The feasible self-stress mode ${}^{i}\mathbf{q}$ can be calculated as a linear combination of $N_{\mathbf{A}}$ independent self-stress modes [19], where $N_{\mathbf{A}}$ is the number of vectors in the null space of $\mathbf{A}$.

$$ \mathbf{I}_{(b\times b)}\,{}^{i}\mathbf{q} = {}^{i}\overline{\mathbf{W}} \overbrace{\begin{Bmatrix} \mathrm{c}_1 \\ \vdots \\ \mathrm{c}_{N_{\mathbf{A}}} \end{Bmatrix}}^{\mathbf{c}} \tag{4.29} $$

is solved for ${}^{i}\mathbf{q}$, where ${}^{i}\overline{\mathbf{W}}$ is used as the basis vectors for the self-stress modes [91]. This process is performed because the $\mathbf{w}$ vectors in the null space of the equilibrium matrix $\mathbf{A}$ cannot be employed directly because they do not satisfy Eq. (4.22). The unknown ${}^{i}\mathbf{q}$ in Eq. (4.27) can be reduced to ${}^{i}\overline{\mathbf{q}}$ if the system is symmetric, which leads to a reduction in unknowns. When there exists members that have the same q value, this will form a group. Then, the grouped ${}^{i}\mathbf{q}$ is ${}^{i}\overline{\mathbf{q}} \in \mathbb{R}^{h}$, where h is the number of groups. Then, $\mathbf{I} \in \mathbb{R}^{b\times b}$ is reduced from its definition in Eq. (4.29) to $\overline{\mathbf{I}} \in \mathbb{R}^{h\times h}$, a shortened identity matrix, which distributes the correct $\overline{q}$ value to each member in its group:

$$ {}^{i}\overline{\mathbf{I}} = \begin{cases} 1 & \text{member } b \text{ belongs to group } h \ , \\ 0 & \text{otherwise} \ , \end{cases} \tag{4.30} $$

such that Eq. (4.29) becomes

$$ {}^{i}\overline{\mathbf{W}}\mathbf{c} \text{ - } {}^{i}\overline{\mathbf{I}} \overbrace{\begin{Bmatrix} \overline{q}_1 \\ \vdots \\ \overline{q}_h \end{Bmatrix}}^{\overline{\mathbf{q}}} = \mathbf{0} \ . \tag{4.31} $$

Now adding ${}^{i}\overline{\mathbf{q}}$ to the end of $\mathbf{c}$ creates a new vector $\boldsymbol{s}$ and similarly, adding ${}^{i}\overline{\mathbf{I}}$ to the right end of ${}^{i}\overline{\mathbf{W}}$, Eq. (4.31) then becomes [150]

$$ \overbrace{\begin{bmatrix} {}^{i}\overline{\mathbf{W}} & \text{-} {}^{i}\overline{\mathbf{I}} \end{bmatrix}}^{{}^{i}\mathbf{G}} \overbrace{\begin{Bmatrix} \mathbf{c} \\ {}^{i}\overline{\mathbf{q}} \end{Bmatrix}}^{{}^{i}\boldsymbol{s}} = \mathbf{0} \ . \tag{4.32} $$

Recall that the vector $\boldsymbol{s}$ which satisfies Eq. (4.32) is in the null space of matrix $\mathbf{G}$. So, the null space of $\mathbf{G}$ should be exactly one by the end of this sub-iterative process [51]:

$$ {}^{t}N_{\mathbf{G}} = 1. \tag{4.33a} $$

From Eq. (4.32), it can be seen that $\mathbf{G} \in \mathbb{R}^{b\times({}^{t}N_{\mathbf{A}}+h)}$, so the null space of ${}^{i}\mathbf{G}$ is calculated by

$$ {}^{i}N_{\mathbf{G}} = ({}^{t}N_{\mathbf{A}} + h) \text{ - } \operatorname{rank}\left({}^{i}\mathbf{G}\right), \tag{4.33b} $$

where $N_{\mathbf{G}}$ is the dimension of the null space of $\mathbf{G}$, and $\operatorname{rank}(\mathbf{G})$ is the rank of $\mathbf{G}$ [95]. From here, if ${}^{i}N_{\mathbf{G}} = {}^{t}N_{\mathbf{G}}$, then the vector $\boldsymbol{s}$ satisfying Eq. (4.32) can be found. Thus, SVD is employed again here:

$$ {}^{i}\mathbf{G} = {}^{i}\boldsymbol{\Upsilon}^{\mathrm{T}}\operatorname{diag}\left({}^{i}\boldsymbol{\nu}\right){}^{i}\boldsymbol{\Pi}. \tag{4.34} $$

However, if ${}^{i}N_{\mathbf{G}} < {}^{t}N_{\mathbf{G}}$, the number of groups (h) are increased because there are not enough equations for the amount of unknowns. Finally, if ${}^{i}N_{\mathbf{G}} > {}^{t}N_{\mathbf{G}}$, there are multiple

pre-stressed modes satisfying the symmetry condition and h is decreased. From here, the process is repeated and at each iteration the number of groups is either increased or decreased depending on the value of ${}^{i}N_{\mathbf{G}}$ (Eq. (4.33b)). The new vector for $\overline{\mathbf{q}}$ is established, $\mathbf{G}$ is reassembled with the new $\bar{\mathbf{I}}$, and then Eqs. (4.33a) and (4.33b) are used again to determine if/how h needs to be changed [105]. When ${}^{i}N_{\mathbf{G}} = {}^{t}N_{\mathbf{G}}$, the last column of $\mathbf{\Pi}$, $\boldsymbol{\pi}_{(N_{\mathbf{A}}+h)}$, is taken to be the $\mathbf{s}$ vector that satisfies Eq. (4.32).

4.3 Static analysis

Stiffness matrix derivation

A vector of member stiffnesses $\boldsymbol{\kappa} \in \mathbb{R}^b$ can be calculated by

$$\boldsymbol{\kappa} = \frac{\mathbf{ea}}{\boldsymbol{\ell}_0} \,, \tag{4.35}$$

where $\mathbf{e} \in \mathbb{R}^b$, $\mathbf{a} \in \mathbb{R}^b$, and $\boldsymbol{\ell}_0 \in \mathbb{R}^b$ are the Young's modulus, cross-sectional area, and unstressed length vectors, respectively.

The tangent stiffness matrix can be described as a collection of the first-order partial derivatives of a function with respect to each component of the function, linearized around some point x_0:

$$\mathbf{K} = \left.\frac{\partial \mathbf{f}}{\partial \mathbf{x}}\right|_{x_0} \,. \tag{4.36}$$

For each configuration, the nodal coordinates of a tensegrity structure are correlated with the external forces through the equilibrium condition(s). One can then consider the external force vector as a function of the nodal coordinate vector, that is $\mathbf{f} = \mathbf{f}(\mathbf{p})$. In differential form [156]:

$$\overbrace{\frac{\mathrm{d}\mathbf{f}}{\mathrm{d}\mathbf{p}}}^{\mathbf{K}} \cdot \mathrm{d}\mathbf{p} = \mathrm{d}\mathbf{f}. \tag{4.37}$$

It is also known that $\mathbf{f} = \mathbf{f}\left(\mathbf{p}, \mathbf{t}\left(\mathbf{p}\right), \boldsymbol{\ell}^{-1}\left(\mathbf{p}\right)\right)$. Therefore, $\mathbf{K}$ can be expanded by chain rule as [156]

$$\mathbf{K} = \frac{\partial \mathbf{f}}{\partial \mathbf{p}} + \frac{\partial \mathbf{f}}{\partial \mathbf{t}} \cdot \frac{\partial \mathbf{t}}{\partial \boldsymbol{\ell}} \cdot \frac{\partial \boldsymbol{\ell}}{\partial \mathbf{p}} + \frac{\partial \mathbf{f}}{\partial \boldsymbol{\ell}^{-1}} \cdot \frac{\partial \boldsymbol{\ell}^{-1}}{\partial \boldsymbol{\ell}} \cdot \frac{\partial \boldsymbol{\ell}}{\partial \mathbf{p}} \ , \tag{4.38}$$

where

$$\frac{\partial \mathbf{f}}{\partial \mathbf{p}} = \mathbf{S} \ , \tag{4.39}$$

$$\frac{\partial \mathbf{f}}{\partial \mathbf{t}} = \mathbf{A} \ , \tag{4.40}$$

$$\frac{\partial \mathbf{t}}{\partial \boldsymbol{\ell}} \cdot \frac{\partial \boldsymbol{\ell}}{\partial \mathbf{p}} = \mathrm{diag}\left(\boldsymbol{\kappa}\right) \cdot \mathbf{A}^{\mathrm{T}} \ , \tag{4.41}$$

$$\frac{\partial \mathbf{f}}{\partial \boldsymbol{\ell}^{-1}} = \mathbf{A} \cdot \mathrm{diag}\left(\mathbf{t}\right) \ , \tag{4.42}$$

and

$$\frac{\partial \boldsymbol{\ell}^{-1}}{\partial \boldsymbol{\ell}} \cdot \frac{\partial \boldsymbol{\ell}}{\partial \mathbf{p}} = \text{-}\mathrm{diag}\left(\boldsymbol{\ell}^{-1}\right) \cdot \mathbf{A}^{\mathrm{T}} \ . \tag{4.43}$$

Using Eqs. (4.39)–(4.43), Eq. (4.38) becomes

$$\mathbf{K} = \overbrace{\mathbf{I}_{(d\times d)} \otimes \mathbf{D}}^{\mathbf{K}_{\mathrm{G}}} + \overbrace{\mathbf{A} \cdot \mathrm{diag}\left(\boldsymbol{\kappa}\right) \cdot \mathbf{A}^{\mathrm{T}}}^{\mathbf{K}_{\mathrm{E}}} \text{ - } \mathbf{A} \cdot \mathrm{diag}\left(\mathbf{q}\right) \cdot \mathbf{A}^{\mathrm{T}} \ . \tag{4.44}$$

Here all structural elements have been considered to be nonlinear because everything is dependent on $\boldsymbol{\ell}$. Generally, existing methods assemble the structural stiffness from element stiffnesses and assume all members to be linear elastic, in which case the structural stiffness matrix reduces to Eq. (4.47) [156]. This means, if a structure is kinematically indeterminate, its stiffness matrix has only positive or zero eigenvalues. Furthermore, if the structure

is kinematically indeterminate, then there exists a displacement vector $\boldsymbol{\rho}\,(\neq \mathbf{0})$ satisfying $\mathbf{D}^{\mathrm{T}}\mathbf{p} = \mathbf{0}$. Therefore, $\mathbf{p}^{\mathrm{T}}\mathbf{K}_{\mathrm{E}}\mathbf{p}$ vanishes [157] and Eq. (4.44) can be reduced.

The linearized tangent stiffness matrix [13] $\mathbf{K}_{\mathrm{T}} \in \mathbb{R}^{3n\times 3n}$ is calculated with $\mathbf{D}$ and $\mathbf{A}$ from Eqs. (4.14) and (4.15):

$$\mathbf{K}_{\mathrm{E}} = \mathbf{A}diag(\boldsymbol{\kappa})\mathbf{A}^{\mathrm{T}}\ , \tag{4.45}$$

$$\mathbf{K}_{\mathrm{G}} = \mathbf{I}_{(d\times d)} \otimes \mathbf{D}\ , \tag{4.46}$$

where $\mathbf{K}_{\mathrm{E}} \in \mathbb{R}^{3n\times 3n}$ is the elastic stiffness matrix, $\mathbf{K}_{\mathrm{G}} \in \mathbb{R}^{3n\times 3n}$ is the geometric stiffness matrix, $\mathbf{I}_{(d\times d)} \in \mathbb{R}^{d\times d}$ is the $d \times d$ identity matrix, and $\otimes$ is the Kronecker delta product. Finally,

$$\mathbf{K}_{\mathrm{T}} = \mathbf{K}_{\mathrm{E}} + \mathbf{K}_{\mathrm{G}}\ . \tag{4.47}$$

In the linearized theory of elastic frameworks, the tangent stiffness operator, $\mathbf{K}_{\mathrm{T}}$, provides the linear relation between displacement increments and load increments [158]

$$\mathbf{K}_{\mathrm{T}}\Delta\mathbf{p} = \Delta\mathbf{f}\ . \tag{4.48}$$

Stability

The stability analysis is performed when the tensegrity structure is in an equilibrium position. If $\mathbf{D}$ has all positive eigenvalues, then the structure is stable when no term higher than second-order terms of the potential energy are considered [96]. A non-trivial displacement is called mechanism if it does not change the member lengths.

A tensegrity structure can be in equilibrium but still be unstable. Super-stability is a special type of a stable self-equilibrated structure [159]. At the same time, a tensegrity without super stability may still be stable [74]. Because classification of equilibrium points is determined by the eigenvalues, this can be determined by investigating the eigenvalues of

the stiffness matrix.

The matrix $\mathbf{U}$, found from the SVD of $\mathbf{A}$ in Eq. (4.17), contains the internal mechanisms. Tensegrity structures are classified as statically and kinematically indeterminate pin-jointed systems [59, 104], i.e., $s > 0, m > 0$, where s is the number of self-stress states and the number of internal mechanisms is m. Therefore, their design requires consideration of the infinitesimal mechanisms associated to the system, and the corresponding states of self-stress capable to stabilize them [59].

There are two kinds of modes, characterized as either rigid or flexible body modes. All structures can have up to six rigid body modes, per DOF, three translational modes and three rotational modes. In traditional analysis of free-standing structures, rigid body motions are not considered in the stability analysis. The number of independent rigid body motions r is given by

$$r = \frac{d(d+1)}{2}. \tag{4.49}$$

The stability of tensegrities is generally studied using the spectral characteristics of the force density matrix. Any rigid-body motion of a structure will result in a structural stiffness matrix with zero eigenvalues [44]. Constraint conditions must be applied properly to exclude all possible rigid body motions [44]. This is because a negative eigenvalue of the stiffness matrix indicates that the structure is unstable, whereas a zero eigenvalue causes divergence of the numerical procedure [44]. Here the rigid body modes are properly constrained by excluding the r zero eigenvalues in the structural stiffness matrix [160].

The found equilibrium state is stable if the necessary condition for the stability of indeterminate pin-jointed structures with symmetry is satisfied [74]. This is established based on the eigenvalues of the quadratic form of the tangent stiffness matrix [65, 96]:

$$\mathbf{p}^{\mathrm{T}}\, \mathbf{K}_{\mathrm{T}} \mathbf{p} > 0\ . \tag{4.50}$$

Consider the differential equation $\dot{x}(t) = Ax(t)$, with initial condition $x(0) = v_0$, then $x(t) = v_0 e^{\lambda t}$ is the solution. Thus, the eigenvalues, λ, are the key indicator of the stability of the differential equation $\dot{x}(t) = Ax(t)$. The stability of tensegrity structures can be defined by the smallest eigenvalue of $\mathbf{K}$. Assuming all members have infinite stiffness, the stability of the structure can be verified by the sign of the eigenvalue. When positive, the structure is stable; when it is negative, the structure is unstable. The minimum eigenvalue of $\mathbf{K}$ corresponds to the eigenvector which is the weakest direction for the structure to deform [96].

The minimum eigenvalue $\lambda_{\min}$ of a real symmetric matrix (such as $\mathbf{K}_{\mathrm{T}}$) implies the positive definiteness of the matrix, and so the stability condition of the structure, independent of the selection of materials [120] is [160]

$$\lambda_{\min}\left(\mathbf{K}_{\mathrm{T}}\right) \begin{cases} > 0 & \text{stable ,} \\ = 0 & \text{critical ,} \\ < 0 & \text{unstable .} \end{cases} \tag{4.51}$$

The criteria shown in Eqs. (4.50) and (4.51) are the necessary and sufficient stability conditions in structural engineering [160].

A tensegrity structure is said to be super-stable if it is stable for any level of the self-equilibrium force densities without causing material failure. The conditions for a super-stable tensegrity are [161]:

1. Eq. (4.22) is satisfied,
2. Eq. (4.19a) is satisfied,
3. $\mathbf{D}$ has only positive or zero λs (Eq. (4.16)), and
4. $\operatorname{rank}\left(\mathbf{K}_{\mathrm{T}}\right) = r$ (from Eq. (4.49)), or equivalently, there are no affine (infinitesimal) flexes of the structure.

Chapter 5

Length-Changing Algorithm

The form-finding algorithm has a tendency to produce widely varying results and should be used only as an initial tool. The length-changing algorithm starts with a tensegrity structure that is close to an equilibrium position. The procedure perturbs a node slightly to a new position, i.e., changes the length of a member, and then finds the new corresponding closest equilibrium of the system. The following algorithm steps through length changes and then iteratively solves for the new equilibrium position.

5.1 Key equations

Variable definitions

A left superscript of i denotes a variable's value at the i^{th} iteration. The following procedure was also implemented in MATLAB version 2016a. The length-changing algorithm uses a numerical iterative approach based on the Force-Displacement Relationship combined with the NRM. The input variables needed for the length-changing algorithm are: ${}^0\mathbf{x}$, ${}^0\mathbf{y}$, and ${}^0\mathbf{z}$ (Eq. (4.4)), $\mathbf{q}$ (Eq. (4.3)), and $\boldsymbol{\kappa}$ (Eq. (4.35)).

The following variables can be calculated using the input variables. The matrix of projected length vectors $\boldsymbol{\Sigma} \in \mathbb{R}^{b\times 3}$ is

$$ {}^i\boldsymbol{\Sigma} = \mathbf{C} \begin{bmatrix} {}^i\mathbf{x} \\ {}^i\mathbf{y} \\ {}^i\mathbf{z} \end{bmatrix} . \tag{5.1} $$

The modified matrix $\overline{\boldsymbol{\sigma}}$ is formed by stacking the column vectors of $\boldsymbol{\Sigma}$:

$$^{i}\overline{\boldsymbol{\sigma}} = \begin{bmatrix} \boldsymbol{\sigma}_1 & \boldsymbol{\sigma}_2 & \boldsymbol{\sigma}_3 \end{bmatrix}^{\mathrm{T}} , \tag{5.2}$$

and so the length can be computed by

$$^{i}\boldsymbol{\ell} = \sqrt{\overline{\boldsymbol{\sigma}}^{\mathrm{T}}\overline{\boldsymbol{\sigma}}} , \tag{5.3}$$

which is equivalent to using vector magnitude:

$$\ell_b = \sqrt{(x_{bk} \text{ - } x_{bj})^2 + (y_{bk} \text{ - } y_{bj})^2 + (z_{bk} \text{ - } z_{bj})^2} , \tag{5.4}$$

where member b is connected to nodes j (x_{bj}, y_{bj}, z_{bj}) and k (x_{bk}, y_{bk}, z_{bk}). The b^{th} component of $\boldsymbol{\ell}$, ℓ_b, depends on the member.

The Jacobian matrix $\mathbf{J} \in \mathbb{R}^{3n \times 3n}$ is computed by

$$^{i}\mathbf{J} = \begin{bmatrix} \mathbf{C}^{\mathrm{T}} \operatorname{diag}\left(\mathbf{C}\ ^{i}\mathbf{x}^{\mathrm{T}}\right) \operatorname{diag}\left(\frac{1}{^{i}\boldsymbol{\ell}}\right) \\ \mathbf{C}^{\mathrm{T}} \operatorname{diag}\left(\mathbf{C}\ ^{i}\mathbf{y}^{\mathrm{T}}\right) \operatorname{diag}\left(\frac{1}{^{i}\boldsymbol{\ell}}\right) \\ \mathbf{C}^{\mathrm{T}} \operatorname{diag}\left(\mathbf{C}\ ^{i}\mathbf{z}^{\mathrm{T}}\right) \operatorname{diag}\left(\frac{1}{^{i}\boldsymbol{\ell}}\right) \end{bmatrix} . \tag{5.5}$$

Notice $\mathbf{J}$ has a very similar definition to $\mathbf{A}$, except its components are divided by $\boldsymbol{\ell}$. The Jacobian can be computed in other ways; see e.g., Refs. [47, 123].

The member internal force vector $\mathbf{t} \in \mathbb{R}$ can be computed using Hooke's Law:

$$^{i}\mathbf{t} = \operatorname{diag}\left(^{i}\boldsymbol{\kappa}\right)\left(^{i}\boldsymbol{\ell} \text{ - } \boldsymbol{\ell}_0\right) . \tag{5.6}$$

Eq. (5.6) can be used for struts as well, where t is now a compressive force (a negative value) because struts have a negative $(^{i}\boldsymbol{\ell} \text{ - } \boldsymbol{\ell}_0)$.

Assuming $\boldsymbol{\ell}$, $\mathbf{q}$ and $\boldsymbol{\kappa}$ are known, $^{i}\mathbf{t}$ can be computed by rearranging Eq. (4.3) as

$$^{i}\mathbf{t} = {}^{i}\mathbf{q}\,{}^{i}\boldsymbol{\ell} . \tag{5.7}$$

Then substituting Eq. (4.35) into Eq. (5.6) and solving for $\boldsymbol{\ell}_0$ yields [59, 75, 162]

$$\boldsymbol{\ell}_0 = \frac{\mathbf{ea}\ {}^i\boldsymbol{\ell}}{{}^i\mathbf{t} + \mathbf{ea}}\ . \tag{5.8}$$

Once $\boldsymbol{\ell}_0$ has been found, this vector is unchanging until a cable is actuated.

The secant stiffness matrix, an approximation for the tangent stiffness matrix, at the i^{th} iteration ${}^i\mathbf{K}_{\text{n}} \in \mathbb{R}^{3n\times 3n}$ is calculated using ${}^i\mathbf{J}$ (Eq. (5.5)):

$${}^i\mathbf{K}_{\text{n}} = \mathbf{I}_{(3\times 3)} \otimes (\mathbf{D}) + {}^i\mathbf{J}\ \text{diag}\,(\boldsymbol{\kappa})\ {}^i\mathbf{J}^{\text{T}} \text{ - } {}^i\mathbf{J}\ \text{diag}\,(\mathbf{q})\,{}^i\mathbf{J}^{\text{T}}\ . \tag{5.9}$$

${}^i\mathbf{K}_{\text{n}}$ will be singular because one of its eigenvalues will be zero due to the presence of at least one rigid body mode. Notice that Eq. (5.9) is nearly identical to Eq. (4.47). A distinction should be made between $\mathbf{K}$, the modal stiffness matrix, which looks at the system dynamics and $\mathbf{K}_{\text{T}}$, the tangent stiffness matrix, and $\mathbf{K}_{\text{n}}$, the secant stiffness matrix, which provide the statics.

Computing the error

The matrix of member force vectors ${}^i\mathbf{F}_{\text{m}} \in \mathbb{R}^{3\times b}$

$${}^i\mathbf{F}_{\text{m}} = {}^i\boldsymbol{\Sigma}^{\text{T}}\text{diag}\left({}^i\mathbf{q}\right)\ , \tag{5.10}$$

is a projection of the force densities along the member projected lengths and it is used to compute the matrix of resultant nodal force vectors ${}^i\mathbf{F}_{\text{n}} \in \mathbb{R}^{3\times b}$:

$${}^i\mathbf{F}_{\text{n}} = \text{-}{}^i\mathbf{F}_{\text{m}}\mathbf{C} + {}^i\mathbf{F}_{\text{e}}\ , \tag{5.11}$$

where $\mathbf{F}_{\text{e}} \in \mathbb{R}^{3\times n}$ is the matrix of node external force vectors. This is a matrix of zeros for a structure with no externally applied loads. Then, the column vectors of $\mathbf{F}_{\text{n}}$ are stacked vertically and used to calculate $\mathbf{F}_{\text{v}}$, where the error is the 2-norm of ${}^i\mathbf{f}_{\text{v}} \in \mathbb{R}^{3n}$:

$$|| \, {}^i\mathbf{f}_{\mathrm{v}} \, ||^2 = \left|\left| \begin{bmatrix} {}^i\mathbf{f}_1 & \dots & {}^i\mathbf{f}_{\mathrm{n}} \end{bmatrix}^{\mathrm{T}} \right|\right|^2 . \tag{5.12}$$

5.2 Iterative procedure

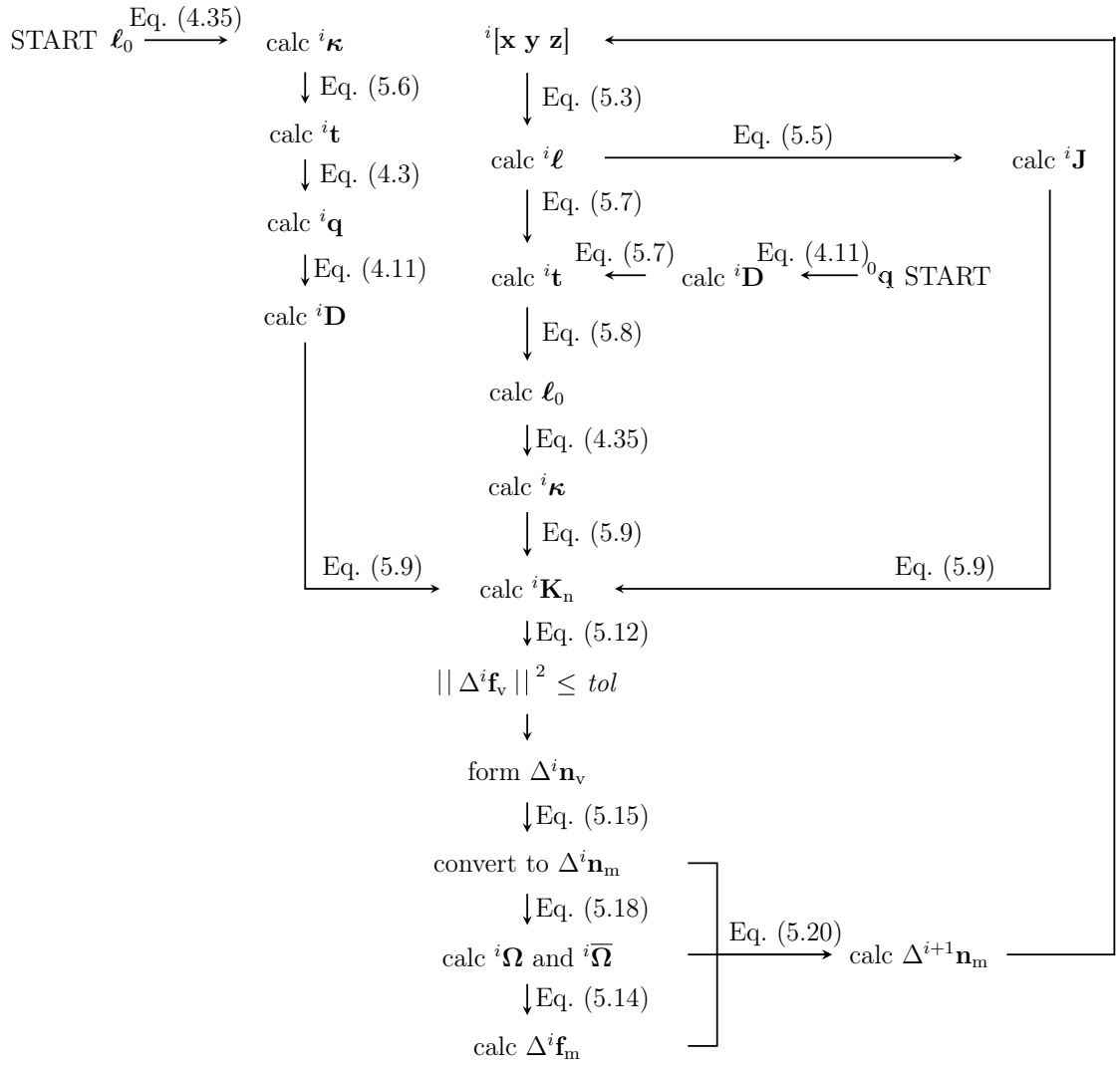

Figure 5.1: Length-changing algorithm flow diagram

In physical space:

$$\Delta^i\mathbf{f}_{\mathrm{v}} = {}^i\mathbf{K}_{\mathrm{n}}\Delta^i\mathbf{n}_{\mathrm{v}} \ , \tag{5.13}$$

where $\mathbf{n}_{\mathrm{v}} = [\mathbf{x}\ \mathbf{y}\ \mathbf{z}]^{\mathrm{T}}$. Here a displacement vector $\mathbf{n}_{\mathrm{v}}$ is mapped to a force vector $\mathbf{f}_{\mathrm{v}}$ by $\mathbf{K}_{\mathrm{n}}$. If $\mathbf{n}_{\mathrm{v}}$ and $\mathbf{f}_{\mathrm{v}}$ point in the same direction, they are called eigenvectors. Thus, the ratio of the length of vector $\mathbf{f}_{\mathrm{v}}$ to the length of vector $\mathbf{n}_{\mathrm{v}}$ is ω, an eigenvalue of $\mathbf{K}$. If a structure is stable, then its stiffness matrix is invertible, i.e., cannot have an eigenvalue of zero. Otherwise, the structure is free to move or deflect without deforming. In other words, for a given force vector and a singular $\mathbf{K}$, there is more than one displacement vector, i.e., there is not a unique displacement for a given force.

In structural mechanics, the system is linearized about a particular configuration by $\mathbf{K}_{\mathrm{T}}$, a linearization operator that describes the change in the stiffness of a system in response to small displacements imposed by the current configuration.

In modal space:

$$\Delta^i \mathbf{f}_{\mathrm{m}} = {}^i\mathbf{\Omega} \Delta^i \mathbf{n}_{\mathrm{m}} \ , \tag{5.14}$$

where $\Delta^i \mathbf{f}_{\mathrm{m}} \in \mathbb{R}^{3n}$ is the nodal DOF force vector, ${}^i\mathbf{\Omega} \in \mathbb{R}^{3n \times 3n}$ is the diagonal matrix of ${}^i\mathbf{K}_{\mathrm{n}}$'s eigenvalues, and $\Delta^i \mathbf{n}_{\mathrm{m}} \in \mathbb{R}^{3n}$ is the displacement vector in modal space.

Transform to modal space

The linear transformation to modal space is analogous to changing the coordinate basis $\mathbf{\Psi}$ of the matrix, i.e.,

$$\Delta^i \mathbf{n}_{\mathrm{m}} = {}^i\mathbf{\Psi}^{-1} \Delta^i \mathbf{n}_{\mathrm{v}} \ , \tag{5.15}$$

where ${}^i\mathbf{\Psi} \in \mathbb{R}^{3n \times 3n}$ is a matrix with columns that are eigenvectors, commonly referred to as the modal matrix, because

$${}^i\mathbf{K}_{\mathrm{n}} = {}^i\mathbf{\Psi}\, {}^i\mathbf{\Omega}\, {}^i\mathbf{\Psi}^{-1} \ . \tag{5.16}$$

Assuming harmonic motion, ${}^i\mathbf{\Omega}$ contains all of the eigenvalues of ${}^i\mathbf{K}_{\mathrm{n}}$. This mapping of

$\mathbf{K}_n \rightarrow \mathbf{\Omega}$ is called a similarity transformation, where $\mathbf{\Omega}$ essentially represents $\mathbf{K}_n$ in a different basis. Reduction means a transformation that preserves the eigenvalues of a matrix. Since $\mathbf{\Omega}$ will have at least one zero eigenvalue due to rigid body motion, it will always be less than full rank, and therefore, not invertible. The modal matrix makes it possible to include all the orthogonality relations in one equation. The product performed in Eq. (5.16) results in a diagonal matrix since the off-diagonal terms express the orthogonality relations which are zero.

When all ω are non-zero, the inverse of a diagonal matrix exists by $\mathbf{\Omega}^{-1} = \text{diag}\,(\boldsymbol{\omega}^{-1})$. Taking the inverse of both sides of Eq. (5.16) yields

$$ {}^{i}\mathbf{K}_{\text{n}}^{-1} = \left({}^{i}\mathbf{\Psi}\,{}^{i}\mathbf{\Omega}\,{}^{i}\mathbf{\Psi}^{-1}\right)^{-1} = {}^{i}\mathbf{\Psi}\,{}^{i}\mathbf{\Omega}^{-1}\,{}^{i}\mathbf{\Psi}^{-1} \ . \tag{5.17} $$

Similar matrices have the same eigenvalues. Thus, define diagonal "inverse" matrix $\overline{\mathbf{\Omega}} \in \mathbb{R}^{3n \times 3n}$ as

$$ {}^{i}\overline{\mathbf{\Omega}} = \text{diag}\left(\begin{bmatrix} \frac{1}{{}^{i}\omega_1} & \cdots & \frac{1}{{}^{i}\omega_{3n-6}} \end{bmatrix}\right) \ . \tag{5.18} $$

The other six diagonal entires of ${}^{i}\overline{\mathbf{\Omega}}$ will be zero because rigid body motion is excluded. This inverse removes the six rigid body modes which have $\omega = 0$, i.e., modes in which all nodes translate or rotate together without altering their relative position. These modes are not relevant for changing the internal forces on the nodes. A rigid-body motion will preserve the length of all members, where the number of independent rigid body motions is given by r.

The solution can be approximated using the NRM. If the Jacobian matrix evaluated at the vector ${}^{i}\mathbf{p}$ is known, then the next trial value of the unknown vector should be

$$ {}^{i+1}\mathbf{p} = {}^{i}\mathbf{p} - \left[\frac{\partial \mathbf{f}}{\partial \mathbf{p}}\right]\Bigg|_{\mathbf{p}={}^{i}\mathbf{p}} \left({}^{i}\mathbf{f} - {}^{0}\mathbf{f}\right) \ . \tag{5.19} $$

The NRM is used to iteratively solve Eq. (5.14):

$$^{i+1}\mathbf{n}_{\mathrm{m}} = {}^{i}\mathbf{n}_{\mathrm{m}} + {}^{i}\overline{\mathbf{\Omega}}\Delta^{i}\mathbf{f}_{\mathrm{m}} \ , \tag{5.20}$$

where $^{0}\mathbf{n}_{\mathrm{m}}$ is an initial guess for $\mathbf{n}_{\mathrm{m}}$. Eq. (5.20) is used to change the nodal coordinates until the 2-norm of $\mathbf{f}_{\mathrm{v}}$ (Eq. (5.12)) is within *tol*. If $\mathbf{f}_{\mathrm{v}}$ is greater than *tol*, then $i = i+1$, $^{i}[\mathbf{x}\ \mathbf{y}\ \mathbf{z}]$ are extracted from $\mathbf{n}_{\mathrm{v}}$, and $\mathbf{K}$ is recalculated. The process is repeated for t iterations. Fig. 5.1 shows an illustrative flow chart of the full iterative process.

Modal analysis

After the length-changing algorithm converges, i.e., $||^{i}\mathbf{f}_{v}||^{2}$ (Eq. (5.12)), a dynamic calculation is performed to track the theoretical natural frequencies over the range of length changes. The total mass at each node is computed by summing half of the mass of each member that connects to the node, as in

$$m_{\mathrm{N1,N2,...,N}n} = \frac{\sum_{\gamma=1}^{p} \mathrm{m}_{\gamma}}{2} \ , \tag{5.21}$$

where $\mathrm{m}_{1\text{–}p}$ are the masses of each of the p members that are concentrated at one node. In other words, equation (5.21) says that $m_{\mathrm{N1}} = \frac{\mathrm{m}_1+\mathrm{m}_2+\cdots+\mathrm{m}_p}{2}$ is the total mass at N1. Then, the mass matrix $\mathbf{M} \in \mathbb{R}^{3n\times 3n}$ can be assembled by:

$$\mathbf{M} = \mathbf{I}_{(3n\times 3n)} \cdot \left\{ m_{\mathrm{N1}} \quad m_{\mathrm{N1}} \quad m_{\mathrm{N1}} \quad m_{\mathrm{N2}} \quad m_{\mathrm{N2}} \quad m_{\mathrm{N2}} \quad \ldots \quad m_{\mathrm{N}n} \quad m_{\mathrm{N}n} \quad m_{\mathrm{N}n} \right\}^{\mathrm{T}} \ . \tag{5.22}$$

Although $\mathbf{M}$ is not a traditional mass matrix as in Refs. [163] or [148], it is comparable to scaling the identity matrix [13]. Similarly, DRM uses lumped nodal masses [123].

The general undamped equations of motion (EOMs) for a tensegrity structure are:

$$\mathbf{M}\ddot{\mathbf{u}} + \mathbf{K}_{T}\mathbf{u} = \mathbf{f} \ , \tag{5.23}$$

where $\mathbf{K}_T$ is from Eq. (4.47), $\mathbf{u}$ is the nodal displacement vector, and $\mathbf{f}$ is the nodal external force vector. Alternatively, the EOMs of a tensegrity structure can be formulated via Euler-Lagrangian [164].

The modal analysis is conducted via eigenvalue analysis, where the natural frequencies of the system are given by the roots of the characteristic equation [33, 37]. The eigenvalue problem,

$$\mathbf{K}_{\mathrm{T}}\mathbf{u} = \omega^2\mathbf{M}\mathbf{u} \ , \tag{5.24}$$

where ω is the natural frequency in $\frac{\mathrm{rad}}{\mathrm{s}}$, can be easily solved for the undamped natural frequencies. This can be rearranged as

$$\Big[\mathbf{K} \text{ - } \omega^2\mathbf{M}\Big]\,\mathbf{u} = \mathbf{0} \ , \tag{5.25}$$

where the EVD gives the natural frequencies ω and the related mode shapes $\mathbf{u}$ [75]. Again, at least one of the eigenvalues of $\mathbf{K}$ will be zero due to rigid body modes, and it is also square and symmetric, i.e., $[K] = [K]^{\mathrm{T}}$. Recall this was also the case with $\mathbf{D}$, which allowed us to perform the EVD. To solve Eq. (5.25), the EVD of $\mathbf{K}$ and $\mathbf{M}$ is employed to solve for ω^2, the eigenvalues of the mass-normalized stiffness matrix. The spectral decomposition of matrix $\mathbf{M}^{-1}\mathbf{K}$ then yields the natural frequencies and corresponding mode shapes of the finite element model (FEM) of the structure. From here, using Eq. (5.27), the length of a member can be directly changed and carried through the procedure to find the new tangent stiffness matrix.

Converting length change into nodal change

Once an equilibrium position is found and a modal analysis has been performed on the system, the algorithm proceeds to adjust the length of certain members, depending on which actuation strategy is being modeled.

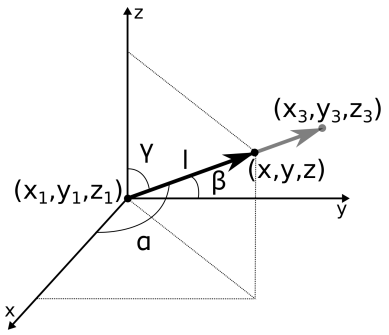

Figure 5.2: Length change coordinate system

In Fig. 5.2, the angles α, β, and γ are shown for a member of length ℓ. The angles are computed by

$$\gamma = \cos^{-1}\left(\frac{z_3 - z_1}{\sqrt{(x_3 - x_1)^2 + (y_3 - y_1)^2 + (z_3 - z_1)^2}}\right) , \tag{5.26a}$$

$$\beta = \cos^{-1}\left(\frac{y_3 - y_1}{\sqrt{(x_3 - x_1)^2 + (y_3 - y_1)^2 + (z_3 - z_1)^2}}\right) , \tag{5.26b}$$

and

$$\alpha = \cos^{-1}\left(\frac{x_3 - x_1}{\sqrt{(x_3 - x_1)^2 + (y_3 - y_1)^2 + (z_3 - z_1))^2}}\right) . \tag{5.26c}$$

The new nodal coordinate, (x_3, y_3, z_3), is found via

$$x = \ell\cos(\alpha) + x_1 , \tag{5.27a}$$

$$y = \ell\cos(\beta) + y_1 , \tag{5.27b}$$

and

$$z = \ell\cos(\gamma) + z_1 . \tag{5.27c}$$

The choice for the construction of the connectivity (see Eq. (4.5), and Fig. 4.1) was made

due to the fact that the nodal constraints occur at the base nodes. Thus, as shown in Fig. 5.2, the length changing formulas (Eqs. (5.26) and (5.27)) only alters the "higher number" nodes, i.e., the unconstrained nodes.

Chapter 6

Experiment

6.1 Investigated tensegrity structures

Schematics of the experimentally tested tensegrities are shown in Figs. 6.1– 6.3. The studied structures are a free-free one-stage prism (FFP) shown in Fig. 6.1, a clamped-free one-stage prism (CFP) shown in Fig. 6.2, and a clamped-free three-stage tensegrity mast (CFM) shown in Fig. 6.3. The corresponding tables are shown in Figs. 6.1 (b), 6.2 (b), and 6.3 (b), where the mass of the b^{th} member is indicated by m_b, the diameter of the b^{th} member is d_b, and the lengths ℓ are applicable to the starting configuration. Each member and node is labeled according to the diagrams in Figs. 6.1 (a), 6.2 (a), and 6.3 (a) to distinguish between cables during testing.

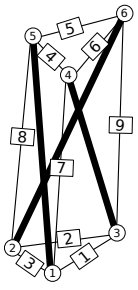

(a) Labeled diagram

Variable	Value	Variable	Value
m_{1-9}	0.0103 $\frac{\text{kg}}{\text{m}}$	$\ell_{1,3,4,6}$	16.5 cm
m_{10-12}	0.1392 $\frac{\text{kg}}{\text{m}}$	$\ell_{2,5}$	25.5 cm
$\text{m}_{\text{structure}}$	0.3813 kg	ℓ_{7-9}	41.5 cm
d_{1-9}	1.6 mm	ℓ_{10-12}	46.0 cm
d_{10-12}	15.88 mm	e_{1-12}	$11 \times 10^9 \frac{\text{N}}{\text{m}^2}$

(b) Mass, length, Young's modulus, and diameter

Figure 6.1: Free-Free Prism (FFP)

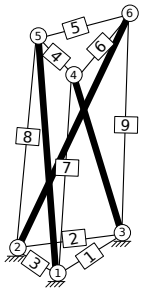

(a) Labeled diagram

Variable	Value	Variable	Value
m_{1-9}	0.0103 $\frac{kg}{m}$	$\ell_{1,3,4,6}$	16.5 cm
m_{10-12}	0.2889 $\frac{kg}{m}$	$\ell_{2,5}$	25.5 cm
$m_{structure}$	0.8887 kg	ℓ_{7-9}	39.8 cm
d_{1-9}	1.6 mm	ℓ_{10-12}	45.0 cm
d_{10-12}	7.9 mm	e_{1-12}	$200 \times 10^9 \frac{N}{m^2}$

(b) Mass, length, Young's modulus, and diameter

Figure 6.2: Clamped-Free Prism (CFP)

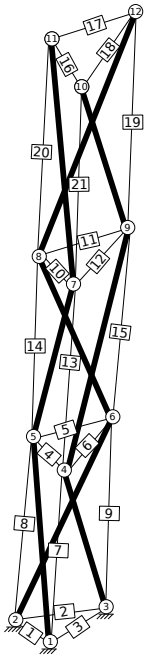

(a) Labeled diagram

Variable	Value	Variable	Value
m_{1-21}	0.0103 $\frac{kg}{m}$	$\ell_{1,3,4,6,10,12,16,18}$	15 cm
m_{22-30}	0.2889 $\frac{kg}{m}$	$\ell_{2,5}$	25 cm
$m_{structure}$	2.7178 kg	$\ell_{7-9,13-15,19-21}$	39.5 cm
d_{1-21}	1.6 mm	ℓ_{22-30}	45.0 cm
d_{22-30}	7.9 mm	e_{1-30}	$200 \times 10^9 \frac{N}{m^2}$

(b) Mass, length, Young's modulus, and diameter

Figure 6.3: Clamped-Free Mast (CFM)

Test articles

(a) Free-free prism (FFP)

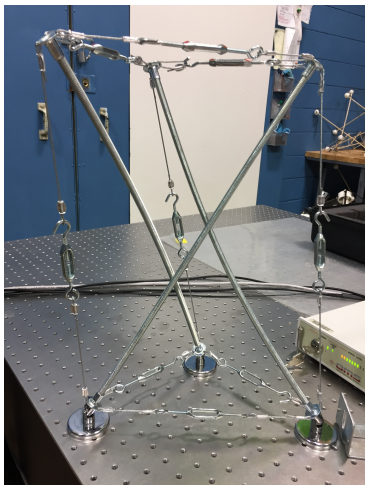

(b) Clamped-free prism (CFP)

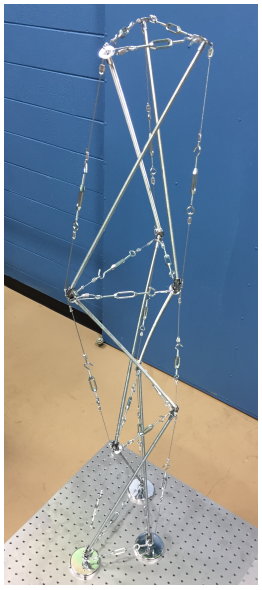

(c) Clamped-free mast (CFM)

Figure 6.4: Photographs of test articles

Photographs of the FFP, CFP, and CFM test articles are shown in Fig. 6.4. The CFP and CFM test articles have struts made of threaded steel rods. The FFP is constructed with oak wooden dowels. All test articles have steel cables.

Structures can be tested under various boundary conditions. In the free-free boundary condition, the test structure is freely supported in space and is not attached at any of its nodes. It is not possible to provide a truly free-free support in practice but it is feasible to approximate this condition by supporting the test structure on very soft springs, such as light elastic cords. In this case, the FFP was placed on a soft foam, as shown in Fig. 6.4a, while three base nodes are fixed for the CFP, shown in Fig. 6.4b, and CFM, in Fig. 6.4c. The method of supporting a structure during vibration testing has a direct impact on the modal characteristics of the structure.

Design and construction

All tensegrities used here are non-redundant. This means that the members are held together in a self-stressed state. The construction process is therefore challenging because the structure does not take shape until the last member is attached. For this reason, initial forethought and design planning is required to build one of these structures. The tensegrity prism was chosen because it is one of the simplest three-dimensional tensegrity structures. The demo units shown in Fig. 6.5 were constructed first and used to inform the dimensions of the test articles. The geometry was defined to prevent any members from coming into contact with each other during actuation. Because this work focuses on the use of tensegrity systems for aeronautical applications, it was desirable for the system to have a wing-like shape. The CFM, shown in Fig. 6.3, was constructed with a span of about 127 cm and a cord of about 30 cm, giving an aspect ratio of 4.2, which is comparable to an aircraft wing [165].

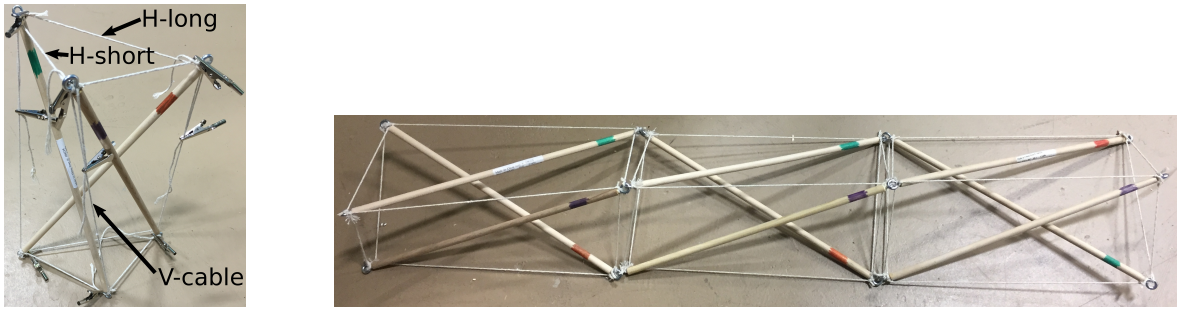

(a) Prism (b) Mast

Figure 6.5: Demo units

Each prism demo unit was constructed out of string attached by eye-hooks to the end of three 300 mm oakwood dowels. This structure was not tested during the experiment. It was used to learn how the tensegrity prism geometry changes with changing string lengths. The string was initially left untied and secured by clips (see Fig. 6.5a), allowing the lengths to be adjusted.

Cable	Lengths (cm)
H-short	2.8
H-long	7.3
V-cable	15.2

Table 6.1: Unstretched half-cable lengths for all test articles

Fig. 6.4 shows that the FFP and CFP test articles each have two parallel triangular bases, while the CFM has three. The FFP, CFP, and CFM have three types of cables: horizontal short (or H-short) referring to each set of two edges in each triangular base that have the smallest length, horizontal long (or H-long) representing the longer edge of a triangular base, and vertical cables (or V-cables) denoting the rest of the cables that run vertically (see Fig. 6.5a). For the test articles, each cable was cut into "half-cables" (lengths shown in Table 6.1) to insert an actuator. The half-lengths can be used to approximate the unstretched cable length Once the tensegrity is fully assembled, each cable is pre-stressed to length ℓ.

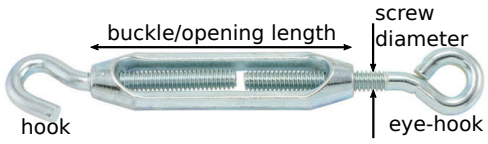

Figure 6.6: Turnbuckle

The 4 mm × 32 mm turnbuckle displayed in Fig. 6.6 is a manual actuator, which shortens the cable length. The standard measuring convention for turnbuckles is screw diameter × buckle or opening length. The opening length is essentially a distance measurement of the change in length from a fully-closed to a fully-open position. Each turnbuckle can turn up to 20 times, where a full turn is counted when the buckle is rotated by 360 degrees or equivalently, when the buckle travels a distance of one screw threading. When the buckle turns, it travels an equal distance symmetrically along both screws, each having 18 turns per 25.4 mm. It is confirmed by measurement, that for every turnbuckle turn, the length of a cable will change by 1.5 mm per turn.

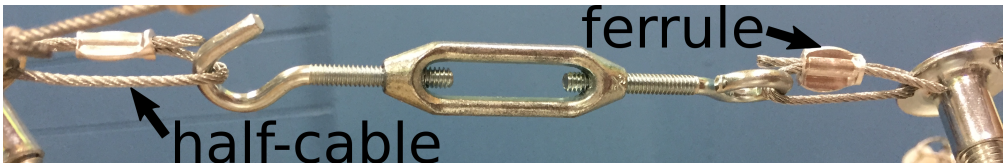

Figure 6.7: H-short cable

Each cable consists of two half-cables and a turnbuckle and the cable length is measured as the distance from one nodal connection point to the other.

The theoretical model assumes all nodes to be pin-joints, only restricting translations. Note this is different from a hinge joint which only permits one-dimensional rotation. It is difficult, in practice, to construct a class 2 (two struts attached at one node) tensegrity joint which achieves true pin-jointed motion. Instead, a universal joint (u-joint) is used for the CFM. A u-joint consists of a pair of hinges. A u-joint allows motion in two axes. For the CFM, two struts at one joint meet at an obtuse angle for every configuration change performed in this study. In turn, the pin-joint requirement can be relaxed, allowing the joints to be somewhat more restrictive on the members.

(a) T Nut

(b) U-joint

(c) Mast/mounting joint

Figure 6.8: CFP and CFM joint components

The CFP and CFM joints have been constructed according to Fig. 6.8 by connecting a u-joint (displayed in Fig. 6.8b) to a T nut (shown in Fig. 6.8a). The u-joint used here is a 6.4 mm socket adapter with female and male ends that have been tapped and threaded, respectively, to a 7.9 mm diameter. The tapped female end can connect to a strut, or to the mounting section. The threaded male end connects to a 7.9 mm $\times$ 16 mm brad hole T nut.

(a) Magnet

(b) Socket screw

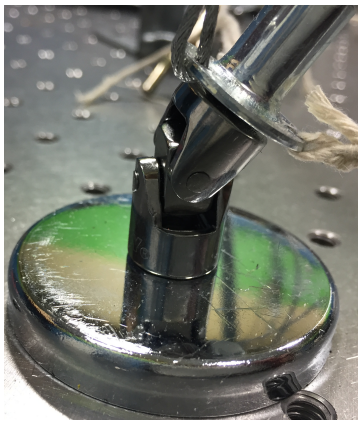

(c) Mounting section

Figure 6.9: CFP and CFM mounting components

The mounting section consists of three magnets as shown in Fig. 6.9a. Each have a maximum pull of 423 N for the CFM and 111 N for the CFP, and are used to fix one end of each test article at nodes 1, 2, and 3. Each magnet is connected to the u-joint via a 7.94 mm diameter screw shown in Fig. 6.9b. The screw‘s length cut to fit the span of the threading on the u-joint.

Part	Mass (g)	FFP	CFP	CFM
Turnbuckle	18.4	✓	✓	✓
U-joint	23.9		✓	✓
T-nut	7.08		✓	✓
Nylon washer	0.544	✓		
Ferrule	3.18	✓	✓	✓

Table 6.2: Masses for components of FFP, CFP, and/or CFM

Table 6.2 shows the masses of all of the components used to construct the test articles.

(a) FFP

(b) CFP

Figure 6.10: Free nodes

As shown in Fig. 6.10b, the free end of the CFP is a T nut, while, in Fig. 6.10a, the free end of the FFP are nylon washers. Switching to nylon washers greatly simplifies the construction process and eliminates extra weight. Plus, it makes it possible to construct a class 2 tensegrity in which the two struts have more freedom compared to the u-joint. This is

because the struts do not actually connect. Rather, they are held together by compression. The improved joint design also allows all members to connect around the same point, which should help reduce unwanted strut behavior, such as buckling. The trade off to this kind of joint is that the lack of connection between strut and joint complicates the assembly process.

(a) CFF cables assembly

(b) CFF struts

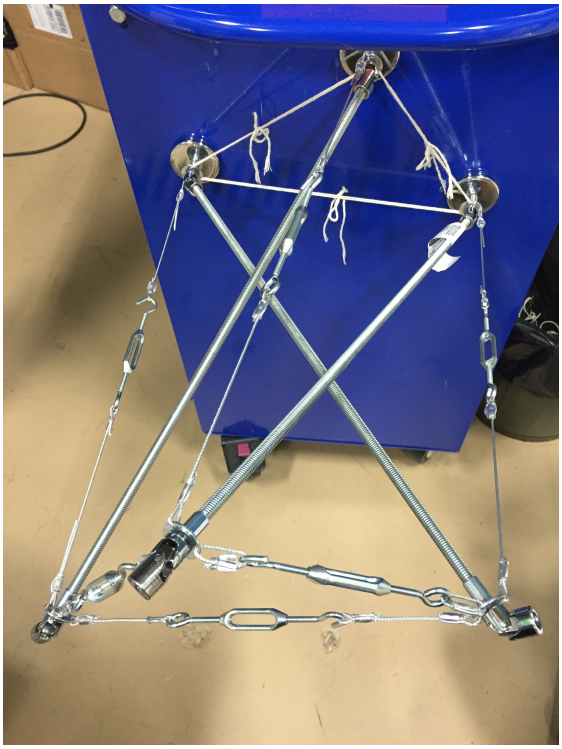

(c) Top view of horizontally mounted CFM

Figure 6.11: Prototype assembly photos

Fig. 6.11c shows the CFM mounted on a magnetic surface during the assembly process. The CFM was assembled one prism at a time, and the new struts are linked by alternating their rotation to the opposite direction. In other words, the direction of the three-strut rotation alternates between prism units to keep the mast straight. Without this alternating pattern, the mast would curl as in Refs. [12, 14, 32].

6.2 Modal testing

Modal testing is a form of vibration testing where the natural frequencies, modal masses, modal damping ratios, and mode shapes of a test article are determined from experimental data. A modal test consists of an acquisition phase and an analysis phase. The complete process is referred to as Experimental Modal Analysis (EMA). Impact hammer testing and shaker testing are common ways to accomplish a EMA. Impact hammer testing is ideal for small lightweight structures. Here, the three tensegrity test articles undergo impact hammer testing.

A wide variety of structures can be impact tested. A roving hammer test is the most common type of impact test. In this test, the response is collected at a node and the structure is roved at as many nodes as desired. Using a 2-channel FFT analyzer, FRFs are computed one at a time, between each impact DOF and the fixed response DOF. A drawback to impact hammer testing is that most structures cannot be impacted in all three directions, so three-dimensional motion cannot be measured at all points.

Equipment

The following equipment is needed to perform an impact test: an impact hammer (PCB 086B01) to excite the structure, an accelerometer or vibrometer to measure the response acceleration or velocity, respectively at a fixed point and direction, a two or four channel FFT analyzer to compute FRFs, and post-processing modal software for identifying modal parameters. A data acquisition analyzer (DAQ) from National Instruments is used for collecting the experimental data.

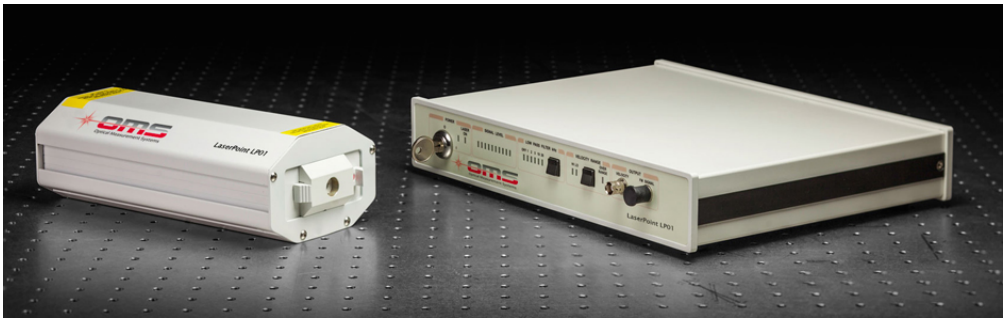

Figure 6.12: OMS LaserPoint LP01

In Fig. 6.12, a single point laser Dopper vibrometer (LDV) is a precision instrument widely used in experimental modal analysis that can measure vibrations of almost any object. LDVs are attractive because they are non-contact and generally do not require the measured surface to be treated. The OMS LaserPoint LP01 is used to measure the response of each test article to an input stimulation.

Actuation strategies

The goal of this study is to determine which combination of cables play a dominant role in the vibration response of tensegrity structures with various units of prisms. When only one cable is adjusted, this is referred to as the "ones" strategy. When horizontal, vertical, or alternating sets of cables are changed, these are referred to as "horizontal", "vertical", and "alternating" actuation strategies, respectively. The ones, horizontal, and vertical actuation strategies are performed for all three test articles, and the CFM has an additional alternating strategy. The targeted cables for each strategy are highlighted green in Figs. 6.14 and 6.15.

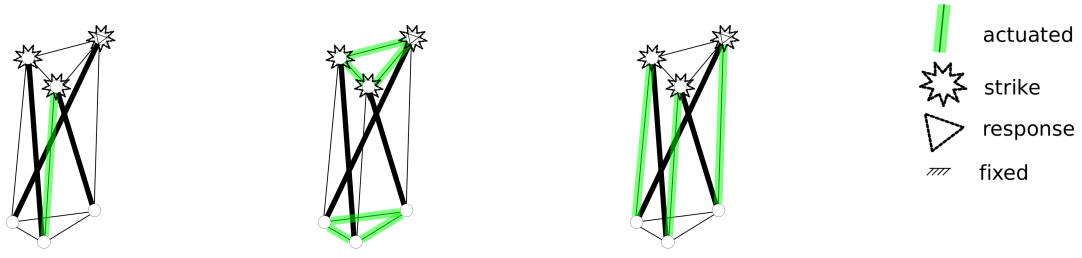

(a) Ones (b) Horizontal (c) Vertical

Figure 6.13: FFP actuation strategies

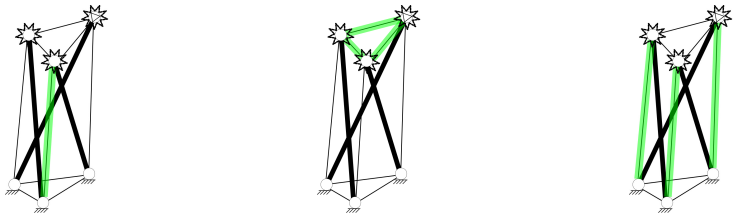

(a) Ones (b) Horizontal (c) Vertical

Figure 6.14: CFP actuation strategies

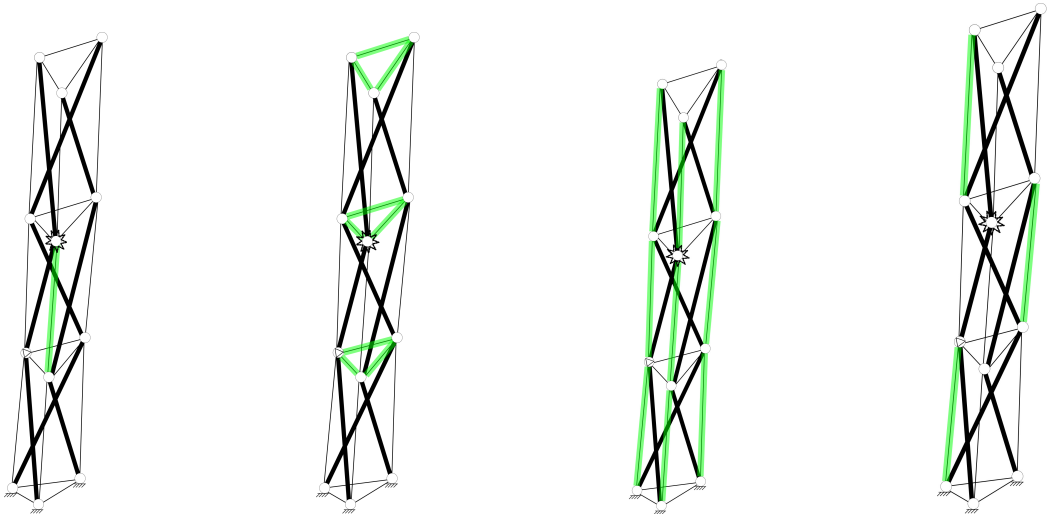

(a) Ones (b) Horizontal (c) Vertical (d) Alternating

Figure 6.15: CFM actuation strategies

Experimental procedure

Cable	FFP (cm)	CFP (cm)	CFM (cm)
H-short	16.5	16.5	17.0
H-long	25.5	25.5	26.0
V-cable	41.5	39.8	42.0

Table 6.3: Initial stretched cable lengths

The following step by step procedure was used:

1. The test articles started from an initial configuration, with initial lengths according to

Table 6.3. The cable length was measured and turnbuckles adjusted to achieve the proper initial condition.

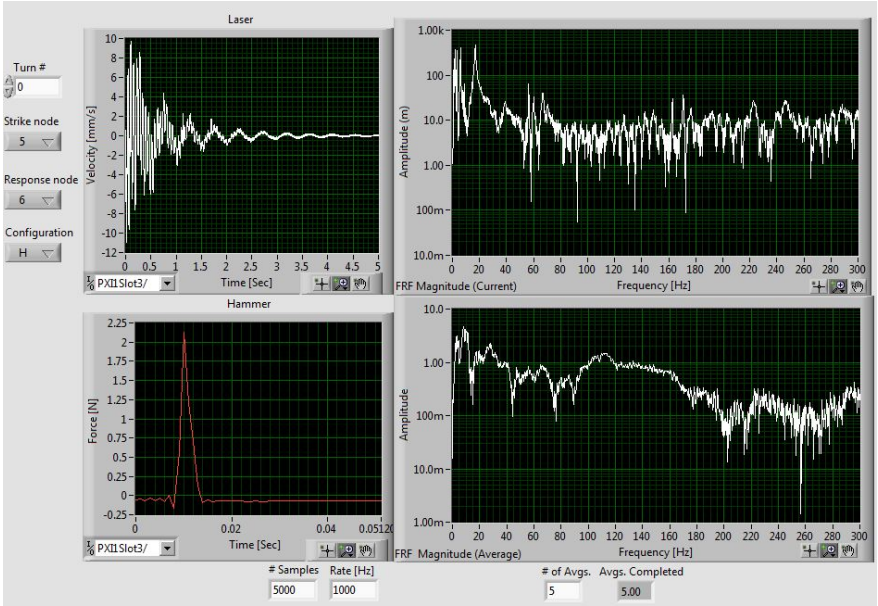

Figure 6.16: NI LabView front panel view

2. The laser and hammer signals were collected for 5000 samples at a rate of 1000 Hz. There are several important considerations that were taken into account to obtain accurate results. On the front panel, the user can select the numbers of the cables that are being changed for a given actuation strategy. The turn number was indicated to keep track of the length change increments. Additionally, the LabView script was programmed such that when a certain threshold voltage is met from impact force on the hammer, the program starts collecting data.

3. A universal joint or nylon washer was tapped with the hammer and the results were processed. Data collected from the LDV and hammer using the DAQ, from Fig. **??**, was stored using National Instruments (NI) Labview. A sample time history and impulse signal are displayed in Fig. 6.16.

4. An accept/reject capability also saves a lot of time during impact testing since the measurement process will not need to be restarted after every bad hit. When the program displayed the FRF after each hammer strike, the user was prompted to accept or reject the

data. Steps 2–4 were repeated for the desired strike points and the LDV was moved for the desired response nodes. The hammer was roved and laser was directed approximately perpendicular to a T nut or washer. The hammer and laser response are recorded for five averages to reduce the effects of noise.

5. The cable lengths were incrementally adjusted by turning the turnbuckle a half-turn, according to each actuation strategy, for up to five turns. The turn number was updated every time the turnbuckles were turned. The turnbuckles were turned uniformly, as in all of the cables were adjusted equal amounts.

6. Steps 2–5 were repeated for four different configurations (i.e., the ones, alternating, horizontal, and vertical strategies).

7. The results were analyzed for frequency content, and checked to ensure that the data sufficiently covered the desired frequency spectrum. The sets of data were exported from Labview and imported into Matlab for signal analysis.

6.3 Signal Analysis

The Frequency Response Function (FRF) is a fundamental measurement that isolates the inherent dynamic properties of a structure. Experimental modal parameters (frequency, damping, and mode shape) are also obtained from a set of FRFs. The FRF describes the input-output relationship between two points on a structure as a function of frequency. In reality, structures are continuous, having an infinite number of DOFs and an infinite number of modes. From a testing point of view, a real structure can be sampled spatially at as many DOFs as desired. There is no limit to the number of unique DOFs between which FRF measurements can be made. Only a small subset of the FRFs are necessary for accurately defining the modes. At the same time, more measurements give more definition to the modes.

A FRF is a complex valued function of frequency that is defined between a single input DOF, and a single output DOF. It is a measure of how much displacement, velocity, or acceleration response a structure has at an output DOF, per unit of excitation force at an

input DOF [166]. A FRF, $\mathbf{H}(\omega)$, describes the input-output relationship of the system. It is defined as the ratio of the FFT of the output response ($\mathbf{X}(\omega)$) divided by the FFT of the input force ($\mathbf{F}(\omega)$), in the frequency domain:

$$\mathbf{F}(\omega)\mathbf{H}(\omega) = \mathbf{X}(\omega) \ , \tag{6.1}$$

where each input and output corresponds to a DOF of the test structure.

Here the FFT is performed using the five averages of the laser response experimental data, and the FRF is obtained, as in Fig. 6.17. By dividing the FFT of the laser signal by the FFT of the hammer signal, Eq. (6.2), computed using [146]:

$$\mathbf{H}(\omega) = \mathbf{X}(\omega)\mathbf{F}(\omega)^{-1} \tag{6.2}$$

The CFM was tapped at nodes 7 and 9, while the FFP and CFP were tapped at 4, 5, and 6. All responses are taken at node 6. The FRF for each tapped node is overlayed, as in Fig. 6.17. The first five changing modes were tracked manually and recorded at each length change. The modes were tracked according to the highest FRF amplitude of the spectogram.

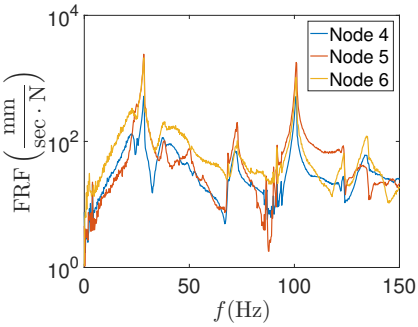

Figure 6.17: Example FRF for CFP

Responses from five hammer taps were averaged as well as the responses. Fig. 6.17 shows a sample of the FRF magnitude for striking nodes 4–6, where the overall structural response at any frequency is a summation of responses due to each mode. Close to the frequency of one

of the resonance peaks, the response of one mode will dominate the frequency response. At certain natural frequencies of the structure, a small amount of input force can cause a very large response. This is clearly evident from the narrow peaks in the FRF [166]. On the other hand, if the structure is excited at or near or near a frequency of one of the anti-resonances, the structural response will be very small per unit of input force.

Windowing and zero padding

Zero padding is simply adding zeros to the end of the time history to improve the frequency resolution. The Hann function is a discrete window function that is linear combination of modulated rectangular windows. The Hanning window is typically used in digital signal processing to select a subset of a series of samples in order to perform a FFT. The advantage of the Hanning window is low signal distortion, with the tradeoff being slightly decreased resolution. It is an offset cosine wave so it is always positive:

$$\mathbf{w}(n) = \frac{1}{2}\left(1 - \cos\left(\frac{2\pi n}{N}\right)\right),\ 0 \leq n \leq N\ , \tag{6.3}$$

where N is the NFFT value, the next power of two from the length of the signal. After zero padding, in this case, NFFT was 131,072. This function returns a Hanning window with L entries in a column vector $\mathbf{w}$, where L is the window length according to L=N+1. The sampled signal values are multiplied by the Hanning function, which forces the ends of the time record to zero regardless of the input signal.

Chapter 7

Results

7.1 Theoretical

The inputs for the length-changing algorithm are consistent with the FFP test article. This includes the connectivity, stiffnesses and masses of members, initial coordinates, and force density, with no external forcing. The mass at each node was computed by dividing the mass of the entire structure by the total number of nodes. The ℓ_0 value for each cable is changed ten times until an overall length change of 15 mm is reached.

The tensegrity prism has the following connectivity matrix $\mathbf{C}$:

$$\mathbf{C} = \begin{bmatrix} -1 & 0 & 1 & 0 & 0 & 0 \\ 0 & -1 & 1 & 0 & 0 & 0 \\ -1 & 1 & 0 & 0 & 0 & 0 \\ 0 & 0 & 0 & -1 & 1 & 0 \\ 0 & 0 & 0 & 0 & -1 & 1 \\ 0 & 0 & 0 & -1 & 0 & 1 \\ -1 & 0 & 0 & 1 & 0 & 0 \\ 0 & -1 & 0 & 0 & 1 & 0 \\ 0 & 0 & -1 & 0 & 0 & 1 \\ -1 & 0 & 0 & 0 & 0 & 1 \\ 0 & -1 & 0 & 1 & 0 & 0 \\ 0 & 0 & -1 & 0 & 1 & 0 \end{bmatrix}. \tag{7.1}$$

The Young's modulus of the members is $\mathrm{e} = 11 \cdot 10^9 \left(\frac{\mathrm{N}}{\mathrm{m}^2}\right)$ and the diameters of the cables and struts are

$$\mathbf{d} = \begin{cases} 1.6 \text{ (mm)} & \text{for all cables ,} \\ 7.9 \text{ (mm)} & \text{for all struts .} \end{cases} \tag{7.2}$$

The first iteration of $\mathbf{q}$ is

$${}^0\mathbf{q} = \begin{cases} 0.2041 & \text{for cables 1–6 ,} \\ 0.3536 & \text{for cables 7–9 ,} \\ -0.3536 & \text{for all struts .} \end{cases} \tag{7.3}$$

The initial nodal coordinates,

$${}^0\mathbf{x} = \begin{bmatrix} 0.125 & 0.000 & 0.251 & 0.198 & 0.036 & 0.250 \end{bmatrix}^{\mathrm{T}} , \tag{7.4}$$

$${}^0\mathbf{y} = \begin{bmatrix} 0.116 & 0.000 & 0.000 & 0.104 & 0.052 & -0.065 \end{bmatrix}^{\mathrm{T}} , \tag{7.5}$$

and

$${}^0\mathbf{z} = \begin{bmatrix} 0.040 & 0.040 & 0.040 & 0.435 & 0.435 & 0.435 \end{bmatrix}^{\mathrm{T}} , \tag{7.6}$$

are the measured nodal coordinates of the physical test article.

In the following figures, the total length change, ΔL, is divided by the total number of actuated cables, N, to distribute the length change across all of the changed cables, and f is the natural frequency. If N is calculated by 1.5 mm per turn times the number of turnbuckle turns times N, then N can be canceled out. The x-axis can therefore be thought of as the length change increment. The first six rigid body modes are excluded here.

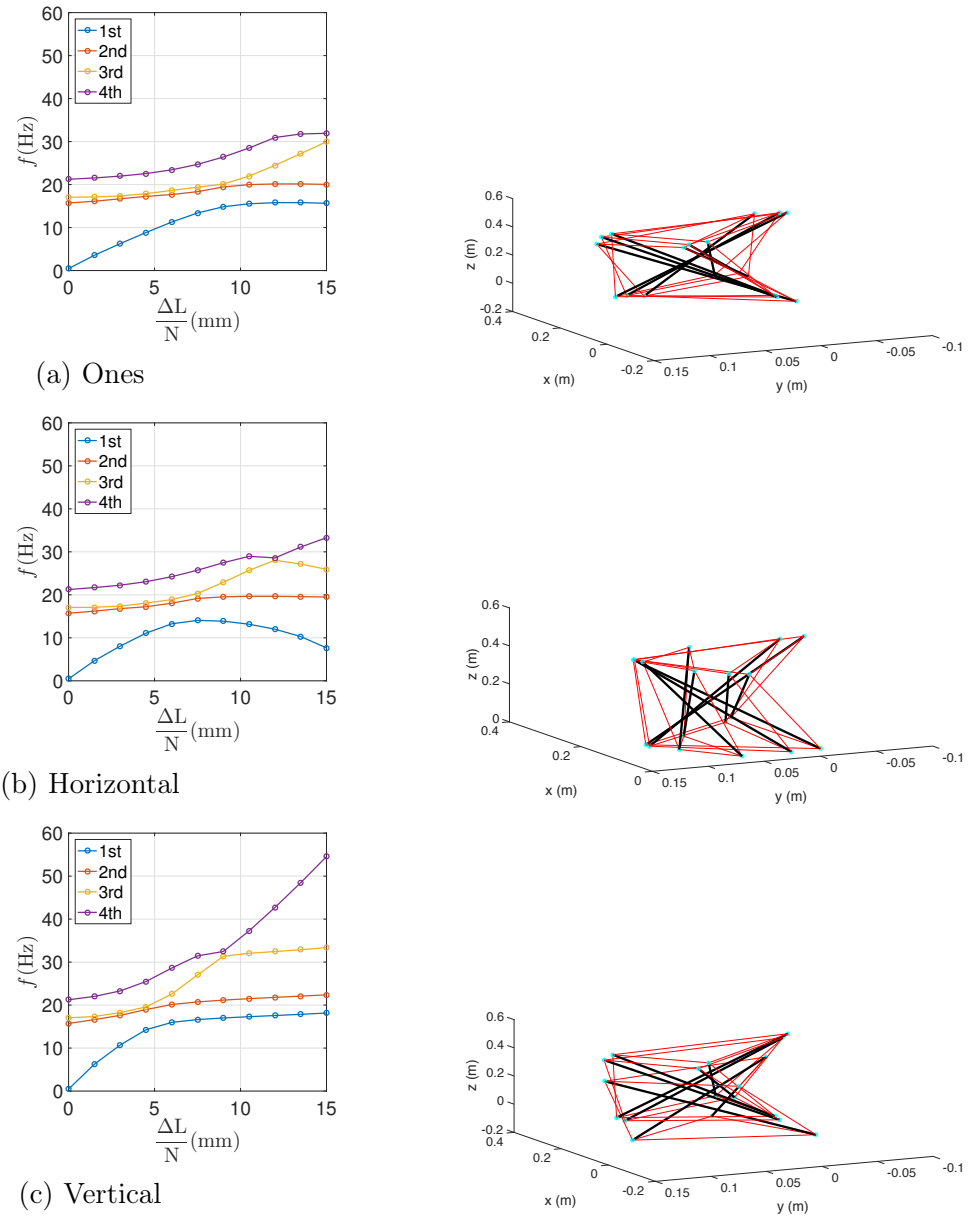

(a) Ones

(b) Horizontal

(c) Vertical

Figure 7.1: Natural frequency vs. length change for FFP

Fig. 7.1 shows the ones, horizontal, and vertical theoretical results for the FFP. These show the evolution of the natural frequencies with length change next to the corresponding shape change. The plots in Figs. 7.1 (a), 7.1 (b), and 7.1 (c) show natural frequency veering. These results also show that the natural frequencies will generally increase with length change. Note this algorithm was only capable of being applied to a tensegrity with all free nodes. It will successfully find equilibrium positions for the FFP based on length changes.

The following figures show the mode shapes for the first two non-zero modes (excluding the six rigid body modes). The mode shapes are displayed for the initial, half-way point, and final equilibrium positions. These are displayed for the three different actuation strategies.

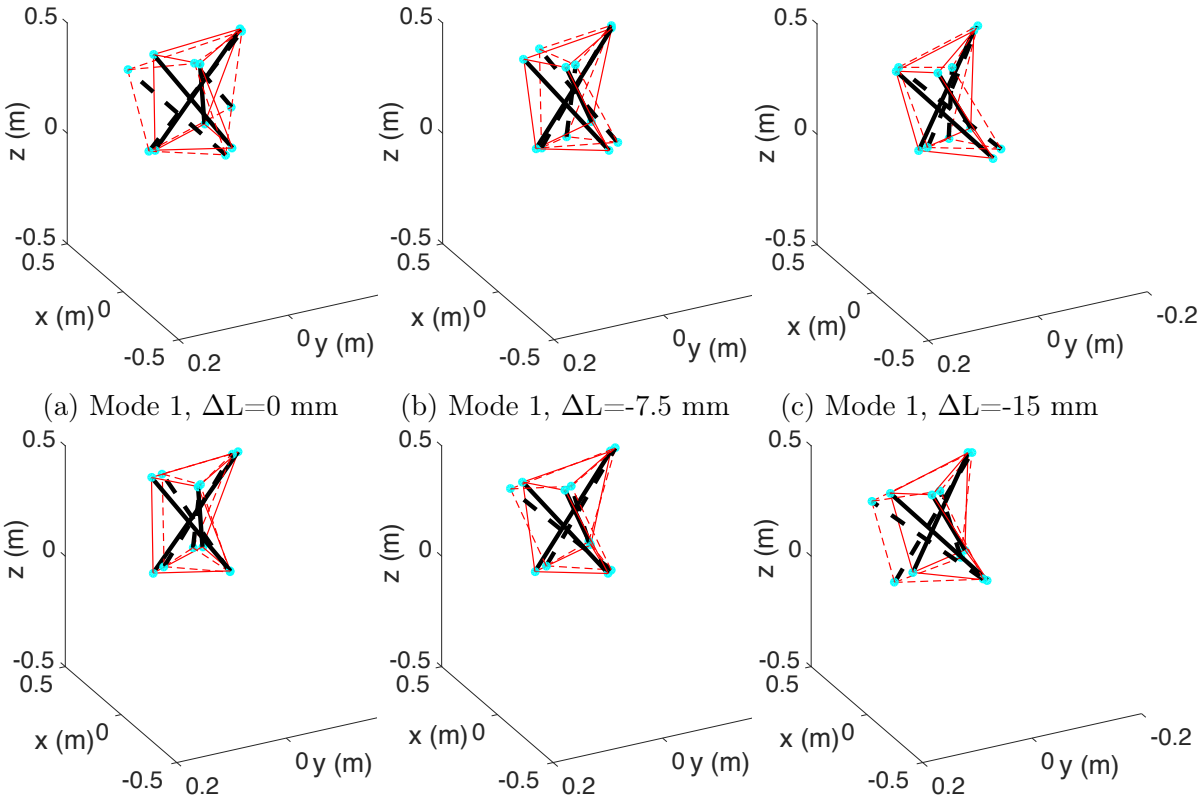

(a) Mode 1, ΔL=0 mm (b) Mode 1, ΔL=-7.5 mm (c) Mode 1, ΔL=-15 mm

(d) Mode 2, ΔL=0 mm (e) Mode 2, ΔL=-7.5 mm (f) Mode 2, ΔL=-15 mm

Figure 7.2: Mode shapes for FFP: Ones

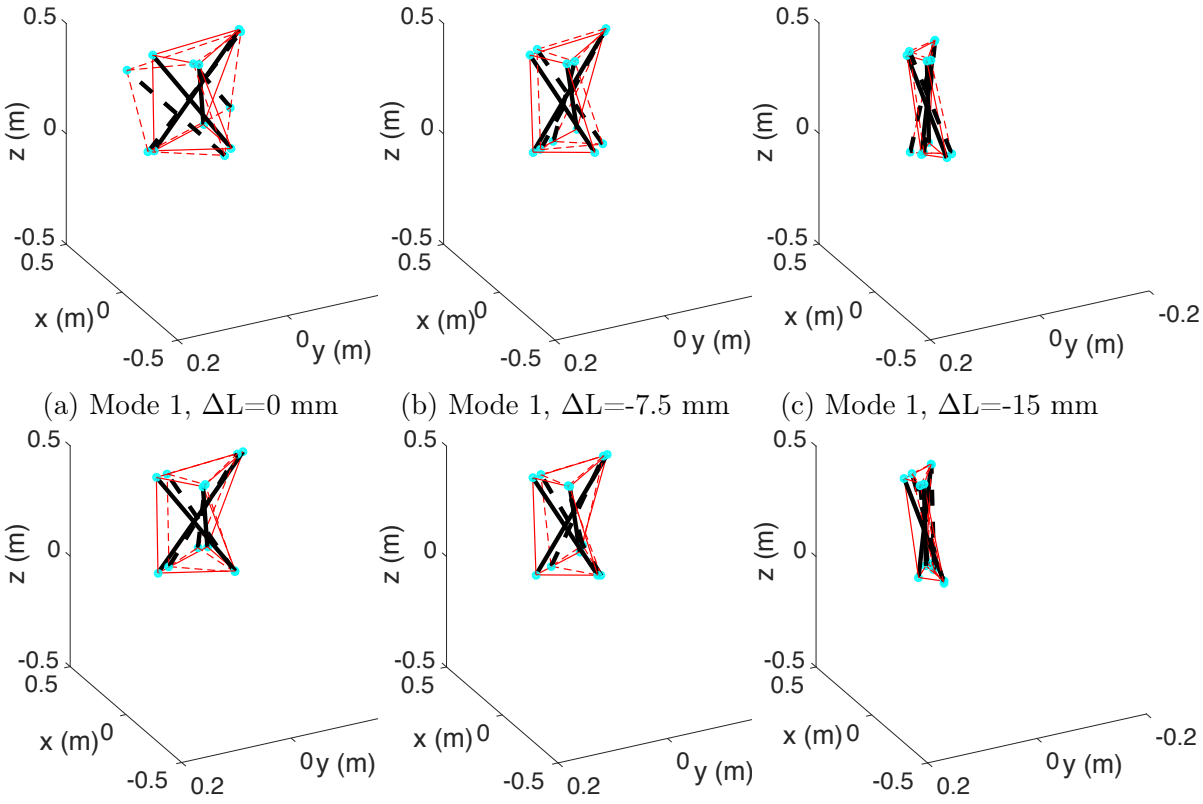

(a) Mode 1, ΔL=0 mm (b) Mode 1, ΔL=-7.5 mm (c) Mode 1, ΔL=-15 mm

(d) Mode 2, ΔL=0 mm (e) Mode 2, ΔL=-7.5 mm (f) Mode 2, ΔL=-15 mm

Figure 7.3: Mode shapes for FFP: Horizontal

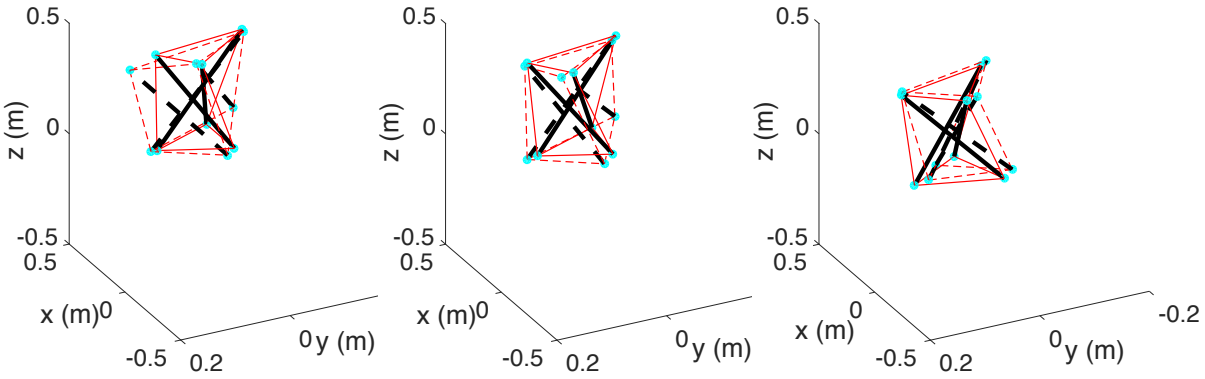

(a) Mode 1, ΔL=0 mm

(b) Mode 1, ΔL=-7.5 mm

(c) Mode 2, ΔL=-15 mm

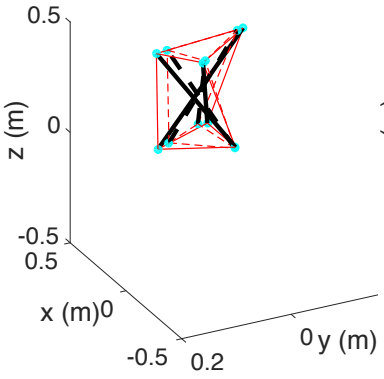

(d) Mode 2, ΔL=0 mm

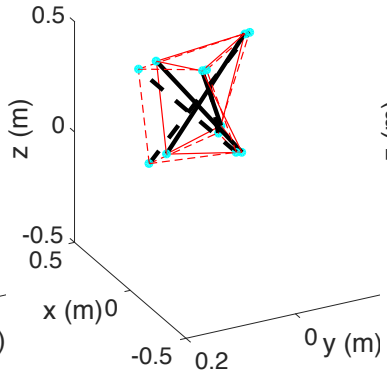

(e) Mode 2, ΔL=-7.5 mm

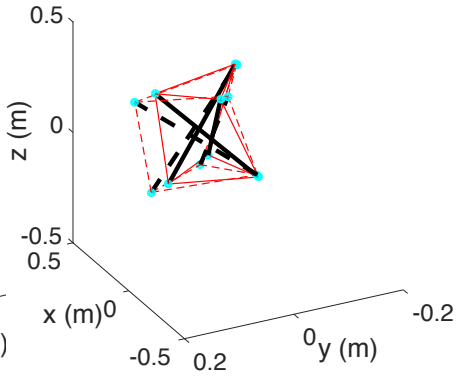

(f) Mode 2, ΔL=-15 mm

Figure 7.4: Mode shapes for FFP: Vertical

7.2 Experimental

The natural frequencies of the system can then be used to indicate how the structure will respond to aerodynamic loading. Thus, it is important to know the natural frequencies at which aeroelastic instabilities might occur to avoid dangerous regions. Flutter analysis indicates that the point where the bending and torsion modes coalesce is where the structure will go unstable. For this reason, the present work is concerned with the separation of the these modes of tensegrity structures.

A spectogram is a plot that shows the evolution of the natural frequencies with increasing length change. The FFP has wooden struts, while the CFP has metal.

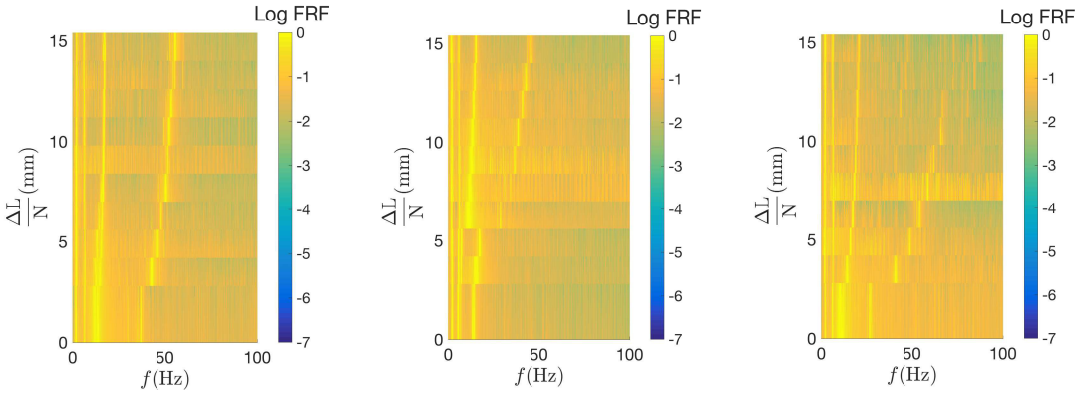

(a) Ones (b) Horizontal (c) Vertical

Figure 7.5: Spectograms for FFP

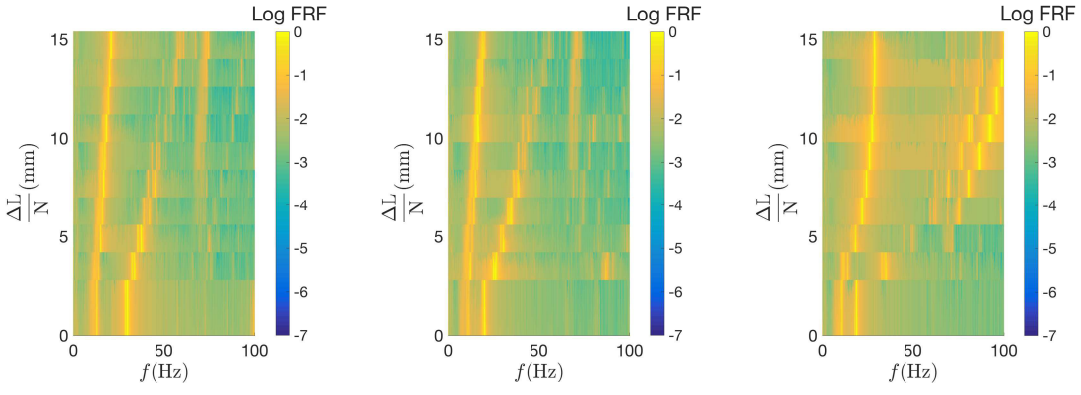

(a) Ones (b) Horizontal (c) Vertical

Figure 7.6: Spectograms for CFP

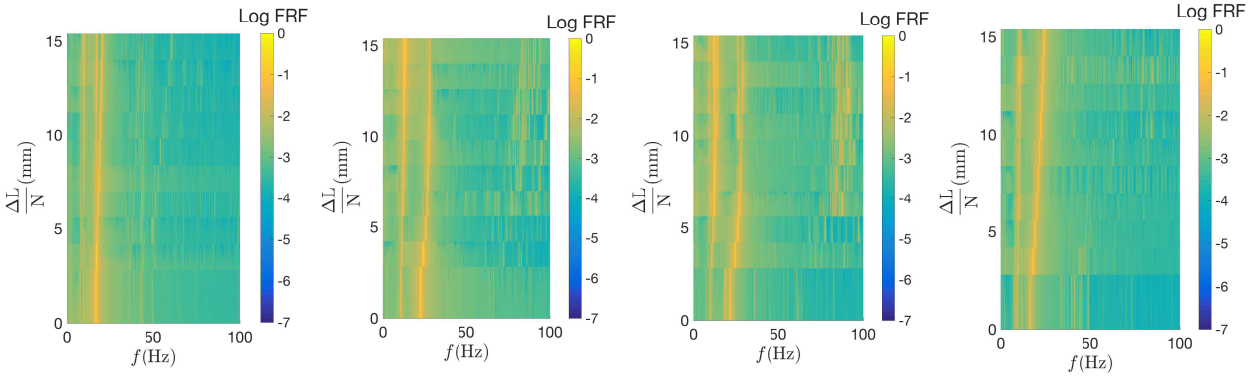

(a) Ones (b) Horizontal (c) Vertical (d) Alternating

Figure 7.7: Spectograms for CFM

In all spectograms, between about 2.5 mm and 5 mm, the natural frequencies change

more dramatically with length change, and then steadily increase. Fig. 7.5 shows that the first two modes for the FFP, in general, do not change with changing length. It is interesting that these two modes do not show up for the CFP and CFM test articles. It can be seen that tensegrities have several modal "families", which can be seen clearly in Fig. 7.7c. All spectograms show two families of modes. For all test articles, the vertical strategy particularly showed the largest separation overall, with the second family of modes showing the most exaggerated changes.

The second modal family for the CFP vertical case is not very well defined. This is probably due to testing inconsistencies. The natural frequencies for the CFM were much lower compared to the CFP and FFP.

For each length change increment, the peaks of the FRF were tracked and recorded manually. The missing data points indicate a resonance peak of the FRF that could not be detected. This mainly affected the fourth and fifth natural frequencies and occurred during the first few length change sets.

The following plots show the first five natural frequency peaks and their corresponding tensegrity system. The strike point is indicated on the diagram by a star symbol and the response point is indicated by the triangle symbol. Figs. 7.14, 7.15, 7.16, and 7.17 show the natural frequency maps.

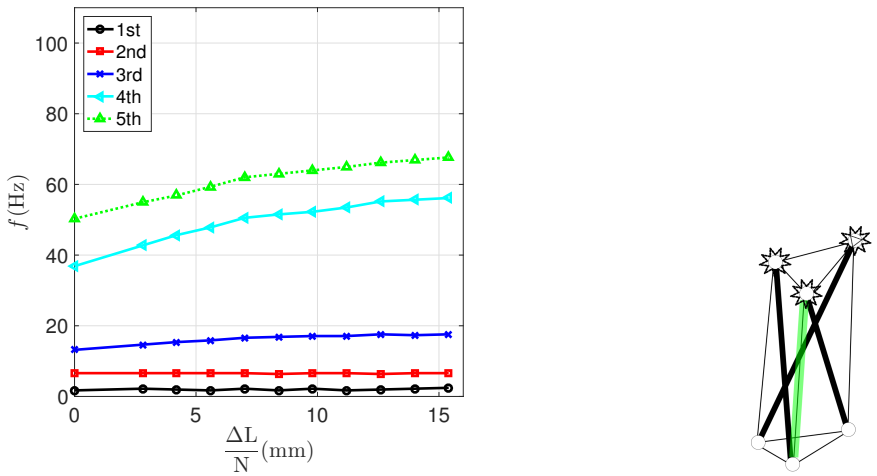

Figure 7.8: Natural frequency map for FFP: Ones

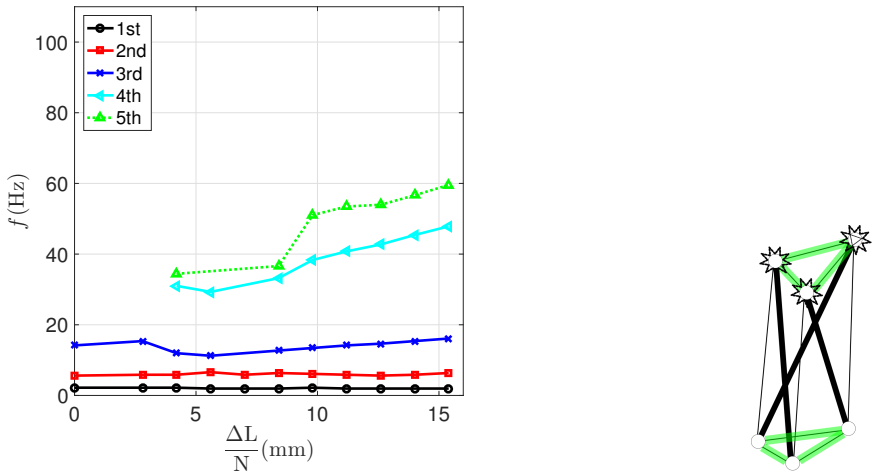

Figure 7.9: Natural frequency map for FFP: Horizontal

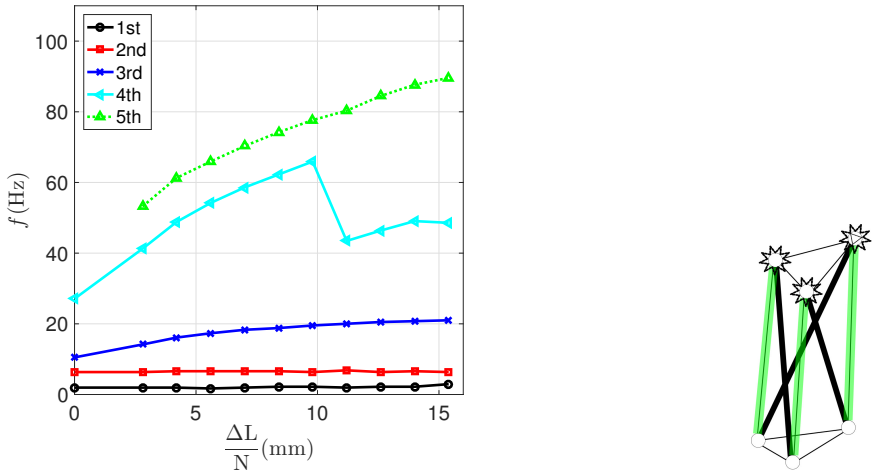

Figure 7.10: Natural frequency map for FFP: Vertical

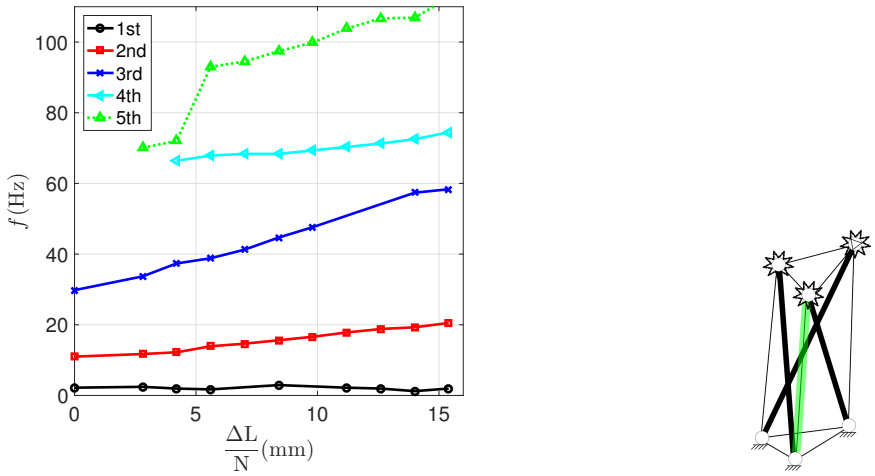

Figure 7.11: Natural frequency map for CFP: Ones

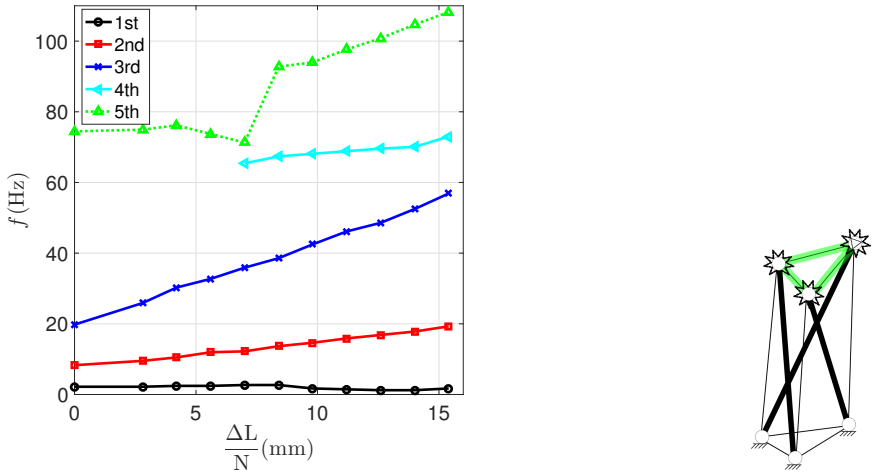

Figure 7.12: Natural frequency map for CFP: Horizontal

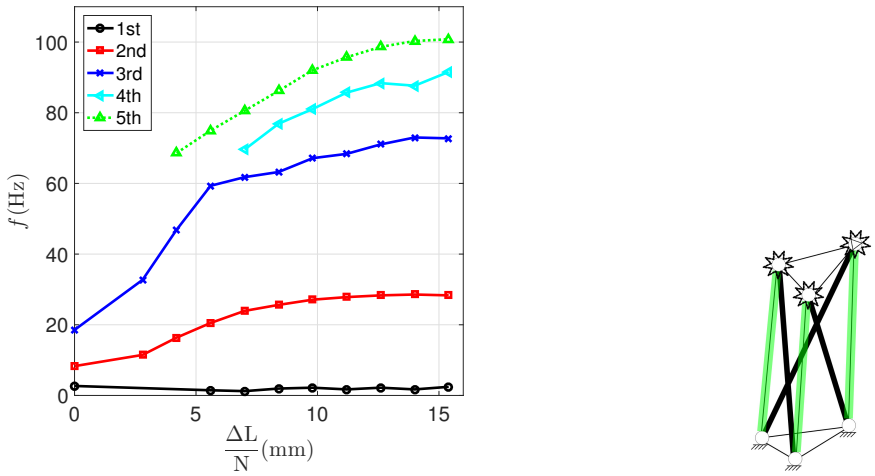

Figure 7.13: Natural frequency map for CFP: Vertical

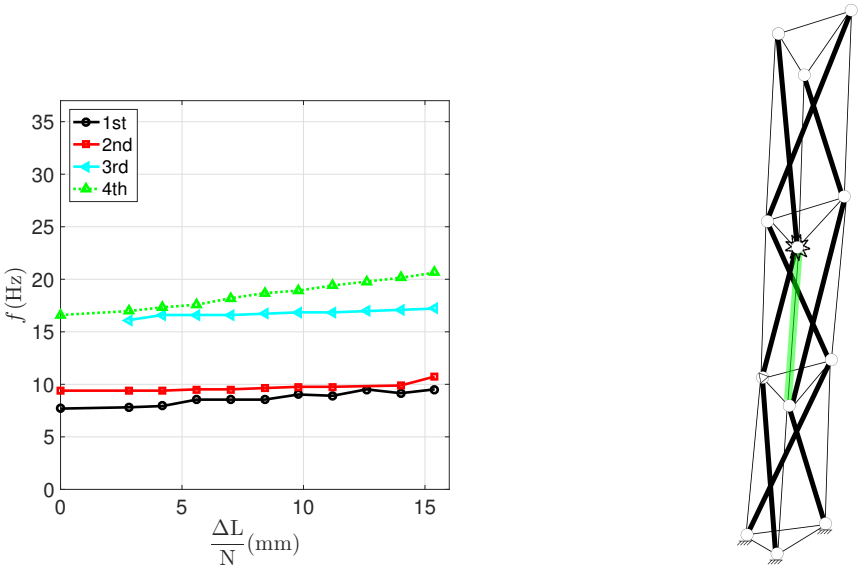

Figure 7.14: Natural frequency map for CFM: Ones

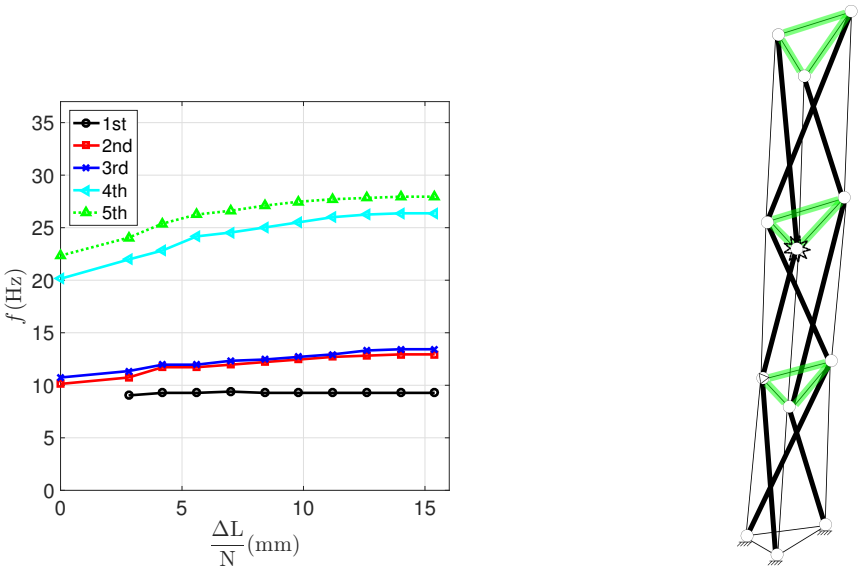

Figure 7.15: Natural frequency map for CFM: Horizontal

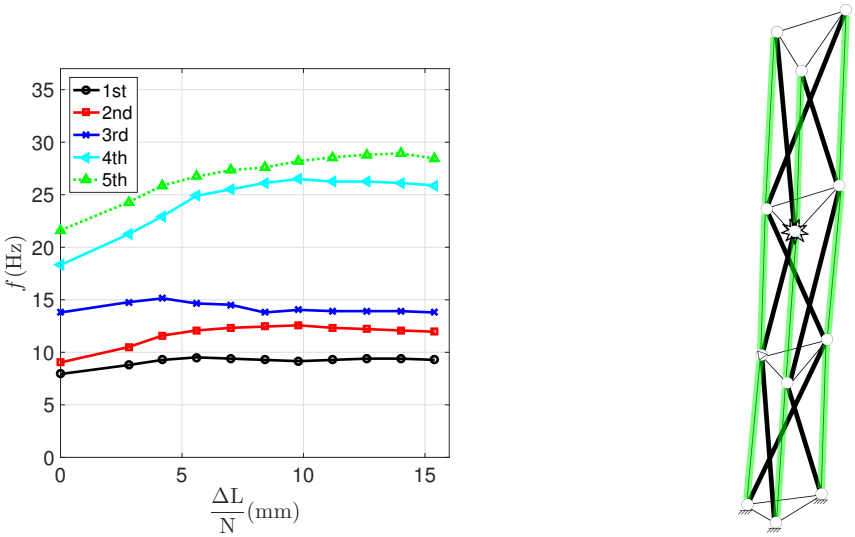

Figure 7.16: Natural frequency map for CFM: Vertical

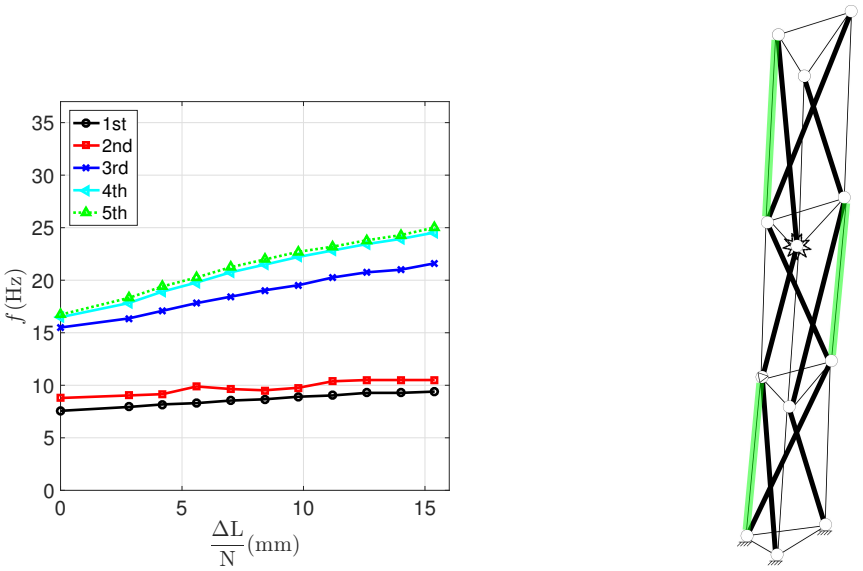

Figure 7.17: Natural frequency map for CFM: Alternating

For the CFM, the ones and alternating strategies have similar patterns, where modes 1 and 2 are one family and modes 3–5 are another. The natural frequencies for the horizontal and vertical cases are not as tightly grouped, where modes 1–3 are one family and 4 and 5 are the second. The reason for this is probably due to symmetrical versus asymmetrical actuation patterns. The natural frequencies for the ones and vertical cases for the FFP and CFP show similar trends, while the natural frequencies for the horizontal and vertical strategies of the CFM were the most comparable.

In some cases, the initial natural frequencies do not agree. This is due to the inconsistencies of cable length measurements for the initial configuration. Additionally, the structure slightly changed form between tests due to permanent cable stretching and strut bending. The sudden jump of the fourth natural frequency in Fig. 7.13 is probably due to resonance peaks in the FRF appearing and disappearing depending on strike and response directions.

7.3 Discussion

The natural frequencies for the ones and alternating cases of the CFM do not change much with increasing length change. This could be due to their asymmetries or could be because

a fewer number of cables are changed. The second and third natural frequencies changed the most for the CFM. The first three natural frequencies of the FFP changed the least compared to the CFP and CFM. This could due to the different boundary conditions.

For the FFP, modes three and four were the most sensitive to length change, while modes two and three were the most sensitive for the CFP and CFM. The separation between each pair of sensitive modes was computed for 0 mm and 16 mm. The percent change of separation between the two modes for each actuation strategy is shown in Table 7.1.

	Ones (%)	Horizontal (%)	Vertical (%)	Alternating (%)
FFP	62.8	66.6	66.1	
CFP	101.3	227.5	333.5	
CFM	3.72	37.7	167.5	65.5

Table 7.1: Maximum natural frequency separation

The CFP showed the highest maximum natural frequency separation. Furthermore, the CFP and FFP both showed higher separations than the CFM. For the FFP, the maximum separation is similar for every actuation strategy, with the horizontal and vertical strategies both at 66%. The CFP and CFM show a significant difference between actuation strategies, with the vertical strategy out performing the horizontal, and the horizontal case exceeding the ones case.

In general, the results show that actuating more cables produces a more dramatic increase in natural frequency. Overall, at each configuration, the first and second natural frequencies remained nearly constant, showing that a given length change will have more of an effect on the higher modes of a tensegrity. In the ones strategy, overall, the natural frequencies changed the least compared to the other strategies. The third and fourth modes of the FFP changed the most. The fourth and fifth natural frequencies for the CFP were much higher compared to the other test articles.

In all cases, the separation between the natural frequencies increased with length change.

Of all the actuation strategies performed on the CFM, the vertical configuration showed the largest maximum percentage increase in natural frequency separation. This means that changing vertical cables in the structure has more of an effect on the natural frequencies of the CFM than changing the alternating cables. The results of this experiment suggest that when designing an actuation system for a tensegrity mast, it would be best to distribute the controls on the vertical cables.

Dalilsafaei, et al. [14] found that placing actuators in all saddle cables of a saddle, vertical, diagonal tensegrity has a high influence on stiffness, while vertical cables were found to have limited effect on bending stiffness. The opposite effect was discovered in this work. For tensegrity prisms and masts, the vertical cables, as opposed to any other type of cable, have the largest affect on the natural frequency behavior.

f (Hz)	Ref. [102]	CFF (exp.)
Mode 1	1.07	1.709
Mode 2	9.103	6.592
Mode 3	9.103	13.18
Mode 4	20.884	36.87
Mode 5	20.884	50.29

Table 7.2: Natural frequency comparison of free-free tensegrity prisms

The first natural frequency of a two-stage tensegrity prism mast found by Safaei, et al. [32], at various slenderness ratios and pre-stress levels, ranges from 1.3 Hz to 23.8 Hz. The pre-stress levels ranged from 0.1 kN to 10 kN.

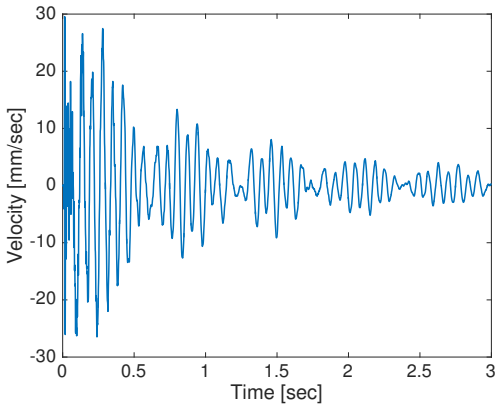

Figure 7.18: Sample time history

It is also interesting to note that the time history response, shown in Fig. 7.18, displays a beating pattern, indicative of the superposition of two slightly different natural frequencies, in this case, 16 and 17 Hz. The modulated frequency is about 1 Hz and the carrier frequency is about 16 Hz. Ali and Smith [148] also obtain a response experimentally with a beating pattern similar to this one.

Bossens, et al. [146] looks at the first four modes of a three-stage saddle-vertical-diagonal tensegrity mast and show the natural frequencies versus pre-tension level. They show the presence of a "soft" mode, which is also found in this study. Soft modes occur when the first natural frequency approaches zero as pre-tension approaches zero. The presence of a soft mode indicates an infinitesimal mechanism such that members of the structure can move without deforming. When soft modes exist, the stiffness of the structure can only be increased via pre-tension. Soft modes can be avoided by adding redundant cables.

Challenges

Some of the discrepancies in the experimental results could due to hitting the modal hammer on a curved surface. Discrepancies could also be due to the increased tension in the cables attached to the fixed magnets. Striking the test articles in their initial configurations resulted in larger amplitude oscillations, which weakened the signal strength of the laser. The curved surface for response resulted in poor laser signal. Also, changing direction of

impact strike could have influenced results. Repeatability could also be influenced by joint friction and cable relaxation [167]. If cable slackening had been taken into account in the study of Ref. [32], the difference in natural frequencies would have been larger as cables in the lowest stage become slack at very low tension.

The two most common tensegrity failures are strut buckling and loss of pre-tensioning level or cable yield [75]. Other limitations include turnbuckle range. Stretching and elongation come from two sources: constructional and elastic. Constructional elongation is a permanent stretching that results from the construction process, or plastic deformation, where the individual wires adjust under the load. Elastic deformation is a recoverable stretch that approximates Hooke's Law. It is believed that this permanent stretch is the reason for cable slackening. Note that the structures were left in a tensioned state overnight. The CFM showed the most cable stretch/slackening over time.

Because each member must articulate independently from the other at a node, the mechanical design of tensegrity joints can become complex [9]. The joint was the most challenging part of the design process because it has to have special requirements. The most restricting being that each joint of the CFM must be capable of maintaining a connection with both multiple cables and multiple struts. Refs. [164,168,169] look at the joint construction of tenesgrity prototypes, while Ref. [108] offers solutions for joint zones and connection points.

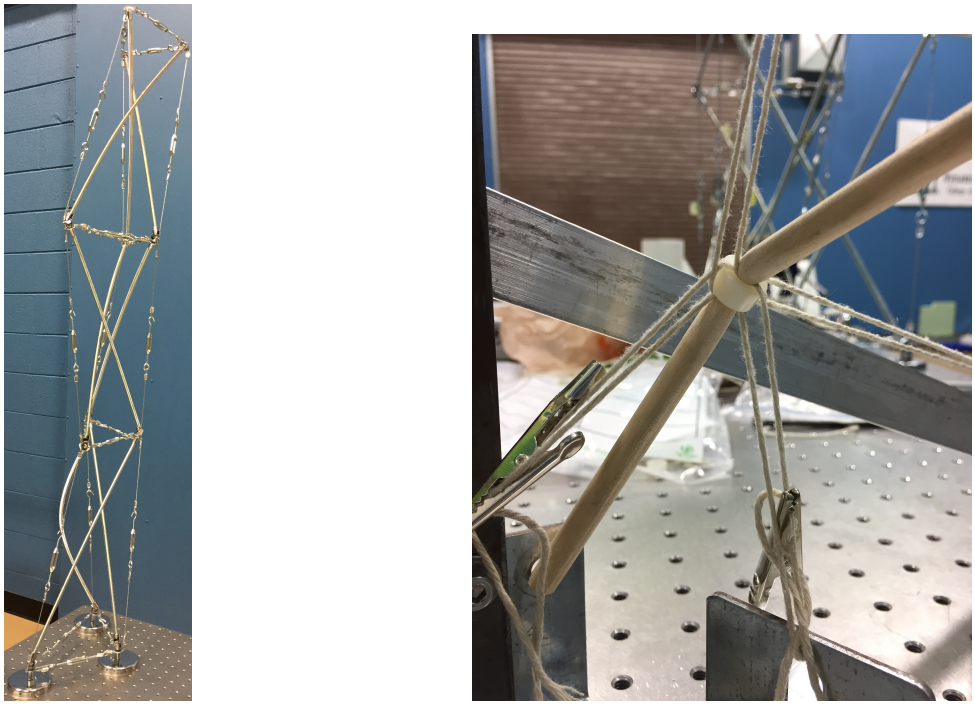

(a) (b)

Figure 7.19: (a) Bending of strut member of CFM, (b) Potential joint improvement

The joint design, shown in Fig. 6.8c, was used as an improvement of the CFM joint. Tensioning the cables resulted in strut bending, as shown in Fig. 7.19a, the most noticeable deformation occurring from the adjustment of the vertical cables (the longest cables). It is likely that this design is more prone to bending as a result of the attached cable members creating a resultant moment at each of the joints. It can be seen in Fig. 6.8c that for the CFM, the nodes would not be balanced because of the fact that the connection point of the cables is offset from that of the struts. The net cable force would then be acting on the struts and could have contributed to the bending behavior. When a force is not applied directly through the center of mass, it will create a torque. Thicker struts help prevent bending.

Chapter 8

Conclusion

The ability to shift the natural frequencies of a tensegrity-based wing offers a potential application towards flutter suppression. A tensegrity mast can be used for the architecture of an aircraft wing [68, 69].

Tensegrity structures offer the possibility of a revolution in aircraft wing design. Not only will tensegrity-based wings be lightweight, affordable, and strong, but they could also increase the efficiency and fuel economy of future aircraft by greatly reducing wing mass.

8.1 Future outlook

Prototypes need a better actuation design and a more precise way to change cables lengths. It would be useful to find an accurate way to directly measure current cable tension for different equilibrium positions. In addition, in the future, more attention will be given to asymmetric configurations via an optimizer. Ref. [170] also noticed significant deformation in their test article. Therefore, this problem needs to be addressed; it may be crucial to model buckling for tensegrity structures. Additionally, a more efficient testing method is needed, as the experimental process took about three hours per actuation pattern.

The practicality of a tensgrity wing in terms of the minimum stiffness required is discussed. In Ref. [26], the 87-stage tensegrity mast has a calculated bending stiffness of 0.11 $\mathrm{MN{\cdot}m^2}$. Ref. [171] indicates that a full-size vehicle wing would have a flat bending stiffness of about 0.6 $\mathrm{MN \cdot m^2}$. A traditional wing would be roughly 5.5 times stiffer than the tensegrity mast. Though this is not favorable, the tensegrity beam could potentially be constructed

and tensioned to be stiff enough for replacing the traditional wing spar. For instance, the beam could be made stiffer by changing the configuration, such as, incorporating more units for the same length. Or, perhaps by changing the material to one with a higher stiffness.

Appendix A

Form-Finding Algorithm Inputs/Results

These results are identical to the values obtained by Ref. [71]. For more numerical form-finding examples, refer to Ref. [54].

A.1 Hexagon tensegrity

Inputs

$d = 2; b = 9$

$$\mathbf{C} = \begin{bmatrix} -1 & 1 & 0 & 0 & 0 & 0 \\ 0 & -1 & 1 & 0 & 0 & 0 \\ 0 & 0 & -1 & 1 & 0 & 0 \\ 0 & 0 & 0 & -1 & 1 & 0 \\ 0 & 0 & 0 & 0 & -1 & 1 \\ -1 & 0 & 0 & 0 & 0 & 1 \\ -1 & 0 & 0 & 1 & 0 & 0 \\ 0 & -1 & 0 & 0 & 1 & 0 \\ 0 & 0 & -1 & 0 & 0 & 1 \end{bmatrix} \tag{A.1}$$

$$^{0}\mathbf{q} = \begin{bmatrix} 1 & 1 & 1 & 1 & 1 & 1 & -1 & -1 & -1 \end{bmatrix}^{\mathrm{T}} \tag{A.2}$$

Outputs

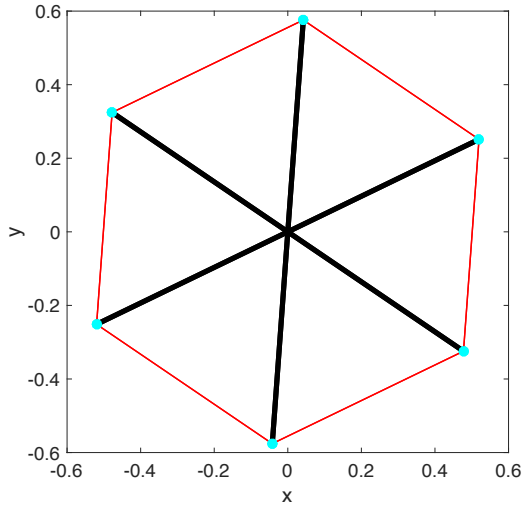

(a)

Node	x	y
1	0.5197	0.2514
2	0.4776	-0.3244
3	-0.0422	-0.5758
4	-0.5197	-0.2514
5	-0.4776	0.3244
6	-0.0422	0.5758

(b)

Figure A.1: (a) Equilibrium position, (b) Nodal Coordinates

$$ {}^{t}\mathbf{q} = \begin{bmatrix} 2 & 2 & 2 & 2 & 2 & 2 & -1 & -1 & -1 \end{bmatrix}^{\mathrm{T}} \tag{A.3} $$

t: 1

μ_b: 4.3467e-16

$s = 1$

A.2 Four-strut tensegrity

Inputs

$d = 2; b = 8$

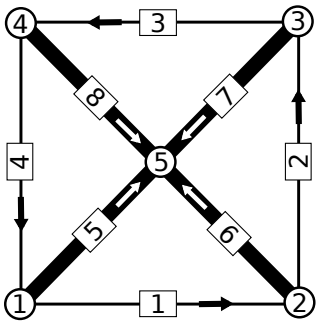

Figure A.2: Four-strut tensegrity connectivity

$$\mathbf{C} = \begin{bmatrix} -1 & 0 & 0 & 1 & 0 \\ -1 & 1 & 0 & 0 & 0 \\ 0 & -1 & 1 & 0 & 0 \\ 0 & 0 & -1 & 1 & 0 \\ -1 & 0 & 0 & 0 & 1 \\ 0 & -1 & 0 & 0 & 1 \\ 0 & 0 & -1 & 0 & 1 \\ 0 & 0 & 0 & -1 & 1 \end{bmatrix} \tag{A.4}$$

$${}^{0}\mathbf{q} = \begin{bmatrix} 1 & 1 & 1 & 1 & -1 & -1 & -1 & -1 \end{bmatrix}^{\mathrm{T}} \tag{A.5}$$

Outputs

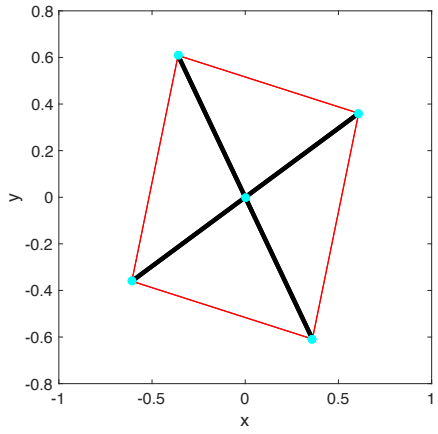

(a)

Node	x	y
1	0.3603	-0.6084
2	-0.6084	-0.3603
3	-0.3603	0.6084
4	0.6084	0.3603
5	-0.0000	-0.0000

(b)

Figure A.3: (a) Equilibrium position, (b) Nodal Coordinates

$$ {}^{t}\mathbf{q} = \begin{bmatrix} 1 & 1 & 1 & 1 & -2 & -2 & -2 & -2 \end{bmatrix}^{\mathrm{T}} \tag{A.6} $$

t: 1

μ_b: 3.5761e-16

$s = 1$

A.3 Two-module Snelson's X

Inputs

$d = 2; b = 11$

$$ {}^{0}\mathbf{x} = \begin{bmatrix} 0 & 2 & 4 & 0 & 2 & 4 \end{bmatrix}^{\mathrm{T}} \tag{A.7} $$

$$ {}^{0}\mathbf{y} = \begin{bmatrix} 0 & 0 & 0 & 1 & 1 & 1 \end{bmatrix}^{\mathrm{T}} \tag{A.8} $$

Outputs

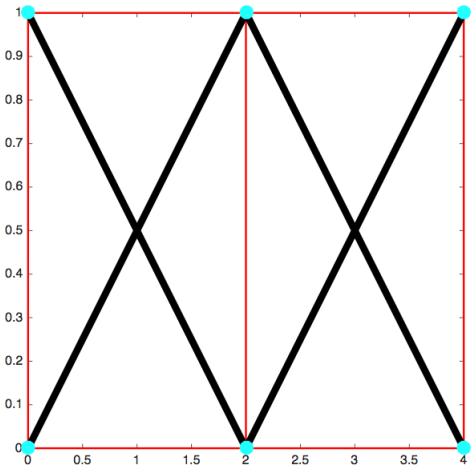

(a)

Node	x	y
1	0	0
2	2	0
3	4	0
4	0	1
5	2	1
6	4	1

(b)

Figure A.4: (a) Equilibrium position, (b) Nodal Coordinates

t: 1

μ_b: 3.1032e-16

$s = 2$

A.4 Tensegrty prism

Inputs

$d = 3; b = 12$

$$\mathbf{C} = \begin{bmatrix} -1 & 0 & 1 & 0 & 0 & 0 \\ 0 & -1 & 1 & 0 & 0 & 0 \\ -1 & 1 & 0 & 0 & 0 & 0 \\ 0 & 0 & 0 & -1 & 1 & 0 \\ 0 & 0 & 0 & 0 & -1 & 1 \\ 0 & 0 & 0 & -1 & 0 & 1 \\ -1 & 0 & 0 & 1 & 0 & 0 \\ 0 & -1 & 0 & 0 & 1 & 0 \\ 0 & 0 & -1 & 0 & 0 & 1 \\ -1 & 0 & 0 & 0 & 0 & 1 \\ 0 & -1 & 0 & 1 & 0 & 0 \\ 0 & 0 & -1 & 0 & 1 & 0 \end{bmatrix} \tag{A.9}$$

$${}^{0}\mathbf{q} = \begin{cases} 1 & \text{for all cables} \\ -1 & \text{for all struts} \end{cases} \tag{A.10}$$

Outputs

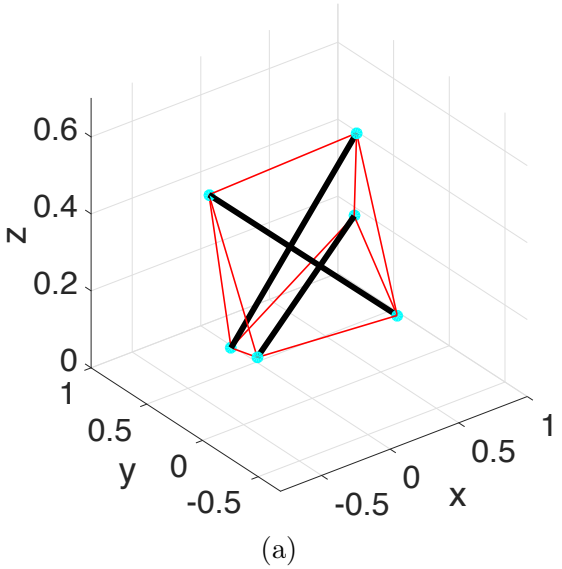

(a)

Node	x	y	z
1	0.5202	0.2504	0.5656
2	-0.4769	0.3254	0.5656
3	-0.0433	-0.5757	0.5656
4	-0.2504	0.5202	-0.1157
5	-0.3254	-0.4769	-0.1157
6	0.5757	-0.0433	-0.1157

(b)

Figure A.5: (a) Equilibrium position, (b) Nodal Coordinates

$$ {}^{t}\mathbf{q} = \begin{cases} 1 & \text{for cables 1—6} \\ \sqrt{3} & \text{for cables 7—9} \\ -\sqrt{3} & \text{for struts} \end{cases} \tag{A.11} $$

t: 1

μ_b: 9.4502e-16

$s = 1$

A.5 Expandable octahedron

Inputs

$d = 3, b = 30$

Outputs

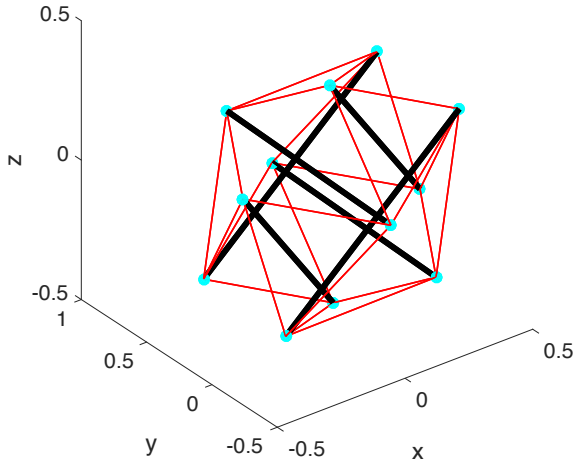

(a)

Node	x	y	z
1	0.2673	0.2359	0.3526
2	-0.4248	0.2105	-0.2124
3	0.3755	-0.1807	0.2367
4	-0.3166	-0.2061	-0.3283
5	-0.1107	-0.1392	0.4796
6	0.4074	0.1817	-0.1728
7	-0.4567	-0.1519	0.1971
8	0.0614	0.1690	-0.4553
9	-0.2624	0.3513	0.2912
10	-0.0460	-0.4819	0.0593
11	-0.0033	0.5117	-0.0350
12	0.2131	-0.3215	-0.2669

(b)

Figure A.6: (a) Equilibrium position, (b) Nodal Coordinates

$$ {}^{t}\mathbf{q} = \begin{cases} 1 & \text{for cables} \\ -1.5 & \text{for struts} \end{cases} \tag{A.12} $$

t: 21

μ_b: 1.3021e-15

$s = 1$

A.6 Three-module prism mast

Inputs

$d = 3; b = 30$

$$^{0}\mathbf{x} = \begin{bmatrix} 0.125 & 0.000 & 0.251 & 0.198 & 0.036 & 0.250 \end{bmatrix}^{\mathrm{T}} \tag{A.13}$$

$$^{0}\mathbf{y} = \begin{bmatrix} 0.116 & 0.000 & 0.000 & 0.104 & 0.052 & -0.065 \end{bmatrix}^{\mathrm{T}} \tag{A.14}$$

$$^{0}\mathbf{z} = \begin{bmatrix} 0.040 & 0.040 & 0.040 & 0.435 & 0.435 & 0.435 \end{bmatrix}^{\mathrm{T}} \tag{A.15}$$

These values were chosen because they are the roughly measured nodal coordinates of the physical test article.

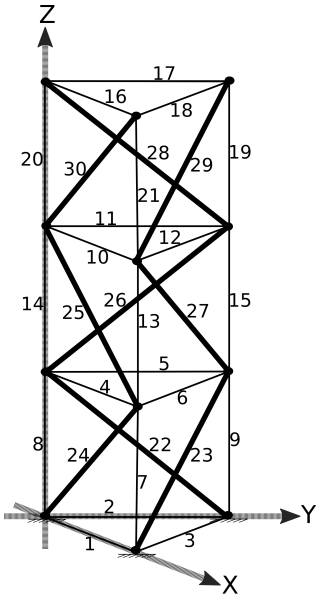

Figure A.7: Three-unit prism mast numbering scheme

Also found in Ref. [53], a typical one module tensegrity prism as in Fig. (6.2) has force density coefficients according to Eq. (A.12). Using the symmetry of Fig. (A.7), the following six groups ($h = 6$) are chosen:

h	b
h_1	1, 2, 3, 16, 17, 18
h_2	4, 5, 6, 10, 11, 12
h_3	13, 14, 15
h_4	7, 8, 9, 19, 20, 21
h_5	22, 23, 24, 28, 29, 30
h_6	25, 26, 27

Table A.1: Groups for three-unit prism mast

Bibliography

[1] D Ramsey. When art becomes autonomous. *U.C. San Deigo News Center*, October 2013.

[2] S Pellegrino and CR Calladine. Matrix analysis of statically and kinematically indeterminate frameworks. *International Journal of Solids and Structures*, 22(4):409–428, 1986.

[3] MR Ashory. *High quality modal testing methods*. PhD thesis, University of London, 1999.

[4] W Anderson and S Mortara. F-22 aeroelastic design and test validation. In *48th AIAA/ASME/ASCE/AHS/ASC Structures, Structural Dynamics, and Materials Conference*, page 1764, 2007.

[5] TE Noll, JM Brown, ME Perez-Davis, SD Ishmael, GC Tiffany, and M Gaier. Investigation of the helios prototype aircraft mishap report. *Technical report, National Aeronautics and Space Administration*, 9:2004, January 2004.

[6] S Barbarino, O Bilgen, RM Ajaj, MI Friswell, and DJ Inman. A review of morphing aircraft. *Journal of intelligent material systems and structures*, 22(9):823–877, 2011.

[7] AYN Sofla, SA Meguid, KT Tan, and WK Yeo. Shape morphing of aircraft wing: status and challenges. *Materials & Design*, 31(3):1284–1292, 2010.

[8] G Pietila and K Cohen. Dynamic modeling of morphing tensegrity structures. In *Infotech@ Aerospace 2011*, page 1534. 2011.

[9] WB Whittier. Kinematic analysis of tensegrity structures. 2002.

[10] B Nabet and NE Leonard. Tensegrity models and shape control of vehicle formations. *arXiv preprint arXiv:0902.3710*, 2009.

[11] B Domer. *Performance enhancement of active structures during service lives*. PhD thesis, École Polytechnique Fédérale De Lausanne, 2003.

[12] RE Skelton and MC de Oliveira. *Tensegrity systems*, volume 1. Springer, 2009.

[13] K Caluwaerts and JP Carbajal. Energy conserving constant shape optimization of tensegrity structures. *International Journal of Solids and Structures*, 58:117–127, 2015.

[14] S Dalilsafaei, A Eriksson, and G Tibert. Improving bending stiffness of tensegrity booms. *International Journal of Space Structures*, 27(2-3):117–129, 2012.

[15] Andrea Micheletti and WO Williams. Shape-change of tensegrity systems by controlling edge-lengths. *IASS, Venice, Italy*, 2007.

[16] RP Navaneeth Krishna. *Towards synthesis of tensegrity structures of desired shape and micro-pipette aspiration of red blood cells*. PhD thesis, Citeseer, 2013.

[17] KY Volokh, O Vilnay, and M Belsky. Tensegrity architecture explains linear stiffening and predicts softening of living cells. *Journal of biomechanics*, 33(12):1543–1549, 2000.

[18] E Postek, F Dubois, and R Mozul. Modeling of a collection of tensegrity particles with a non smooth discrete element method. In *38th Solid Mechanics Conference*, 2012.

[19] HC Tran and J Lee. Determination of a unique configuration of free-form tensegrity structures. *Acta mechanica*, 220(1):331–348, 2011.

[20] X Xu, Y Wang, and Y Luo. Numerical modeling of force-stiffness response of cross-linked actin networks using tensegrity systems. *Mathematical Problems in Engineering*, 2015, 2015.

[21] W Bourne, F Bello, and PF Villard. The use of tensegrity to simulate diaphragm motion through muscle and rib kinematics. *Imperial College London*, 2008.

[22] S Lessard, J Bruce, E Jung, M Teodorescu, V SunSpiral, and A Agogino. A lightweight, multi-axis compliant tensegrity joint. In *International Conference on Robotics and Automation*, 2016.

[23] SH Juan, JM Mirats-Tur, JR i Colomer, and P Avanı. Path planning for deformable robotic systems based on tensegrity structures.

[24] K Kim, AK Agogino, and AM Agogino. Emergent form-finding for center of mass control of ball-shaped tensegrity robots.

[25] AA Dobson and MJD Hayes. Tensegrity platforms and geometric form finding.

[26] AG Tibert and S Pellegrino. Deployable tensegrity masts. In *Proc. 44th AIAA/ASME/ASCE/AHS Structures, Structural Dynamics, and Materials Conference*, 2003.

[27] RE Skelton, R Adhikari, JP Pinaud, W Chan, and JW Helton. An introduction to the mechanics of tensegrity structures. In *40th IEEE Conference on Decision and Control*, volume 5, pages 4254–4259. IEEE, 2001.

[28] A Micheletti and D Cadoni. Design of single-layer floating-compression tensegrities. *Proceedings of CSMA*, 2011.

[29] M Masic and RE Skelton. Deployable plates made from stable-element class 1 tensegrity. In *SPIE's 9th Annual International Symposium on Smart Structures and Materials*, pages 220–230. International Society for Optics and Photonics, 2002.

[30] J Averseng and JF Dubé. Design, analysis and self stress setting of a lightweight deployable tensegrity modular structure. *Procedia Engineering*, 40:14–19, 2012.

[31] BF Knight. *Deployable antenna kinematics using tensegrity structure design.* PhD thesis, University of Florida, 2000.

[32] SD Safaei, A Eriksson, A Micheletti, and G Tibert. Study of various tensegrity modules as building blocks for slender booms. *International Journal of Space Structures*, 28(1):41–52, 2013.

[33] JJ Rimoli. On the impact tolerance of tensegrity-based planetary landers. In *57th AIAA/ASCE/AHS/ASC Structures, Structural Dynamics, and Materials Conference*, page 1511, 2016.

[34] S Korkmaz, NBH Ali, and IFC Smith. Determining control strategies for damage tolerance of an active tensegrity structure. *Engineering Structures*, 33(6):1930–1939, 2011.

[35] L Rhode-Barbarigos, NBH Ali, R Motro, and IFC Smith. Designing tensegrity modules for pedestrian bridges. *Engineering Structures*, 32(4):1158–1167, 2010.

[36] MH Zgoul, A Alzamer, MR Elayyan, and MA Quran. Static analysis of a tensegrity bridge using the finite element method. In *International Conference on Applications and Design in Mechanical Engineering (ICADME)*.

[37] S Lee and J Lee. Optimum self-stress design of cable–strut structures using frequency constraints. *International Journal of Mechanical Sciences*, 89:462–469, 2014.

[38] B Domer, E Fest, V Lalit, and IFC Smith. Combining dynamic relaxation method with artificial neural networks to enhance simulation of tensegrity structures. *Journal of Structural Engineering*, 129(5):672–681, 2003.

[39] NBH Ali, L Rhode-Barbarigos, and IFC Smith. Active tensegrity structures with sliding cables-static and dynamic behavior. *csma2011. lmgc. univ-montp2. fr*, pages 1–8, 2011.

[40] NBH Ali, L Rhode-Barbarigos, and IFC Smith. Analysis of clustered tensegrity structures using a modified dynamic relaxation algorithm. *International Journal of Solids and Structures*, 48(5):637–647, 2011.

[41] KW Moored and H Bart-Smith. Investigation of clustered actuation in tensegrity structures. *International Journal of Solids and Structures*, 46(17):3272–3281, 2009.

[42] GG Estrada, HJ Bungartz, and C Mohrdieck. Numerical form-finding of tensegrity structures. *International Journal of Solids and Structures*, 43(22):6855–6868, 2006.

[43] JY Zhang, SD Guest, and M Ohsaki. Symmetric prismatic tensegrity structures: Part i. configuration and stability. *International Journal of Solids and Structures*, 46(1):1–14, 2009.

[44] LY Zhang, Y Li, YP Cao, and XQ Feng. Stiffness matrix based form-finding method of tensegrity structures. *Engineering Structures*, 58:36–48, 2014.

[45] A González, AN Luo, and HP Liu. Construction of a unit cell tensegrity structure. In *Proceedings of 14th IFToMM World Congress, Taipei, doi*, volume 10, page 6567, 2015.

[46] K Koohestani. A computational framework for the form-finding and design of tensegrity structures. *Mechanics Research Communications*, 54:41–49, 2013.

[47] K Koohestani. Reshaping of tensegrities using a geometrical variation approach. *International Journal of Solids and Structures*, 71:233–243, 2015.

[48] J Zhang, M Ohsaki, SD Guest, and R Connelly. Stability of tensegrity structures with dihedral symmetry. In *Proceedings of the 9th Asian Pacific Conference on Shell and Spatial Structures*, 2009.

[49] M Miki. Extended force density method and its expressions. *J. IASS*, 2011.

[50] N Ashwear, G Tamadapu, and A Eriksson. Optimization of modular tensegrity structures for high stiffness and frequency separation requirements. *International Journal of Solids and Structures*, 80:297–309, 2016.

[51] HC Tran and J Lee. Form-finding of tensegrity structures with multiple states of self-stress. *Acta mechanica*, 222(1-2):131–147, 2011.

[52] C Paul, H Lipson, and FJV Cuevas. Evolutionary form-finding of tensegrity structures. In *Proceedings of the 7th annual conference on Genetic and evolutionary computation*, pages 3–10. ACM, 2005.

[53] N Vassart and R Motro. Multiparametered formfinding method: application to tensegrity systems. *International Journal of Space Structures*, 14(2):147–154, 1999.

[54] HC Tran and J Lee. Advanced form-finding of tensegrity structures. *Computers & structures*, 88(3):237–246, 2010.

[55] DTT Do, S Lee, and J Lee. A modified differential evolution algorithm for tensegrity structures. *Composite Structures*, 158:11–19, 2016.

[56] K Koohestani and SD Guest. A new approach to the analytical and numerical form-finding of tensegrity structures. *International Journal of Solids and Structures*, 50(19):2995–3007, 2013.

[57] J Lu, N Li, and G Shu. Form-finding analysis of irregular tensegrity structures by matrix iteration. *Advanced Steel Construction*, 11(4):507–516, 2015.

[58] S Lee and J Lee. A novel method for topology design of tensegrity structures. *Composite Structures*, 152:11–19, 2016.

[59] TEC Deifeld and RMO Pauletti. Numerical and physical modeling of tensegrity structures. In *IASS 2004 Symposium-Shell and Spatial Structures: from Models to Realization*, 2004.

[60] RE Skelton. Dynamics and control of tensegrity systems. In *IUTAM Symposium on Vibration Control of Nonlinear Mechanisms and Structures*, pages 309–318. Springer, 2005.

[61] NB Kahla and K Kebiche. Nonlinear elastoplastic analysis of tensegrity systems. *Engineering Structures*, 22(11):1552–1566, 2000.

[62] K Kebiche, MN Kazi-Aoual, and R Motro. Geometrical non-linear analysis of tensegrity systems. *Engineering Structures*, 21(9):864–876, 1999.

[63] J Averseng, J Quirant, and JF Dubé. Interactive dynamic design and analysis of tensegrity systems. *International Journal of Space Structures*, 27(2-3):97–106, 2012.

[64] M Jones and K Cohen. Fuzzy control of a tensegrity based morphing uav wing. In *Infotech@ Aerospace 2011*, page 1561. 2011.

[65] M Ohsaki, JY Zhang, and T Taguchi. Form-finding and stability analysis of tensegrity structures using nonlinear programming and fictitious material properties. In *Proceedings of the International Conference on Computational Methods*, 2014.

[66] M Masic and RE Skelton. Optimization of class 2 tensegrity towers. In *Smart Structures and Materials*, pages 163–174. International Society for Optics and Photonics, 2004.

[67] B De Jager and RE Skelton. Symbolic stiffness optimization of planar tensegrity structures. *Journal of Intelligent Material Systems and Structures*, 15(3):181–193, 2004.

[68] KW Moored and H Bart-Smith. The analysis of tensegrity structures for the design of a morphing wing. *Journal of Applied Mechanics*, 74(4):668–676, 2007.

[69] KW Moored and H Bart-Smith. The analysis of tensegrity structures for the design of a morphing wing. In *ASME 2005 International Mechanical Engineering Congress and Exposition*, pages 81–89. American Society of Mechanical Engineers, 2005.

[70] A Bronfeld. *Shape change algorithm for a tensegrity device*. Tel Aviv University, 2010.

[71] AG Tibert and S Pellegrino. Review of form-finding methods for tensegrity structures. *International Journal of Space Structures*, 26(3):241–255, 2011.

[72] JY Zhang and M Ohsaki. Form-finding of tensegrity structures subjected to geometrical constraints. *International Journal of Space Structures*, 21(4):183–195, 2006.

[73] S Faroughi and J Lee. Analysis of tensegrity structures subject to dynamic loading using a newmark approach. *Journal of Building Engineering*, 2:1–8, 2015.

[74] K Koohestani. Automated element grouping and self-stress identification of tensegrities. *Engineering Computations*, 32(6):1643–1660, 2015.

[75] N Ashwear and A Eriksson. Natural frequencies describe the pre-stress in tensegrity structures. *Computers & Structures*, 138:162–171, 2014.

[76] J Cai and J Feng. Form-finding of tensegrity structures using an optimization method. *Engineering Structures*, 104:126–132, 2015.

[77] Z Ji, T Li, and M Lin. Stiffness and dynamic analysis of a planar class-2 tensegrity mechanism. *Transactions of the Canadian Society for Mechanical Engineering*, 39(1):37, 2015.

[78] B de Jager. Design for shape control of tensegrities. In *American Control Conference, 2006*, pages 2528–2533. IEEE, 2006.

[79] B de Jager and RE Skelton. Input-output selection for planar tensegrity models. *IEEE transactions on control systems technology*, 13(5):778–785, 2005.

[80] B De Jager and RE Skelton. Symbolic stiffness optimization of planar tensegrity structures. *Journal of intelligent material systems and structures*, 15(3):181–193, 2004.

[81] AG de Jager and AG van Asch. Design of tensegrities: control vs. structural requirements. 2006.

[82] B De Jager, RE Skelton, and M Masic. Integrated control/structure design for planar tensegrity models. In *Control Applications, 2002. Proceedings of the 2002 International Conference on*, volume 2, pages 862–867. IEEE, 2002.

[83] B De Jager and RE Skelton. Stiffness of planar tensegrity beam topologies. In *Proc. Third World Conference on Structural Control*, pages 425–430, 2003.

[84] P Foti, A Fraddosio, S Marzano, G Pavone, and MD Piccioni. Self-equilibrium state of v-expander tensegrity beam. In *3rd International Balkans Conference on Challenges of Civil Engineering*, pages 126–135, 2016.

[85] Y Li, XQ Feng, YP Cao, and H Gao. A monte carlo form-finding method for large scale regular and irregular tensegrity structures. *International Journal of Solids and Structures*, 47(14):1888–1898, 2010.

[86] HC Tran and J Lee. Geometric and material nonlinear analysis of tensegrity structures. *Acta Mechanica Sinica*, 27(6):938–949, 2011.

[87] K Kebiche, MN Kazi-Aoual, and R Motro. Geometrical non-linear analysis of tensegrity systems. *Engineering structures*, 21(9):864–876, 1999.

[88] Y Kanno. Topology optimization of tensegrity structures under self-weight loads. *Journal of the Operations Research Society of Japan*, 55(2):125–145, 2012.

[89] L Zhang, Q Gao, and HW Zhang. An efficient algorithm for mechanical analysis of bimodular truss and tensegrity structures. *International Journal of Mechanical Sciences*, 70:57–68, 2013.

[90] A Micheletti and W Williams. A marching procedure for form-finding for tensegrity structures. *Journal of mechanics of materials and structures*, 2(5):857–882, 2007.

[91] P Foti, A Fraddosio, S Marzano, G Pavone, and MD Piccioni. On self-stress design in modular tensegrity grid structures. In *Proceedings of 11th international conference on applied and theoretical mechanics*, pages 95–104. Malaysia Kuala Lumpur, 2015.

[92] J Averseng, JF Dubé, B Crosnier, and R Motro. Active control of a tensegrity plane grid. In *Proceedings of the 44th IEEE Conference on Decision and Control*, pages 6830–6834. IEEE, 2005.

[93] N Angellier, JF Dubé, and B Crosnier. Comparison between experimental tests and numerical calculations carried out on a tensegrity mini grid. In *International Symposium New Olympics New Shell and Spatial Structures*, 2006.

[94] A Prakash. *Tensegrity based tower structures*. PhD thesis, Indian Institute Of Technology Delhi, 2007.

[95] HC Tran and J Lee. Initial self-stress design of tensegrity grid structures. *Computers & structures*, 88(9):558–566, 2010.

[96] JY Zhang and M Ohsaki. Optimization methods for force and shape design of tensegrity structures. In *Proc. 7th World Congress on Structural and Multidisciplinary Optimization, Seoul, Korea, May*, pages 21–25, 2007.

[97] M Ohsaki, JY Zhang, and Y Ohishi. Force design of tensegrity structures by enumeration of vertices of feasible region. *International Journal of Space Structures*, 23(2):117–125, 2008.

[98] G Fagerström. Dynamic relaxation of tensegrity structures. In *Proceedings of the 14th International Conference on Computer Aided Architectural Design Research in Asia/Yunlin (Taiwan)*, volume 22, pages 553–562, 2009.

[99] S Ehara and Y Kanno. Topology design of tensegrity structures via mixed integer programming. *International Journal of Solids and Structures*, 47(5):571–579, 2010.

[100] BS Gan, J Zhang, DK Nguyen, and E Nouchi. Node-based genetic form-finding of irregular tensegrity structures. *Computers & Structures*, 159:61–73, 2015.

[101] D Veenendaal and P Block. A framework for comparing form finding methods. In *Proceedings of the International Association for Shell and Spatial Structures (IABSE-IASS) Symposium*, 2011.

[102] M Attig, M Abdelghani, and N Kahla. Output-only modal identification of tensegrity structures. *Engineering Structures and Technologies*, 8(2):52–64, 2016.

[103] JV Henrickson, RE Skelton, and J Valasek. Shape control of tensegrity airfoils. In *AIAA Guidance, Navigation, and Control Conference*, page 1864, 2016.

[104] XF Yuan and SL Dong. Integral feasible prestress of cable domes. *Computers & structures*, 81(21):2111–2119, 2003.

[105] HC Tran, HS Park, and J Lee. A unique feasible mode of prestress design for cable domes. *Finite Elements in Analysis and Design*, 59:44–54, 2012.

[106] X Yuan, L Chen, and S Dong. Prestress design of cable domes with new forms. *International Journal of Solids and Structures*, 44(9):2773–2782, 2007.

[107] L Lachauer and P Block. Interactive equilibrium modelling. *International Journal of Space Structures*, 29(1):25–37, 2014.

[108] A Falk and G Tibert. Plate based tensegrity structures. In *Proceedings of the IASS 2005 Symposium*, pages 611–618, 2005.

[109] WL Chan, D Arbelaez, F Bossens, and RE Skelton. Active vibration control of a three-stage tensegrity structure. In *Smart Structures and Materials*, pages 340–346. International Society for Optics and Photonics, 2004.

[110] KW Moored, SA Taylor, TK Bliss, and H Bart-Smith. Optimization of a tensegrity wing for biomimetic applications. In *Decision and Control, 2006 45th IEEE Conference on*, pages 2288–2293. IEEE, 2006.

[111] MD Stubbs. *Kinematic design and analysis of a morphing wing*. PhD thesis, Virginia Polytechnic Institute and State University, 2003.

[112] KW Moored and H Bart-Smith. Developing a morphing fin for a biomimetic underwater vehicle.

[113] KW Moored, TH Kemp, NE Houle, and H Bart-Smith. Analytical predictions, optimization, and design of a tensegrity-based artificial pectoral fin. *International Journal of Solids and Structures*, 48(22):3142–3159, 2011.

[114] T Bliss, T Iwasaki, and H Bart-Smith. Central pattern generator control of a tensegrity swimmer. *IEEE/ASME Transactions on Mechatronics*, 18(2):586–597, 2013.

[115] A Plummer and G Lai. New concepts for parallel kinematic mechanisms using fluid actuation. In *7th International conference on Fluid Power and Mechatronics*. University of Bath, 2015.

[116] X Xu, Y Wang, and Y Luo. General approach for topology-finding of tensegrity structures. *Journal of Structural Engineering*, 142(10):04016061, 2016.

[117] S Faroughi, MA Kamran, and J Lee. A genetic algorithm approach for 2-d tensegrity form finding. *Advances in Structural Engineering*, 17(11):1669–1679, 2014.

[118] LY Zhang, HP Zhao, and XQ Feng. Constructing large-scale tensegrity structures with bar–bar connection using prismatic elementary cells. *Archive of Applied Mechanics*, 85(3):383–394, 2015.

[119] WJ Lewis. Computational form-finding methods for fabric structures. *Proceedings of the ICE-Engineering and Computational Mechanics*, 161(3):139–149, 2008.

[120] V Gomez-Jauregui, C Otero, R Arias, and C Manchado. Innovative families of double-layer tensegrity grids: Quastruts and sixstruts. *Journal of Structural Engineering*, 139(9):1618–1636, 2012.

[121] L Lachauer and P Block. Interactive equilibrium modelling. *International Journal of Space Structures*, 29(1):25–37, 2014.

[122] NBH Ali and IFC Smith. Dynamic analysis and vibration control of an active tensegrity structure. In *CIMNE*, number EPFL-CONF-148738, pages 18–25, 2009.

[123] D Veenendaal and P Block. An overview and comparison of structural form finding methods for general networks. *International Journal of Solids and Structures*, 49(26):3741–3753, 2012.

[124] R Kouhia. Computational techniques for the non-linear analysis of structures. 2009.

[125] B Nabet and N Leonard. Shape control of a multi-agent system using tensegrity structures. *Lagrangian and Hamiltonian methods for nonlinear control 2006*, pages 329–339, 2007.

[126] A Harichandran and IY Sreevalli. Form-finding of tensegrity structures based on force density method. *Indian Journal of Science and Technology*, 9(24), 2016.

[127] J Zhang and M Ohsaki. Form-finding of self-stressed structures by an extended force density method. *Journal of the International Association for Shell and Spatial Structures*, 46(3):159–166, 2005.

[128] HJ Schek. The force density method for form finding and computation of general networks. *Computer Methods in Applied Mechanics and Engineering*, 3(1):115–134, 1974.

[129] KS Lee and SE Han. Advanced shape finding algorithm of force density method based on fem. *Advanced Steel Construction*, pages 313–329, 2011.

[130] M Miki and K Kawaguchi. Extended force density method for form-finding of tension structures. *Journal of the International Association for Shell and Spatial Structures*, 51(4):291, 2010.

[131] M Miki and K Kawaguchi. Comparison of foregoing methods on form-finding of tension structures. In *6th China-Japan-Korea Joint Symposium on Optimization of Structural and Mechanical Systems*, 2010.

[132] G Tibert. Optimal design of tension truss antennas. In *44th AIAA/ASME/ASCE/AHS/ASC Structures, Structural Dynamics, and Materials Conference*, page 1629, 2003.

[133] JY Zhang, M Ohsaki, and Y Kanno. A direct approach to design of geometry and forces of tensegrity systems. *International Journal of Solids and Structures*, 43(7):2260–2278, 2006.

[134] K Koohestani. Form-finding of tensegrity structures via genetic algorithm. *International Journal of Solids and Structures*, 49(5):739–747, 2012.

[135] Y Chen, J Feng, R Ma, and Y Zhang. Efficient symmetry method for calculating integral prestress modes of statically indeterminate cable-strut structures. *Journal of Structural Engineering*, 141(10):04014240, 2014.

[136] BS Gan, J Zhang, DK Nguyen, and E Nouchi. Node-based genetic form-finding of irregular tensegrity structures. *Computers & Structures*, 159:61–73, 2015.

[137] T Tachi. Interactive freeform design of tensegrity. 2012.

[138] Y Kanno. Exploring new tensegrity structures via mixed integer programming. *Structural and Multidisciplinary Optimization*, 48(1):95–114, 2013.

[139] M Pagitz and JMM Tur. Finite element based form-finding algorithm for tensegrity structures. *International Journal of Solids and Structures*, 46(17):3235–3240, 2009.

[140] S Lee and J Lee. Form-finding of tensegrity structures with arbitrary strut and cable members. *International Journal of Mechanical Sciences*, 85:55–62, 2014.

[141] S Dalil Safaei, A Eriksson, and G Tibert. Optimum pre-stress design for frequency requirement of tensegrity structures. In *10th World Congress on Computational Mechanics*, 2011.

[142] S Faroughi and JM Mirats-Tur. Vibration properties in the design of tensegrity structure. *Journal of Vibration and Control*, 21(3):611–624, 2015.

[143] IJ Oppenheim and WO Williams. Vibration and damping in three-bar tensegrity structure. *Journal of Aerospace Engineering*, 14(3):85–91, 2001.

[144] W Chan, D Arbelaez, F Bossens, and RE Skelton. Active vibration control of a three-stage tensegrity structure. In *Proc. of SPIE Vol*, volume 5386, page 341, 2004.

[145] J Michielsen, RHB Fey, and H Nijmeijer. Steady-state dynamics of a 3D tensegrity structure: simulations and experiments. *International Journal of Solids and Structures*, 49(7):973–988, 2012.

[146] F Bossens, RA de Callafon, and RE Skelton. Modal analysis of a tensegrity structure–an experimental study. *Department of Mechanical and Aerospace Engineering, Dynamic Systems and Control Group, University of California, San Diego, USA*, 2007.

[147] LGA Rhode-Barbarigos. *An active deployable tensegrity structure*. PhD thesis, École Polytechnique Fédérale De Lausanne, 2012.

[148] NBH Ali and IFC Smith. Dynamic behavior and vibration control of a tensegrity structure. *International Journal of Solids and Structures*, 47(9):1285–1296, 2010.

[149] G Strang. *Linear algebra and its applications*, volume 3. Harcourt, Brace, Jovanovich, Publishers, 1988.

[150] HC Tran and J Lee. Self-stress design of tensegrity grid structures with exostresses. *International Journal of Solids and Structures*, 47(20):2660–2671, 2010.

[151] C Sultan, M Corless, and RE Skelton. Linear dynamics of tensegrity structures. *Engineering Structures*, 24(6):671–685, 2002.

[152] GG Estrada. *Analytical and numerical investigations of form-finding methods for tensegrity structures*. Shaker, 2007.

[153] S Pellegrino. Structural computations with the singular value decomposition of the equilibrium matrix. *International Journal of Solids and Structures*, 30(21):3025–3035, 1993.

[154] CH Wolkowicz, J Ruth, and A Stahr. Tool to check topology and geometry for spatial structures on basis of the extended maxwell‘s rule. In *Proceedings International Conference on the Applications of Computer, Science and Mathematics in Architecture and Civil Engineering, Weimar*, 2006.

[155] J Averseng and B Crosnier. Prestressing tensegrity systems: application to multiple selfstress state structures. *International Journal of Structural Stability and Dynamics*, 4(04):543–557, 2004.

[156] LY Zhang, Y Li, YP Cao, XQ Feng, and H Gao. A numerical method for simulating nonlinear mechanical responses of tensegrity structures under large deformations. *Journal of Applied Mechanics*, 80(6):061018, 2013.

[157] M Ohsaki and J Zhang. Stability conditions of prestressed pin-jointed structures. *International Journal of Non-Linear Mechanics*, 41(10):1109–1117, 2006.

[158] A Micheletti. Bistable regimes in an elastic tensegrity system. In *Proc. R. Soc. A*, volume 469, page 20130052. The Royal Society, 2013.

[159] LY Zhang, Y Li, YP Cao, XQ Feng, and H Gao. Self-equilibrium and super-stability of truncated regular polyhedral tensegrity structures: a unified analytical solution. In *Proc. R. Soc. A*, volume 468, pages 3323–3347. The Royal Society, 2012.

[160] Y Chen, J Feng, and Y Zhang. A necessary condition for stability of kinematically indeterminate pin-jointed structures with symmetry. *Mechanics Research Communications*, 60:64–73, 2014.

[161] LY Zhang, Y Li, YP Cao, and XQ Feng. A unified solution for self-equilibrium and super-stability of rhombic truncated regular polyhedral tensegrities. *International Journal of Solids and Structures*, 50(1):234–245, 2013.

[162] H Tanaka and MC Natori. Shape control of cable-network structures based on concept of self-equilibrated stresses. *JSME International Journal Series C Mechanical Systems, Machine Elements and Manufacturing*, 49(4):1067–1072, 2006.

[163] S Lee and J Lee. Optimum self-stress design of cable–strut structures using frequency constraints. *International Journal of Mechanical Sciences*, 89:462–469, 2014.

[164] M Cefalo and JM Mirats-Tur. A comprehensive dynamic model for class-1 tensegrity systems based on quaternions. *International Journal of Solids and Structures*, 48(5):785–802, 2011.

[165] JR Wright and JE Cooper. *Introduction to aircraft aeroelasticity and loads*, volume 20. John Wiley & Sons, 2008.

[166] BJ Schwarz and MH Richardson. Experimental modal analysis. *CSI Reliability week*, 35(1):1–12, 1999.

[167] E Fest, K Shea, B Domer, and IFC Smith. Adjustable tensegrity structures. *Journal of Structural Engineering*, 129(4):515–526, 2003.

[168] JM Mirats-Tur. On the movement of tensegrity structures. *International Journal of Space Structures*, 25(1):1–13, 2010.

[169] B Shekastehband, K Abedi, and N Dianat. Experimental and numerical study on the self-stress design of tensegrity systems. *Meccanica*, 48(10):2367–2389, 2013.

[170] A Amendola, G Carpentieri, M De Oliveira, RE Skelton, and F Fraternali. Experimental investigation of the softening–stiffening response of tensegrity prisms under compressive loading. *Composite Structures*, 117:234–243, 2014.

[171] Z Wan and CES Cesnik. Geometrically nonlinear aeroelastic scaling for very flexible aircraft. *AIAA Journal*, 52(10):2251–2260, 2014.